

Master's Dissertation in Mechanical Engineering on:

Finite element analysis of residual stresses in metallic parts produced by additive manufacturing

Maria Madureira Pires

Supervisor: Prof. Marco Parente

Co-Supervisor: Prof. Abílio de Jesus



Mestrado Integrado em Engenharia Mecânica

July 20, 2021

“O que há em mim é sobretudo cansaço
 Não disto nem daquilo,
 Nem sequer de tudo ou de nada:
 Cansaço assim mesmo, ele mesmo,
 Cansaço.

A subtileza das sensações inúteis,
 As paixões violentas por coisa nenhuma,
 Os amores intensos por o suposto alguém.
 Essas coisas todas -
 Essas e o que faz falta nelas eternamente -;
 Tudo isso faz um cansaço,
 Este cansaço,
 Cansaço.

Há sem dúvida quem ame o infinito,
 Há sem dúvida quem deseje o impossível,
 Há sem dúvida quem não queira nada -
 Três tipos de idealistas, e eu nenhum deles:
 Porque eu amo infinitamente o finito,
 Porque eu desejo impossivelmente o possível,
 Porque eu quero tudo, ou um pouco mais, se puder ser,
 Ou até se não puder ser...

E o resultado?
 Para eles a vida vivida ou sonhada,
 Para eles o sonho sonhado ou vivido,
 Para eles a média entre tudo e nada, isto é, isto...
 Para mim só um grande, um profundo,
 E, ah com que felicidade infecundo, cansaço,
 Um supremíssimo cansaço.
 Íssimo, íssimo. íssimo,
 Cansaço...”

Álvaro de Campos, *O que há em mim é sobretudo cansaço*

This page was intentionally left blank.

Abstract

Metal additive manufacturing has gathered the interest of many researchers and the industry in recent years. These methods are now frequently capable of producing high strength parts with static strengths that exceed their conventionally manufactured counterparts due to ongoing process improvements. On the other hand, these processes produce large and anisotropic residual stresses, which can have a significant impact on fatigue characteristics and cause geometric distortion.

Since residual stress formation is dependent on processing variables, material properties and part geometry, it is difficult to efficiently predict their behaviour. As a result, the demand for numerical models that can accurately anticipate a component's microstructure, distortion and residual stresses has increased. Computer simulation is a useful tool for assisting with experimental work and reducing the amount of time and money spent on it, however, the simulation process is very challenging and presents several limitations.

The main goal of this dissertation is to gain insight into commercially available finite element packages that simulate metallic additive manufacturing processes, specifically Laser Powder Bed Fusion and Direct Energy Deposition, in the context of distortion and residual stress simulation. Each of these techniques uses a heat source that fuses each layer in a certain pattern, gradually constructing the part. The final residual stresses and deformations are influenced by the complex thermal history. Thermo-mechanical finite element analysis can be used to model these effects, promoting the production of high quality parts. This is accomplished by conducting convergence and parametrical studies to evaluate the influence of simulation inputs on the expected residual stress field and by modeling the conditions of real physical systems to allow the comparison between numerical and experimental results. Thermo-mechanical analysis were performed using the software Abaqus. Abaqus AM module has an automated interface that allows the user to define event data, such as element activation and heat input, as a function of both position and time.

INEGI partnered with Faculty of Science and Technology of University of Coimbra to develop a project called "MAMTool - Machinability of Additive Manufactured Parts for Tooling Industry", which consists on the characterization of the residual stresses of two physical specimens produced by Powder Bed Fusion: a quadrangular right prism and a benchmark bridge. A comparison between the numerical and the experimental data was conducted, allowing final conclusions on the accuracy of the developed model. In general, the numerical model over predicted the values of the residual stresses.

Lastly, the displacement field was analysed when the benchmark bridge was gradually removed from its baseplate and compared to experimental results. In this case, the numerical and experimental results were very similar.

Keywords: Finite Element Method, Powder Bed Fusion, Direct Energy Deposition, Metallic Additive Manufacturing, Residual Stresses

This page was intentionally left blank.

Resumo

O fabrico aditivo de metais tem despertado o interesse nas áreas da investigação e da indústria nos últimos anos. Devido a melhorias contínuas, estas técnicas são agora capazes de produzir peças de alta resistência e com melhores características mecânicas relativamente a peças fabricadas convencionalmente. Por outro lado, estes processos produzem tensões residuais elevadas e anisotrópicas, que podem ter um impacto significativo nas características de fadiga e causar distorções geométricas.

Uma vez que a formação de tensões residuais depende das variáveis de processamento, propriedades do material e geometria da peça, é difícil prever com eficiência o seu comportamento. Desta forma, a necessidade de modelos numéricos que conseguem antecipar com precisão a microestrutura, distorção e tensões residuais de um componente é cada vez maior. A simulação computacional é uma ferramenta útil no auxílio ao trabalho experimental e para reduzir a quantidade de tempo e dinheiro investidos, no entanto, o processo de simulação é bastante desafiante e apresenta várias limitações.

O principal objetivo desta dissertação é compreender melhor o funcionamento dos programas comerciais de elementos finitos que simulam processos de fabrico aditivo de metais, mais especificamente os processos de *Powder Bed Fusion* e *Direct Energy Deposition*, no contexto de distorções e na e simulação de tensões residuais. Cada uma destas técnicas usa uma fonte de calor que solidifica cada camada num determinado padrão, construindo gradualmente a peça. As tensões residuais e deformações finais são influenciadas pelas características térmicas da peça. A análise termo-mecânica de elementos finitos pode ser utilizada para modelar esses efeitos, permitindo a produção de peças de alta qualidade. O objetivo é atingido através da realização de estudos paramétricos e de convergência que avaliam a influência dos dados da simulação no campo de tensões residuais e pela modelação das condições de sistemas físicos reais. As análises termo-mecânicas foram realizadas no software Abaqus. O módulo Abaqus AM possui uma interface automatizada que permite ao usuário definir eventos como uma função de posição e tempo.

Em parceria com a Faculdade de Ciências e Tecnologia da Universidade de Coimbra, o INEGI desenvolveu um projeto denominado "MAMTool - *Machinability of Additive Manufactured Parts for Tooling Industry*", que consiste na caracterização das tensões residuais de duas peças produzidas por *Powder Bed Fusion*: um prisma quadrangular e uma *benchmark bridge*. Foi realizada uma comparação entre os dados numéricos e experimentais, permitindo tirar conclusões quanto à precisão do modelo desenvolvido. Em geral, o modelo numérico estimou valores de tensões residuais superiores aos dos resultados experimentais.

Por último, o campo de deslocamentos foi analisado quando a *benchmark bridge* foi gradualmente removida do substrato e comparado com resultados experimentais. Neste caso, os resultados numéricos e experimentais são semelhantes.

Palavras-chave: Método dos Elementos Finitos, Powder Bed Fusion, Direct Energy Deposition, Fabrico Aditivo Metálico, Tensões Residuais

This page was intentionally left blank.

Acknowledgements

First and foremost, I would like to thank the supervisor of this dissertation, Professor Marco Parente, for the support, trust, positive spirit and knowledge transmitted over the last months.

Furthermore, I would also like to give a special thanks to the co-supervisor of this dissertation, Professor Abílio de Jesus, for giving me the opportunity to be involved in an innovative project and for the availability and assistance provided throughout this thesis' development.

To Professor Maria José Marques and Professor Castanhola from Center for Physics of the University of Coimbra, for giving access to the data of an experimental study that consisted on the measurements of residual stresses using x-ray diffraction.

To Engineers Jorge Wolfs, Felipe Fiorentin and Tiago Silva, who were always available to help me and give me access to tools and data that were important for this project.

To Engineer Manuel Abarca, for giving me access to a model developed during his dissertation and that was used as a base for this dissertation.

To my family, especially my parents, for all their support, motivation, affection and inspiration. To my brother João, for his patience. To my grandmother and aunt Bitá for their unconditional love.

To Gonçalo, for supporting me during these 5 years, for making me believe when I doubted the most, for never leaving me behind, for being the best partner and friend I could ever have. To Beatriz, Mafalda and Maria, for always making me smile. To Tixa for her advice and therapeutic conversations.

To Carla, Mariana, Filipa, Rita, Ritinha, Vera, Nanda, Taninha and Tânia, for being by my side for so many years, for their unconditional friendship. Friends for life.

To all my 016 friends, for the memories.

This page was intentionally left blank.

Institutional acknowledgements

The Add.Strength project (Reference PTDC/EME-EME/31307/2017) entitled “Enhanced Mechanical Properties in Additive Manufactured Components” funded by the Programa Operacional Competitividade e Internacionalização (POCI), and Programa Operacional Regional de Lisboa funded by FEDER and National Funds (FCT) is acknowledged. The BIC scholarship funded by the Add.Strength project is also acknowledged.

The MAMTool project (Reference PTDC/EME-EME/31895/2017) entitled “Machinability of Additive Manufactured Parts for Tooling Industry” funded by the Programa Operacional Competitividade e Internacionalização, and Programa Operacional Regional de Lisboa funded by FEDER and National Funds (FCT) is acknowledged.

The ADDing project (Reference POCI-01-0145-FEDER-030490) entitled “Multi-scale Modelling of ADDitive Manufacturing by Direct Energy Deposition of Metallic Powders” funded by the Programa Operacional Competitividade e Internacionalização, and Programa Operacional Regional de Lisboa funded by FEDER and National Funds (FCT) is acknowledged.

The project “GEAR3D: Reconstrução 3D de dentes de engrenagens de grande dimensão via deposição direta por laser” (Reference POCI-01-0247-FEDER-039848) co-funded by FEDER through POCI is acknowledged.



Cofinanciado por:



UNIÃO EUROPEIA
Fundo Europeu
de Desenvolvimento Regional



This page was intentionally left blank.

Contents

1	Introduction	1
1.1	Framework and motivation	1
1.2	Objectives	2
1.3	Outline	3
2	Literature Review	5
2.1	Additive Manufacturing	5
2.1.1	Definition	5
2.1.2	Process description	6
2.1.3	Classification	7
2.1.4	Metal Additive Manufacturing	8
2.1.5	Powder Bed Fusion	11
2.1.6	Direct Energy Deposition	13
2.1.7	Process Parameters	15
2.1.8	Mechanical considerations	18
2.1.9	Design for AM	21
2.1.10	Hybrid AM	24
2.1.11	Applications	26
2.2	Finite Element Method	31
2.2.1	Introduction	31
2.2.2	FEM within AM	32
2.2.3	Commercial software packages	39
3	Simulation Details and Methods	47
3.1	Introduction	47
3.1.1	Physical specimens	47
3.1.2	Material Definition	50
3.2	Thermo-mechanical Simulations	54
3.2.1	Thermo-mechanical analysis of PBF process	54
3.2.2	Thermo-mechanical analysis of LDED-type processes	56
3.2.3	Toolpath and scanning strategy	57
3.2.4	Level of fidelity	58
3.2.5	Boundary conditions and interactions	59
3.2.6	Printing parameters	59
3.2.7	Cooling	60
3.2.8	Mesh	60
3.3	Parametric analysis	60

4	Results and Discussion	63
4.1	Parametric simulations	63
4.2	Mesh size	64
4.3	Scanning strategy	69
4.4	Preheat Temperature	71
4.5	DED results	73
4.6	Comparison between the PBF and DED results	76
4.7	Benchmark bridge	78
4.8	Comparison between the numerical and experimental results	84
4.8.1	Prism	84
4.8.2	Benchmark bridges	87
4.9	Deflection analysis	89
5	Conclusions and Future Work	93
5.1	Conclusions	93
5.2	Future work	95
	References	97

Notation

Acronyms

AM	Additive Manufacturing
MAM	Metal Additive Manufacturing
PBF	Powder Bed Fusion
DED	Direct Energy Deposition
CAD	Computer Aided Design
STL	Standart Tessellation Language
ASTM	American Society for Testing and Materials
BJ	Binder Jetting
SL	Sheet Lamination
VP	Vat Photopolymerization
MJ	Material Jetting
ME	Material Extrusion
LOM	Laminated Object Manufacturing
SLA	Stereolithography
DLP	Direct Light Processing
UV	Ultra Violet
SLM	Selective Laser Melting
FDM	Fused Deposition Modeling
FFF	Fused Filament Fabrication
LPBF	Laser Powder Bed Fusion
EBPBF	Electron Beam Powder Bed Fusion
LDED	Laser Direct Energy Deposition
EBDED	Electron Beam Direct Energy Deposition
GMA-DED	Gas Metal Arc Direct Energy Deposition
GTA-DED	Gas Tungsten Arc Direct Energy Deposition
PA-DED	Plasma Arc Direct Energy Deposition
WAAM	Wire Arc Additive Manufacturing
HAZ	Heat-Affected Zone
TO	Topology Optimization
ESO	Evolutionary Structural Optimization
LSM	Level Set Method
FEM	Finite Element Method
FEA	Finite Element Analysis
FE	Finite Element
SSF	Strain Scaling Factor
LAM	Laser Additive Manufacturing

LMD	Laser Melting Deposition
BC	Boundary Condition
J-C	Johnson-Cook

List of Symbols

d	Depth of the melt pool
L_t	Layer thickness
s	Hatch spacing
ψ_j	Shape function defined in node j
N_n	Total number of nodes
Ω_e	Domain of the shape function
\mathbf{X}	Spatial coordinates
t	Time
Q	Body heat source
ρ	Density
C_p	Specific heat
k	Conductivity
T	Temperature
P	Laser power
η	Absorption efficiency
f	Weighting fraction
a	Ellipsoid's longitudinal measurement
b	Ellipsoid's transverse measurement
c	Ellipsoid's pool depth measurement
q_{rad}	Thermal radiation
q_{conv}	Convective heat loss
h	Convective heat transfer coefficient
ζ	Surface emissivity
σ_b	Stefan-Boltzmann constant
T_S	Surface temperature
T_{env}	Environment temperature
σ	Cauchy stress
C	Fourth-order elastic stiffness matrix
ϵ	Total strain tensor
ϵ^p	Plastic strain tensor
ϵ^T	Thermal strain tensor
\mathbf{f}	Nodal force vector
\mathbf{B}	Deformation matrix
\mathbf{D}	Constitutive matrix
\mathbf{u}	Displacement vector
\mathbf{K}	Stiffness matrix
ϵ_{tot}	Total strain
ϵ_e	Elastic strain
ϵ_{inh}	Inherent strain
k	Thermal conductivity

ϵ^{eig}	Eigenstrain
ϵ_0^{eig}	Value of the eigenstrain at the beginning of the increment at which the element is activated
t_{act}	Activation time
τ_{eig}	User-specified time constant
ξ_s	Start point
ξ_e	End point
t_s	Start Time
t_e	End time
m	Number of intersections
v_f	Volume fraction
A	Area

This page was intentionally left blank.

List of Figures

2 Literature Review

Figure 2.1:	3DP process chain	7
Figure 2.2:	Classification of metal additive manufacturing processes	8
Figure 2.3:	MAM processes and their commercial machine supplier names.	10
Figure 2.4:	Schematic representation of the working principle of (a) Laser powder bed fusion (LPBF) and (b) Electron beam powder bed fusion (EBPBF).	11
Figure 2.5:	Schematic illustration of LPBF	12
Figure 2.6:	Schematic representation of the working principle of (a) Laser direct energy deposition (LDED); (b) Electron beam direct energy deposition (EBDED); (c) Gas metal arc direct energy deposition (GMA-DED); (d) Gas tungsten arc direct energy deposition (GTA-DED) and (e) Plasma arc direct energy deposition (PA-DED).	14
Figure 2.7:	Schematic showing depth of the melt pool (d), layer thickness (L_t), bead spacing/step over/hatch spacing (s) and heat-affected zone (HAZ) (h).	16
Figure 2.8:	Classification of residual stresses.	19
Figure 2.9:	Mechanisms of stress and plastic deformation development during AM: a) during heating and thermal expansion of new layer and b) during cooling and thermal contraction of new layer.	19
Figure 2.10:	Effects of residual stress in AM parts: a) reduced fatigue properties due to internal stress, b) distortion upon baseplate removal and c) potential for process errors due to plastic deformation.	20
Figure 2.11:	Schematic of (a) interlayer porosity and (b) intralayer porosity.	21
Figure 2.12:	Aerospace bracket designed by TO and manufactured by AM.	22
Figure 2.13:	Influence of build orientation on a generic dogbone.	23
Figure 2.14:	Classification of hybrid manufacturing processes.	24
Figure 2.15:	Hybrid AM components: valve body (left) and injection mold (right) produced by DMG Mori.	25
Figure 2.16:	System sales revenue by industry 2019.	26
Figure 2.17:	Copper Heatexchanger Demopart (left) and Copper Combustion Chamber (right) produced by DMLS.	27
Figure 2.18:	ArianeGroup's engine component for Ariane 6 (left) and Satellite bracket from RUAG (right).	27
Figure 2.19:	SLM Ti based frontal skull implant (C) and mandibular implant (D). Courtesy of the Centre for Rapid Prototyping and Manufacturing, Central University of Technology, Free State, South Africa.	28

Figure 2.20:	Orthopaedic Knee Implant by SLM Solutions.	28
Figure 2.21:	PBF cooling die designed with conformal cooling channels to optimize heat transfer rate.	29
Figure 2.22:	Tooling insert equipped with conformal cooling channels	30
Figure 2.23:	Die-casting mold insert with conformal cooling channels by SLM Solutions	30
Figure 2.24:	The Goldak expression for energy distribution from a laser source.	34
Figure 2.25:	Schematic showing the subroutine model deposition of material.	38
Figure 2.26:	Point, infinite line and box toolpaths.	40
Figure 2.27:	Point toolpath-mesh intersection.	41
Figure 2.28:	Infinite line toolpath-mesh intersection.	41
Figure 2.29:	Box toolpath-mesh intersection using the sub-segment approach.	42
Figure 2.30:	A scan pattern with four patches with local orientations rotated by 90° , 0° , 135° and 45°	44
Figure 2.31:	Scan pattern overlaid on an element.	45
3	Simulation Details and Methods	
Figure 3.1:	Prism dimensions and coordinate system (dimensions in millimetres).	48
Figure 3.2:	Benchmark bridge and coordinate system.	48
Figure 3.3:	Bridge dimensions (in millimetres).	49
Figure 3.4:	Behaviour of the five J-C's models and the experimental study of AISI 316L.	53
Figure 3.5:	Progressive element activation for LDED process.	57
4	Results and Discussion	
Figure 4.1:	Representation of the analysed nodes on the $z=20$ plane.	63
Figure 4.2:	Representation of the analysed nodes on the xz plane.	64
Figure 4.3:	Abaqus' mesh refinement of the prism and substrate (von Mises distribution).	65
Figure 4.4:	Evolution of the σ_{xx} and σ_{yy} stresses throughout the $z=20$ plane.	65
Figure 4.5:	Evolution of σ_{xx} stresses throughout the $y=0$ plane.	66
Figure 4.6:	Evolution of σ_{zz} stresses throughout the $y=0$ plane.	67
Figure 4.7:	σ_{xx} stress distribution, extracted from $y=5$ plane in the prism.	68
Figure 4.8:	σ_{yy} stress distribution, extracted from $y=5$ plane in the prism.	68
Figure 4.9:	σ_{zz} stress distribution, extracted from $y=5$ plane in the prism.	68
Figure 4.10:	Representation of the four used orientations: 0° , 120° , 240° and 90°	69
Figure 4.11:	Evolution of the σ_{xx} and σ_{yy} stresses throughout the $z=20$ plane (laser scan strategy effect).	70
Figure 4.12:	Evolution of σ_{xx} stresses throughout the $y=0$ plane (laser scan strategy effect).	70
Figure 4.13:	Evolution of σ_{zz} stresses throughout the $y=0$ plane (laser scan strategy effect).	71
Figure 4.14:	Evolution of the σ_{xx} and σ_{yy} stresses throughout the $z=20$ plane (preheat temperature effect).	72

Figure 4.15:	Evolution of σ_{xx} stresses throughout the $y=0$ plane (preheat temperature effect).	72
Figure 4.16:	Evolution of σ_{zz} stresses throughout the $y=0$ plane (preheat temperature effect).	73
Figure 4.17:	Evolution of the σ_{xx} and σ_{yy} stresses throughout the $z=20$ plane, extracted from the DED model.	74
Figure 4.18:	Evolution of σ_{xx} stresses throughout the $y=0$ plane, extracted from the DED model.	74
Figure 4.19:	Evolution of σ_{zz} stresses throughout the $y=0$ plane, extracted from the DED model.	75
Figure 4.20:	σ_{xx} stress distribution of the DED model, extracted from $y=5$ plane.	75
Figure 4.21:	σ_{yy} stress distribution of the DED model, extracted from $y=5$ plane.	75
Figure 4.22:	σ_{zz} stress distribution of the DED model, extracted from $y=5$ plane.	76
Figure 4.23:	Comparison between the evolution of the σ_{xx} and σ_{yy} stresses throughout the $z=20$ plane (PBF and DED).	76
Figure 4.24:	Comparison between the evolution of σ_{xx} stresses throughout the $y=0$ plane (PBF and DED).	77
Figure 4.25:	Comparison between the evolution of σ_{zz} stresses throughout the $y=0$ plane (PBF and DED).	77
Figure 4.26:	Representation of the analysed nodes on the the xy plane.	78
Figure 4.27:	Evolution of σ_{xx} stresses on the bridge's prominences.	78
Figure 4.28:	Evolution of σ_{yy} stresses on the bridge's prominences.	79
Figure 4.29:	Evolution of σ_{xx} stresses on different levels.	79
Figure 4.30:	Evolution of σ_{yy} stresses on different levels.	80
Figure 4.31:	σ_{xx} distribution on the benchmark bridge, extracted from $y=2.5$ plane.	80
Figure 4.32:	σ_{yy} distribution on the benchmark bridge, extracted from $y=2.5$ plane.	81
Figure 4.33:	σ_{zz} distribution on the benchmark bridge, extracted from $y=2.5$ plane.	81
Figure 4.34:	σ_{xx} distribution on the benchmark bridge using a different scanning strategy.	82
Figure 4.35:	σ_{yy} distribution on the benchmark bridge using a different scanning strategy.	82
Figure 4.36:	Bridge σ_{xx} stress distribution using a different scanning strategy, extracted from $y=2.5$ plane.	83
Figure 4.37:	Bridge σ_{yy} stress distribution using a different scanning strategy, extracted from $y=2.5$ plane.	83
Figure 4.38:	Bridge σ_{zz} stress distribution using a different scanning strategy, extracted from $y=2.5$ plane.	83
Figure 4.39:	Evolution of the σ_{xx} and σ_{yy} stresses throughout the xy plane (Numerical <i>vs.</i> Experimental).	84
Figure 4.40:	Evolution of the σ_{yy} and σ_{zz} stresses throughout the $x=0$ plane (Numerical <i>vs.</i> Experimental).	85
Figure 4.41:	Stress distributions extracted from $x=25$ plane.	85
Figure 4.42:	Evolution of σ_{xx} stresses throughout the xz plane (Numerical <i>vs.</i> Experimental).	86

Figure 4.43:	Evolution of σ_{zz} stresses throughout the xz plane (Numerical <i>vs.</i> Experimental).	86
Figure 4.44:	Printed benchmark bridges (November 2019).	87
Figure 4.45:	Evolution of σ_{xx} stresses on the bridges' prominences.	88
Figure 4.46:	Evolution of σ_{yy} stresses on the bridges' prominences.	88
Figure 4.47:	Wire-cut EDM process used on the bridges.	89
Figure 4.48:	Measuring points of the experimental study.	89
Figure 4.49:	Experimental and numerical comparison between vertical deflection u_{zz} after leg removal.	90
Figure 4.50:	Displacement u_{zz} of the bridge with geometrical scale of 10.	90
Figure 4.51:	Bridge deflection after EDM process.	91

List of Tables

2 Literature Review

Table 2.1:	Critical parameters that control DED and PBF processes [1]. . . .	16
------------	-------------------------------------------------------------------	----

3 Simulation Details and Methods

Table 3.1:	Machine settings used in the AM process of the prism.	49
Table 3.2:	Machine settings used in the AM process of the benchmark bridge.	50
Table 3.3:	Chemical composition, in wt.%, of type 316L austenitic stainless steel [2].	50
Table 3.4:	Latent heat properties [3].	51
Table 3.5:	Thermo-physical properties of AISI 316L steel [4].	51
Table 3.6:	Young's modulus of AISI 316L steel [4].	52
Table 3.7:	AISI 316L's material constants for J-C constitutive model [5]. . . .	52
Table 3.8:	Thermo-physical properties of 18Ni300 maraging steel [4].	54
Table 3.9:	Maraging steel's material constants for J-C constitutive model [6].	54
Table 3.10:	Goldak's spatial energy distribution parameters [7].	59
Table 3.11:	Description of the performed simulation's conditions.	61

4 Results and Discussion

Table 4.1:	Residual stresses at the midpoint of xy plane ($x=25$).	65
Table 4.2:	Residual stresses of the different scanning strategies at a reference point ($x=40$).	74

This page was intentionally left blank.

Chapter 1

Introduction

1.1 Framework and motivation

3D printing is a revolutionary technology that has quickly evolved over the years, which led to a great interest from several industries, such as chemical, food, textile, aerospace, medical and automotive.

In conventional methods such as forming, casting and injection, very complex geometries and objects with more than one material cannot be obtained, due to the inability of the tool used. In 3D printing, however, the parts are constructed by adding material, therefore, when compared to conventional processes, 3D printing technologies promote optimization in terms of cost effectiveness, automation and flexibility [8]. Due to additive manufacturing (AM) powerful personalized manufacturing capabilities, shackles of conventional manufacturing techniques have been broke. This played a major role in advanced manufacturing industry, increasing application prospects in aerospace, mechatronics, medicine and civil engineering [9].

AM processes differ from each other in several factors, namely, in the material used and in the ways in which the layers are created and joined together. These parameters directly influence characteristics such as production time, process precision, mechanical properties of the parts and the need for post-processing. In these processes, a wide range of materials can be used including metals, composites, ceramics and plastics, with the possibility of using more than one material in a piece in order to optimize its structure and improve mechanical properties. There is also great interest to develop biocompatible materials and machines that can obtain multicolored parts [10].

Since its inception, Metal Additive Manufacturing (MAM) has grown enormously and continues to show excellent prospects for the future. This technology is mostly used for research, prototyping or advanced applications in the aerospace sector, as well as in the automotive, tooling and biomedical industries, since it promotes the production of high geometric complexity parts [11].

MAM generally consists of melting metallic raw material (powder or wire) using an energy source, usually a laser or an electron beam. The molten material is transformed layer by layer to form a solid part. Powder Bed Fusion (PBF) and Directed Energy Deposition (DED) are most commonly used among MAM techniques, having the ability to manufacture fully dense high-quality components. In PBF processes, thermal energy selectively fuses regions of a powder bed, while in DED, the materials are fused by melting as they are being deposited using focused thermal energy [12].

For more than a decade, researchers have been focused on monitoring and controlling metal additive processes, to both enhance and ensure part quality and reliability. However, due to the complexity of the additive process physics, which differs over several temporal and spatial scales, such attempts have proved difficult. Exquisite material control is provided by the melting and solidification of material on local scales.

Factors such as changes in spatters, plume dynamics, local and global thermal histories, and boundary conditions affect the resulting material structures and properties. In existing metal machines, process monitoring and control is limited since it is difficult at any moment in the construction process, specially during a full building cycle, to track and capture all of these process inputs. To date, research to classify sections of outlier activity has focused mainly on identifying process abnormalities [13].

Due to the use of AM parts in structural applications, many commercial software packages have been developed to predict these defects and to research their consequences. Accurate numerical solutions, while not replacing experimental data entirely, can provide informations about how a fully printed component behaves.

Therefore, knowledge that includes the basic formulation of the finite element method in the AM problem, more precisely a thermo-structural analysis of components produced by DED and PBF, is the motivation of this thesis.

1.2 Objectives

The main goal of this dissertation is to perform a thermo-structural analysis of components manufactured by PBF using the finite element method through Abaqus, in order to understand the causes of residual stresses and the effects of different parameters on their magnitude. These results will then be compared to experimental values obtained from an experimental study conducted on ongoing INEGI's research projects, with the objective of characterizing the residual stresses of parts produced by PBF.

Although an experimental study of parts obtained by DED was not performed within the scope of this dissertation, one of the objectives of this work is to develop a numerical model of this process in order to compare the numerical values of residual stresses on parts produced by PBF and DED.

This is accomplished by reviewing current literature on numerical calculations of distortions in AM parts, as well as analysing the results of parametric and convergence studies that examine the impact of mesh refinement and process parameters.

The summary of the simulations performed is as follows:

- Mesh convergence studies, in which the in-plane mesh fineness (number of elements per numerical layer) of a component is adjusted using user-defined parameters;
- Comparison of different laser scanning strategies using a prism component to understand the impact of this parameter on the residual stresses;
- Study of the influence of different preheat temperatures;
- Comparison of the two AM processes (PBF and DED) in order to provide insight into the differences between the two models;
- Simulating the printing process of the components based on known process parameters, using meshes that converged in prior simulations, and comparing the results to known experimental data.
- Simulating the removal process of a benchmark bridge and comparison to experimental values.

1.3 Outline

In this Section, the contents of the remaining Chapters of this document are summarised.

Chapter 2 - This chapter is focused in exploring the principles required to comprehend the developed work, such as additive manufacturing and the finite element method;

Chapter 3 - The developed simulations are presented and discussed, with specifics on the utilized software package, process parameters, material description and component geometry;

Chapter 4 - The numerical solutions to the simulations discussed in the previous chapter are detailed and a discussion is conducted;

Chapter 5 - Final remarks on the developed work, as well as possible future works that enhance the knowledge of additive manufacturing simulation are presented.

This page was intentionally left blank.

Chapter 2

Literature Review

This chapter intends to introduce the reader to appropriate information about the relevant technologies and topics applied in this thesis. The chapter includes an introduction to the concept of Additive Manufacturing, as well as a description of this technology's different categories. Metal AM processes are deeply explored, as they are the main focus of this thesis. Applications of AM on various industries are also presented in this chapter. This is followed by an introduction to the Finite Element Method and its many applications on AM processes simulations.

2.1 Additive Manufacturing

2.1.1 Definition

Additive Manufacturing is characterized as a process that uses a heat source and filler material to directly produce parts or components constructed from a solid model. The solid model is sliced into several layers, creating a toolpath to trace the individual layers, and then, building the part layer-by-layer in a computer-controlled automated system using the filler material. It is called an additive process since the method relies on material addition in each layer until the final geometry of the component is obtained. A traditional machining process, on the other hand, starts with a material block and consists on material removal until the geometry of the final part is established, hence being called a subtractive process.

Even though 3D printing and AM are frequently used as synonyms, AM actually involves other techniques besides 3D printing, such as material addition for the purpose of repair, remanufacturing and property improvement of existing parts or components. This technology's major advantages over traditional production processes are its ability to create components directly from CAD data, decreasing the need for a tool or die and allowing for a substantial reduction in design-to-production time, as well as reducing the production cost of low volume parts, which is not feasible in casting or injection, for example, due to the high cost of molds. Furthermore, AM provides a higher degree of design freedom and

allows the development of geometries that are not at all achievable through traditional manufacturing. As components are becoming more and more engineered and complex, this technology provides the manufacturing industry with a great alternative to conventional processes and encourages innovation by reducing the time needed for new products to be marketed, even though it is not yet suitable for high-volume manufacturing [14].

2.1.2 Process description

In order to reduce the amount of human labor and the errors that come with it, the AM process can be divided into eight stages, some of which are represented in Figure 2.1 [15]:

1. 3D CAD modeling of the component: parts must start from a software model that fully describes the external geometry, which can be generated through CAD or by optical scanning of an existing workpiece.
2. Conversion from CAD to STL format: the geometry of a surface is described by the use of triangular facets and this information is stored by the use of the triangles' vertices and the respective normal vectors. The greater the number of triangles created for the geometric representation of the surface, the greater the execution time and the precision of the process.
3. Transfer to AM machine and STL file manipulation: the model is divided into successive layers of material.
4. Machine setup: prior to the construction process, settings such as mechanical properties of the material, printing time, sources of energy and power, the thickness of the layers, scanning strategy and the type of supports to be used, so that the part does not lose its shape during cooling, must be properly set up. All of these aspects will determine the dimensional accuracy and the quality of the parts' surfaces: for example, the thinner the layers are, the more accurate the final result will be when compared to the numerical model.
5. Construction: the construction of the part is primarily an automated process and without supervision. At this time, only superficial machine monitoring is required to ensure that no errors have occurred, such as running out of material or software glitches.
6. Removal: the part is removed from the machine when it is complete and cooled. This stage can include contact with the system, which may have safety devices to ensure, for example, that the operating temperatures are sufficiently low.
7. Post-processing: parts may need a certain amount of additional cleaning after being removed from the machine. At this point, components may be fragile or have construction supports that must be removed, which requires time and careful experienced manual manipulation.

8. Finishing: one of the characteristics that is associated with these processes is a high surface roughness. However, in order to offer an acceptable surface texture, it is possible to carry out finish processes, such as polishing and machining, to improve the mechanical properties of the part. If the finishing criteria are very demanding, treatments can be laborious and long. There may also be the need to assemble the obtained part to a final model or a product with multiple components.

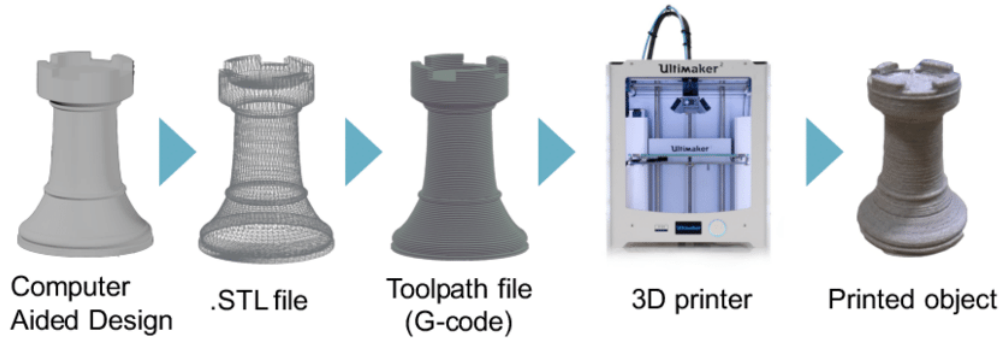


Figure 2.1 3DP process chain [16].

2.1.3 Classification

The EN ISO/ASTM 52921 (2015) standard classifies additive manufacturing processes into seven different categories [10]:

- Binder Jetting (BJ);
- Powder Bed Fusion (PBF);
- Sheet Lamination (SL);
- Direct Energy Deposition (DED);
- Vat Photopolymerization (VP);
- Material Jetting (MJ);
- Material Extrusion (ME).

These technologies are all based on the general concept of multi-layer slicing of a solid model, creating a toolpath for each layer, uploading these data into the computer and building the component up layer-by-layer using a heat source (laser, electron beam, electric arc or ultrasonic energy) and feedstock (powder, wire or thin sheet).

Although polymer printing techniques have progressed over the years, AM technology has been taken to a whole new level by the sophistication of metal AM techniques, which allowed for functional parts to be produced in a large variety of engineering and industrial applications, with similar properties and enhanced performance as conventionally manufactured components [14].

2.1.4 Metal Additive Manufacturing

As represented in Figure 2.2, Metal Additive Manufacturing (MAM) can be divided into two categories: direct and indirect processes, this difference being related to the finality of the parts. Metal built parts are the final products of direct MAM, as they are essentially manufactured according to the design requirements and specifications. On the other hand, in indirect MAM, the built parts consist of master patterns or instruments that are ultimately used by conventional production methods to achieve the required metal parts.

Consequently, indirect MAM primarily resorts to non-metallic materials such as polymers, photopolymers, ceramics, waxes, resins and composites, being unable to disassociate itself from conventional manufacturing processes such as investment casting, sand casting, die casting and injection molding.

Direct MAM includes four of the categories mentioned previously: BJ, SL, PBF and DED. The remaining categories (VP, MJ and ME) are considered to be indirect MAM, since they are mainly used to build polymer and highly-filled polymer parts made from mixtures of metals or ceramic powders with polymers. At the moment, there is little evidence that these processes can be used to fabricate pure or alloyed metal components [10].

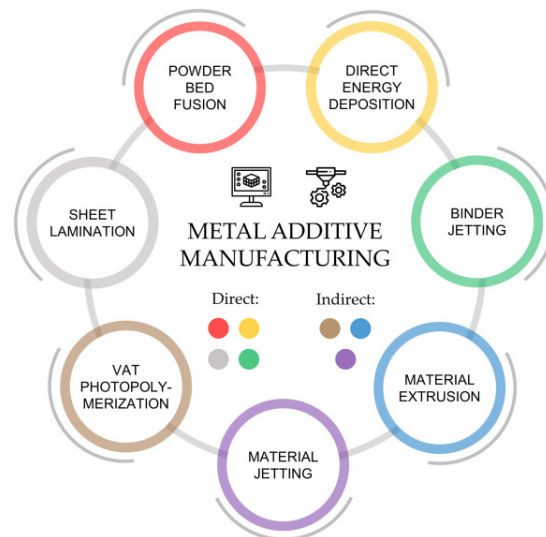


Figure 2.2 Classification of metal additive manufacturing processes [10].

Binder Jetting uses a binder to unite the layered metal powder and, then, the part is sintered in an oven to remove binders and infiltrate the pores with liquid metal. This process distinguishes itself from the other technologies by not using a heat source during the building process. Some advantages associated to this category are the fact that it eliminates the need for a build plate since the pieces are supported by the loose powder in the job box, having spreading rates that outperform those of other processes and being able to print large sections, often in a more cost effective way than other AM techniques [1].

Sheet Lamination uses thin sheets of metal placed one on top of the other, layer-by-layer and joined together using an ultrasonic process based on CAD data [14]. Laminated Object Manufacturing (LOM) was one of the first commercialized AM techniques, which involved lamination of paper material sheets, cut using a CO₂ laser. A variety of other processes have been developed based on the concept of SL, involving other building materials and cutting methods. These techniques can be further classified based on the mechanism used to establish bonding between layers: gluing or adhesive bonding, thermal bonding, clamping and ultrasonic welding. The use of ultrasonic welding requires specific solid state bonding characteristics and can provide a wide range of applications [15].

Vat Photopolymerization uses a vat of liquid photopolymer resin, from which the model is built, and UV light to cure or harden the resin where it is desired, while the platform moves down the object being constructed after each new layer is cured [14]. This technique includes laser-based processes such as stereolithography (SLA) and direct light processing (DLP). Photopolymers have several disadvantages, including a higher cost than thermoplastics and a lack of structural strength, which causes parts to degrade and deform over time [10].

Material Extrusion involves heating a resin filament, extruding it through a process nozzle and depositing it layer-by-layer on a substrate [14]. Fused Deposition Modeling (FDM) and Fused Filament Fabrication (FFF) are two relevant processes in this category, which are slower and less accurate than other AM methods. Nevertheless, due to the low cost of thermoplastic materials like Nylon and ABS, these processes are widely used for the cost-effective manufacturing of non-functional prototypes [10].

Material Jetting delivers particles of a photosensitive material (liquid thermoset photopolymers) that solidifies under UV light [14]. This process uses the same type of printer head technology as BJ, however, MJ deposits the material directly on the part being produced. Amongst AM technologies, MJ-based methods are the most precise, capable of creating smooth surfaces with fine details and high accuracy. The limitations of this process are associated to the cost of photopolymers, their strength limits and the size constraints imposed by long processing run times [10].

Out of all the processes, PBF and DED are the most commonly used technologies for metal AM, having a wide variety of industrial applications unlike the other categories. Figure 2.3 summarizes the different processes included in both DED and PBF, as well as their commercial machine supplier names. In these processes, metal powder or wire are used as the feedstock, which is melted using a heat source such as a laser, electron beam, plasma or gas-metal arc. Important process variables associated to both technologies include the type of heat source, its energy density, the speed rate (designated scan rate in PBF and traverse speed in DED) and the rate of the added feedstock (nominated layer thickness in PBF) [1]. Both these technologies will be deeply explored in the following chapters of this dissertation since the studied specimens were produced by PBF and numerical models of both PBF and DED were developed.

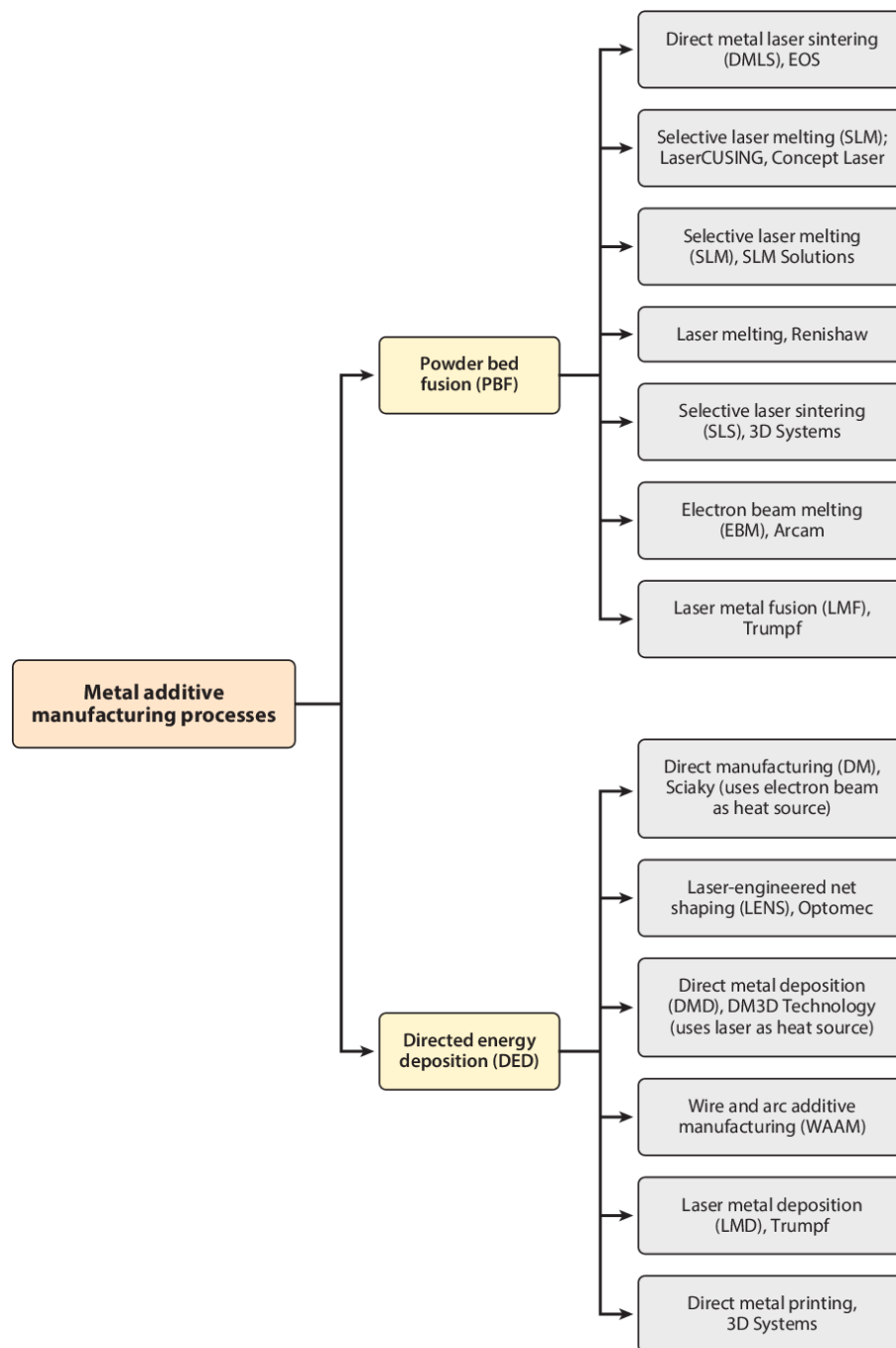


Figure 2.3 MAM processes and their commercial machine supplier names [17].

2.1.5 Powder Bed Fusion

PBF technologies work by layering down metal powder on the build platform, scanning the bed with a heat source (usually a laser or electron beam), that partially or fully melts the powder in the beam's direction, and then, re-solidifying or binding together the powder during the cooling process [1].

This technology involves the following steps that can easily explain the components' production process [1]:

1. A substrate is fixed on the build platform.
2. In order to reduce the oxygen level in the chamber to the desired level, the build chamber is filled with inert gas (for laser processing) or evacuated (for electron beam processing).
3. A thin layer of metal powder, with thickness in the range of 20-200 $[\mu\text{m}]$ (depending on the technology and equipment used), is laid down on the substrate and leveled to a predetermined thickness using a leveling device, for example, a roller or a blade.
4. The heat source scans the powder bed surface, following a toolpath calculated from the component's CAD data.
5. This process is repeated for the subsequent layers until the component is complete.

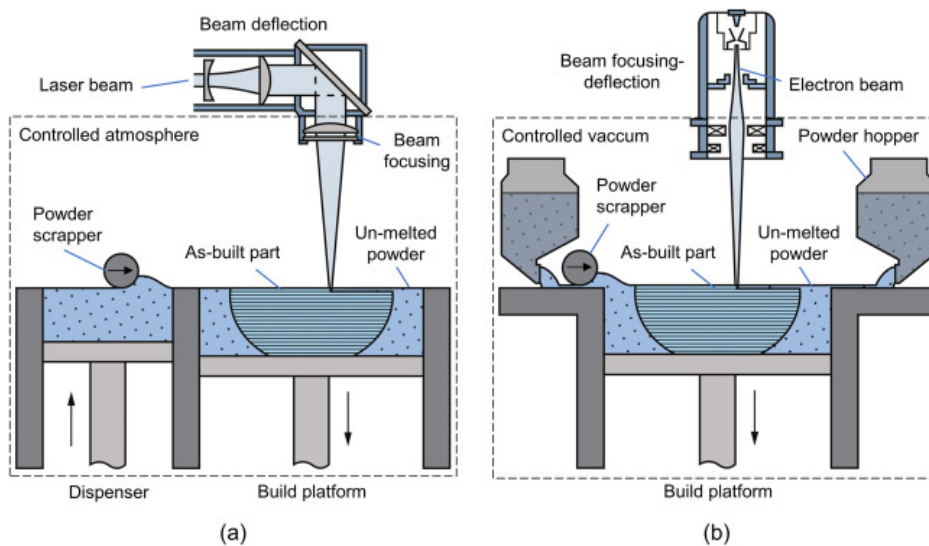


Figure 2.4 Schematic representation of the working principle of (a) Laser powder bed fusion (LPBF) and (b) Electron beam powder bed fusion (EBPBF) [10].

A similar set of characteristics can be associated to all PBF processes, namely, one or more thermal sources for inducing powder particle fusion, a method to regulate powder fusion to a specified region of each layer and mechanisms for adding and smoothing powder layers [15].

This category provides advantages such as free form fabrication without any tools or dies, production of fine-featured high-precision components, construction of overhangs and closed cooling passages, fully dense parts and possibility to successfully use a wide range of materials (300 maraging steels, stainless steels, Ni alloys, Co alloys, Ti alloys, Cu alloys and Al alloys). However, some limitations associated to PBF processes are the production of parts with residual stress that can cause distortion and difficulties in fixing components, adding metal to existing parts and using several materials in a single build [1].

The two PBF-based processes described in Figure 2.4 are Laser Powder Bed Fusion (LPBF) and Electron Beam Powder Bed Fusion (EBPBF), which can be used to produce high resolution complex prototypes and end-use metal parts with low material waste and effective recycling of unmelted powder. The source of thermal energy is what distinguishes them the most, however, laser processes are most commonly used [10].

Laser Powder Bed Fusion

LPBF is one of the oldest MAM processes that uses a laser beam thermal energy source to selectively melt and consolidate the metal powder. Depending on whether the metal is reactive or not, the built chamber is protected by a flow of inert gas (argon or nitrogen) to prevent oxidation. Homogeneous gas flow across the build area is important for the parts' quality and properties since it helps to remove the condensate that is produced by melting the powder. Reflective mirrors are also used to pass the laser beam along a pre-defined two-dimensional scanning path, as illustrated in Figure 2.5 [10, 18]. The most well known process included in this category is Selective Laser Melting (SLM).

Due to the widespread use of this method and the continuous development of equipment by manufacturers, deposition rates of up to 0.1 [kg/h] and surface roughness in the range of 10-20 [μm] are now achievable. To monitor the quality of a component built by powder bed processes, it is necessary to achieve a homogeneous thickness of powder in each sheet [10, 18].

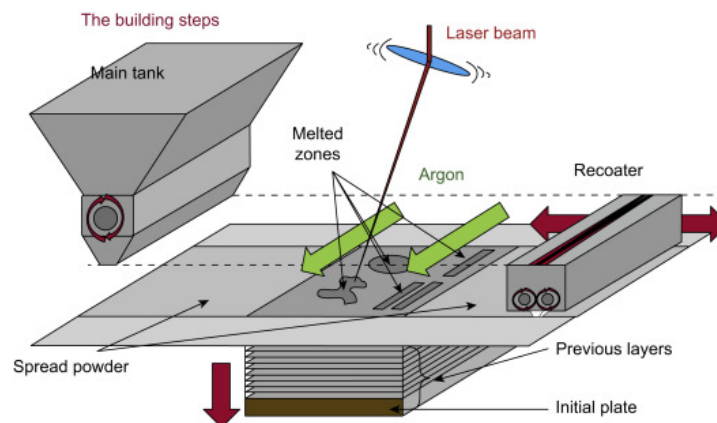


Figure 2.5 Schematic illustration of LPBF [18].

Electron Beam Powder Bed Fusion

EBPBF process is similar to LPBF with the exception that the source of thermal energy used to melt the powder is an electron beam rather than a laser beam. Since the electron beam is generated under controlled vacuum conditions and is focused and deflected by electromagnetic lenses rather than mirrors, the shift in the thermal energy source requires many other changes in the equipment. To prevent powder spreading caused by electrostatic charging, the feedstock must be preheated to temperatures about 0.5 to 0.6 of its melting point.

This process is not as commonly used as LPBF in both industry and research, nonetheless, it has provided some industrial applications, especially in the processing of difficult-to-process materials such as cobalt and nickel alloys, titanium aluminides, niobium and even cellular materials. Maximum deposition rates are significantly higher than those of LPBF, reaching up to 0.2 [kg/h], with surface roughness ranges of 15-30 [μm] [10].

2.1.6 Direct Energy Deposition

DED processes involve feeding powder or wire through a nozzle onto the build component, where it is melted using a concentrated thermal energy source. Unlike PBF processes, DED avoids using binders and the feedstock flows through a feeding system and melts at the precise time that is being deposited into the substrate's melt pool, rather than remaining stagnant within the build platform during the part's construction [10].

This process can be summarized in 4 stages [1]:

1. A substrate or existing part is placed on the work table.
2. Just like in PBF processes, the machine chamber is closed and filled with inert gas (for laser processing) or evacuated (for electron beam processing).
3. To create a melt pool, in the beginning of the cycle, the process nozzle with a concentric laser, electron beam or gas metal arc focus on the part surface. The material is delivered as powder through a coaxial nozzle (for lasers) or as metal wire with a side delivery nozzle. The melt pool solidifies and forms layers of metal as the nozzle moves away at a constant speed and follows a specified toolpath.
4. Subsequent layers work in the same way, building up the part layer-by-layer until it is complete.

An example of DED unique capabilities is the ability to produce fully dense parts with highly controllable microstructural features. Additionally, this process has the potential to repair and refurbish high-tech components, such as turbine blades that are unreliable or have been subjected to service damage, as well as deposit thin layers of thick, corrosion-resistant and wear-resistant metals on components to optimize their efficiency and lifespan [15].

Unlike PBF, DED enables the production of functionally graded components with composition variations in the x , y , and z directions. Nevertheless, DED processes cannot manufacture structures as complex as PBF processes, since it would require more robust support structures (or multi-axis deposition) to achieve the desired geometries and due to the fact that larger melt pools result in a reduced capacity to produce small-scale features, greater surface roughness and less accuracy [15]. Porosity is one of the most significant defects associated with the mechanical properties of DED components [19]. Furthermore, tight tolerance parts are difficult to achieve and it is impracticable to produce closed cooling passages and wide overhangs [1].

Post-processing of components produced by DED usually involves removing support structures or the substrate and finishing operations are commonly required to achieve better accuracy and surface roughness. Heat treatment may also be needed in order to reduce residual stresses or to achieve the desired microstructure.

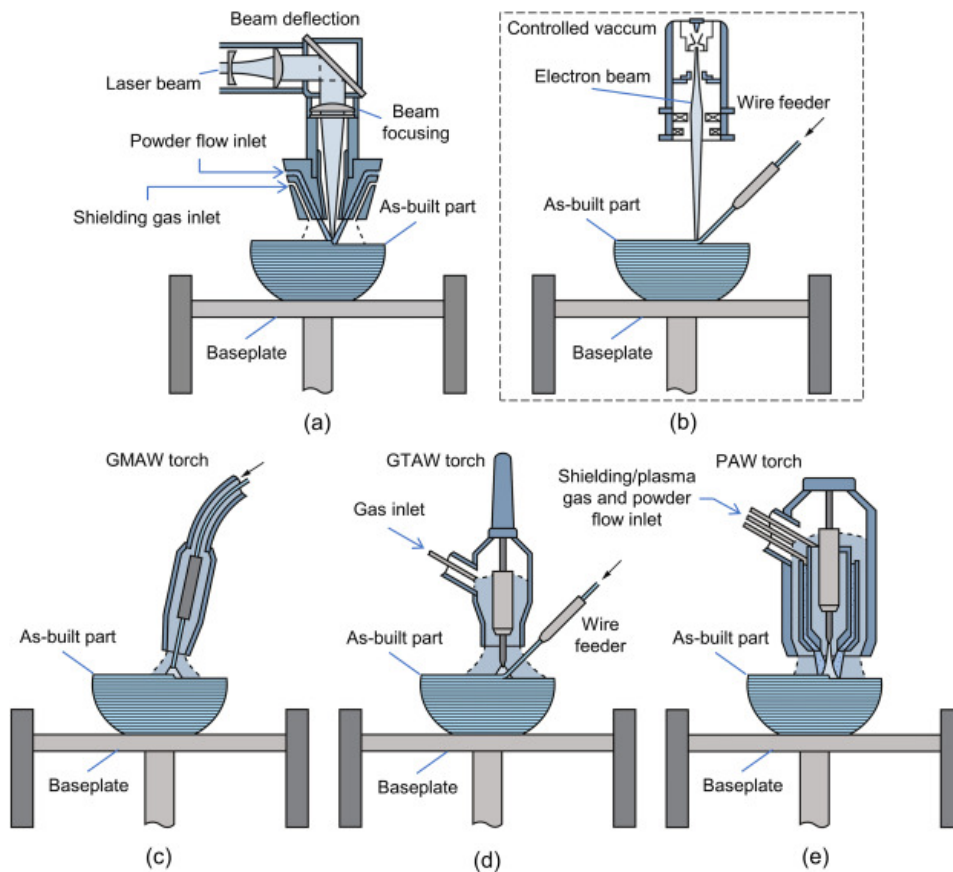


Figure 2.6 Schematic representation of the working principle of (a) Laser direct energy deposition (LDED); (b) Electron beam direct energy deposition (EBDED); (c) Gas metal arc direct energy deposition (GMA-DED); (d) Gas tungsten arc direct energy deposition (GTA-DED) and (e) Plasma arc direct energy deposition (PA-DED) [10].

Figure 2.6 shows a schematic of the various energy sources that can be used to create the melt pool: laser, electron beam, plasma arc, gas-tungsten arc and gas-metal arc. The

sources of thermal energy and the systems used to deliver the feedstock are the major differences between the DED-based processes [10].

Laser Direct Energy Deposition

LDED employs the principles of laser cladding to build metal components layer-by-layer, using powder or wire as feedstock. Powder is segmented and fed through the laser head (usually coaxially), while wire is fed through a separate mechanism. Deposition rates of 2 [kg/h] can be achieved when using wire as feedstock and the surface roughness is usually greater than 30 [μm]. This process does not involve the use of regulated environmental chambers, which enables it to be fully automated in order to improve path motion flexibility [10].

Electron Beam Direct Energy Deposition

Similar to LDED, but using an electron beam to operate under regulated vacuum conditions, EBDED fabricates large-scale parts at deposition rates ranging from 3 to 10 [kg/h], however, fast deposition rates can cause major thermal stresses. Due to poor handling of metal powder flow in vacuum, the process uses exclusively wire as feedstock to avoid possible defects on the components' final quality and accuracy [10].

Wire Arc Additive Manufacturing

WAAM includes processes that use an electric arc as a source of thermal energy and have operating concepts similar to arc welding processes: gas metal arc, gas tungsten arc and plasma arc.

These processes are characterized by deposition rates that can reach values of 5-6 [kg/h], which makes them faster but less accurate than LDED. Nonetheless, since the energy required to convert electrical energy into a laser beam is higher, WAAM-based processes are more efficient than LDED. These processes are appealing to research institutions and industries with their own welding equipment, because the acquisition of the appropriate CNC mechanisms and the installation of the equipment in existing robots makes it relatively simple and affordable to build a MAM device capable of producing large parts over a short period of time [10].

2.1.7 Process Parameters

AM technologies, especially PBF and DED, involve a large number of process parameters. Table 2.1 includes critical parameters that control these two processes, as well as some reference values.

Table 2.1 Critical parameters that control DED and PBF processes [1].

Process Parameter	DED	PBF
Heat source	Type Heat Power [W] Beam size: Laser 0.5-4 [mm] EB/WAAM 5-20 [mm]	Type Heat Power [W] Beam size: 50-400 [μm]
Feedstock	Type Powder size [μm] Particle size distribution: 45-150 [μm] Morphology or wire size [μm] Powder feed rate [g/min] or wire feed rate [m/min] Preheat (wire)	Type Powder size [μm] Particle size distribution: 15-45 [μm] Morphology Layer thickness: 50-200 [μm] Preheat applied to powder bed for some applications
Machine Settings	Traverse speed: 300-2000 [mm/min] Gas type and flow rates [L/min] Chamber environment: inert gas, vacuum, temperature, O ₂ level, humidity level	Scan speed: 1-10 [m/s] Powder cover gas flow rate [L/min] Chamber environment: inert gas, vacuum, temperature, O ₂ level, humidity level
Design/Programming	Deposition layer thickness [μm] Step over: 1-2 [mm] Toolpath strategy	Fused layer thickness [μm] Hatch spacing: 50-200 [μm] Toolpath strategy

Figure 2.7 shows a schematic diagram of a printed metal layer with individual tracks, specifying several process parameters.

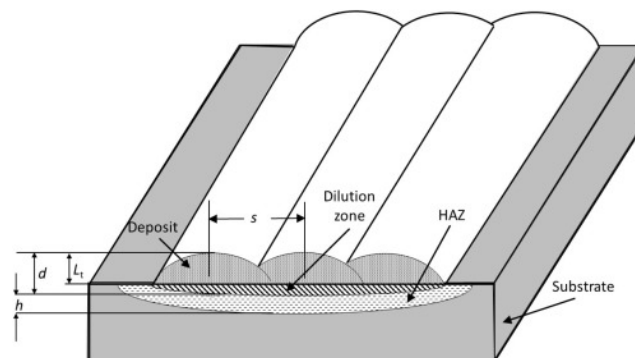


Figure 2.7 Schematic showing depth of the melt pool (d), layer thickness (L_t), bead spacing/step over/hatch spacing (s) and heat-affected zone (HAZ) (h) [1].

Other variables worth mentioning are the laser wavelength, which determines the amount of energy absorbed by the metal, the nozzle design, which determines the shape of the powder beam, and the optical focus [1]. The majority of process variables are highly interdependent and connected with each other.

Multiple lasers have been used in laser-based processes, including CO₂ lasers, diode lasers and fiber lasers. In comparison to CO₂ lasers, metals absorb far more of the shorter wavelengths: diode or fiber lasers of 900-1070 [nm]. As a result, industry is increasingly adopting these lasers as energy sources and shifting away from conventional CO₂ lasers. In terms of beam size, a smaller heat source spot size increases process resolution and fine feature build-up capacity, whereas larger spot sizes yield higher efficiency [1]. Additionally, the required laser power increases with the material's melting point and lower powder bed temperature, as well as being influenced by the powder bed's absorptivity properties [15].

The type of feedstock used in the printing process is crucial. Although wire-fed processes have a near 100% material capture rate, they promote lower feature resolution, fewer material options and are less versatile than powder-fed processes.

Microstructure, part quality and productivity are all influenced by machine parameters such as scan speed/traverse speed, energy density, gas flow rates, machine chamber environment and build plate temperature. In either DED or PBF processes, reactive metals such as Ti, Ta and Mo need the chamber to be filled with, typically, argon gas. Design and toolpath strategy also influence parts quality: in the z direction, a bigger layer thickness yields a better surface finish, unlike the XY plane, where a smaller step over promotes better results [1].

The size of the melt pool is highly dependent on the laser power, scan speed, spot size and bed temperature settings. To ensure solid mechanical properties, scan spacing should be chosen in order to achieve a reasonable degree of melt pool overlap between adjacent lines of fused material. Moreover, changing the scan orientation from layer to layer can be beneficial to reduce residual stress accumulation [15].

The density of the powder bed, which is influenced by powder form, size, distribution and spreading mechanism, has a significant impact on the component's quality. Powder bed densities for most commercially available powders are usually between 50 and 60%. The higher the powder packing density, the better the thermal conductivity of the bed and the mechanical properties of the component [15]. In PBF processes, having a consistent powder layer with uniform powder packing throughout the entire build platform is very important to achieve consistent and high quality products. DED methods, on the other hand, are more adaptable and can handle irregular powders to some degree [1].

To accomplish the best tradeoff between melt pool size, dimensional precision, surface finish, build rate and mechanical properties, factors such as powder bed temperature, laser strength, scan speed and scan spacing must be optimized. In order to obtain repeatable results, the powder bed temperature should be kept uniform and constant. Generally,

high laser power combined with low bed temperatures cause nonuniform shrinkage and the development of residual stresses, resulting in curling of parts.

Powder feed rate, beam power and traverse speed are also connected with each other, for example, raising the feed rate has the same effect as lowering the beam power. Furthermore, because of the shorter dwell time, the input beam energy decreases as the scan speed is increased, resulting in a smaller melt pool on the substrate and a more rapid cooling [15].

2.1.8 Mechanical considerations

Currently, AM methods are capable of manufacturing high strength components with static strengths that are often greater than their conventionally produced counterparts [20]. This technology's specific rapid heating-cooling thermal cycle, which is similar to welding, causes residual stress in the component that can have a significant impact on fatigue properties and result in geometric distortion [21]. Another obstacle associated to AM, besides equipment expense and lack of rigorous qualification standards, is the existence of a wide variety of material defects: gas porosity, keyhole porosity and significant lack-of-fusion defects can occur, depending on the material's properties and processing parameters [20].

Residual Stress

Residual stresses occur when a material is submitted to non-uniform plastic deformation and remains in equilibrium after processing, heating or other alterations. In order to be possible to make safe and reliable predictions of the component's final properties and life, these existing stresses must be taken into account during the production process. The effects of residual stresses are particularly dependent on magnitude and orientation and may either have a negative impact or be beneficial to material efficiency.

When it comes to AM components, though it can be reduced by post-processing heat treatments, the formation of significant residual stresses during the manufacturing process can result in excessive distortion, which can lead to production failure or errors. However, as additional heat treatments extend the process and increase its cost, it is crucial to understand how residual stresses grow in manufactured components [20].

Residual stresses are classified into three types based on their length: type I, residual stresses are on macro-level; type II, also known as micro-scale stresses, are caused by anisotropic material properties on grain scale; and type III, stresses that are caused by coherency and dislocation on the nano-scale [21]. This classification is represented in Figure 2.8.

Types II and III residual stresses have very small impact on mechanical properties and are beyond the reach of most modern measurement methods [21]. Type I anisotropic

stresses have a direct effect on fatigue properties, cause distortion during or after production and also have proven to be directly manipulable by changes in processing conditions [20].

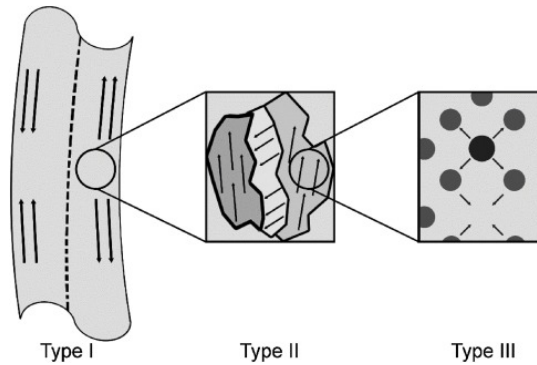


Figure 2.8 Classification of residual stresses [20].

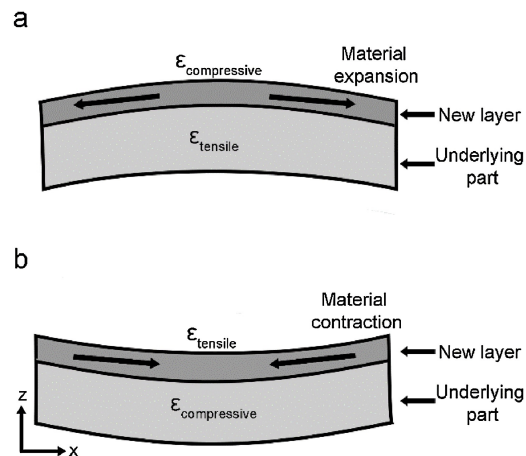


Figure 2.9 Mechanisms of stress and plastic deformation development during AM: a) during heating and thermal expansion of new layer and b) during cooling and thermal contraction of new layer [20].

Considering a simplified example of a component during PBF processing, in which the whole layer is melted instantly, the portion of the section built until a certain stage cools uniformly with a temperature gradient in the z direction. When a new layer is introduced and heated to a temperature well above that of the underlying part, the new layer of material expands uniformly at first. The much cooler underlying part will limit this expansion, resulting in the growth of compressive stresses in the new layer and tensile stresses in the underlying part. When the heat source is removed, the new layer cools rapidly, contracting faster than the cooled part beneath it can handle, causing tensile stresses in the new layer and compressive stresses in the part beneath it [20]. These phenomena are represented on figure 2.9.

The degree and type of residual stress within the build is influenced by thermal conductivity, coefficient of thermal expansion, Young's modulus and yield power, as well as

phase transformations, component's geometry, fabrication process parameters and scanning pattern. Volumetric changes occur during solidification, as well as various solid-state transformations, such as martensitic transformation or precipitations, resulting in residual stresses in the fabricated part and substrate [1].

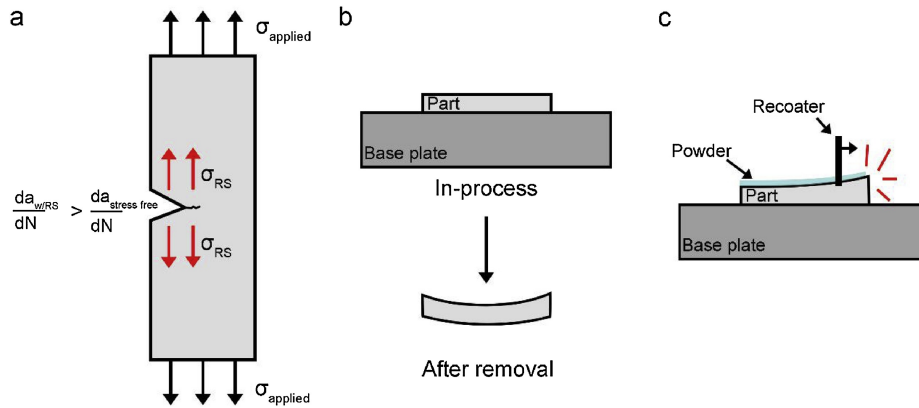


Figure 2.10 Effects of residual stress in AM parts: a) reduced fatigue properties due to internal stress, b) distortion upon baseplate removal and c) potential for process errors due to plastic deformation [20].

Figure 2.10 shows different effects of the residual stresses in AM parts. To relieve or minimize residual stresses, a variety of techniques can be used: preheating the substrate or the initial feedstock to reduce abrupt thermal gradients; in-situ process monitoring with feedback control to tune process parameters on the fly; and ex-situ post-processing techniques, such as heat treatment [19].

Porosity

Porosity in AM parts can have multiple origins, namely, unmelted powder particles, absorbed gases or prior gases present in powder particles, interbead voids due to inappropriate parameter selection, melt pool instability and shrinkage porosity from rapid solidification.

Gas porosities have a spherical shape, typically with a diameter of 5-200 [μm]. These porosities can occur in PBF processes due to entrapped gases in a powder bed if the powder packing density is low, while in DED processes, gas entrapment can happen since process gases blow through the process nozzle itself. Gases can also dissolve in the superheated melt pool causing porosity, which is particularly important for alloys with lower melting points, such as aluminum. Additionally, hollow powders containing entrapped gases from the atomization process may be responsible for this phenomenon as well [1].

Improper selection of process parameters can also affect porosity, for example, porosity formation decreases as the hatch spacing increases, but once it reaches a critical value, it quickly increases again. Shrinkage porosity is another type of porosity found in AM materials, which is determined by the alloy chemistry. As these processes adopt rapid cooling

speeds, materials with a greater solidification range (larger distance between liquidus and solidus temperatures) and higher viscosity are more likely to cause shrinkage porosities [1].

There are two main forms of porosity represented in Figure 2.11: interlayer porosity, that occurs due to a lack of sufficient energy input to melt the filler material, and intralayer porosity, which is linked to the use of inert shielding gas that promotes gas trapping. As a result of the rapid solidification cooling rates, interlayer pores are typically wide, irregular and are often caused by low dilution values. Intralayer pores, on the other hand, are typically spherical in shape and emerge most commonly in regions with slower solidification cooling speeds. The presence of intralayer porosities is referred to as high dilution [19].

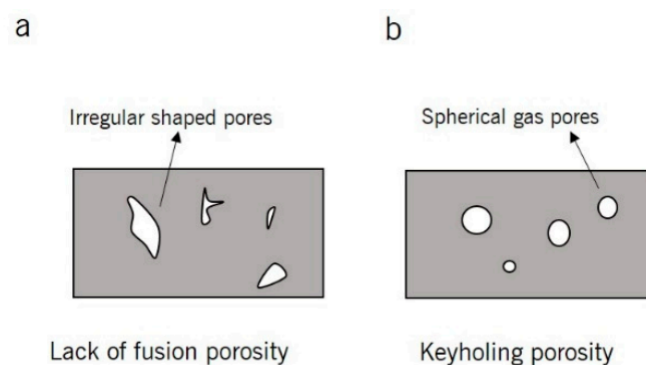


Figure 2.11 Schematic of (a) interlayer porosity and (b) intralayer porosity [19].

In order to monitor the shape and size range of powders, as well as preserve optimum process parameters during deposition, all of these forms of porosity must be considered. Porosity can be both qualitatively and quantitatively measured, using the Archimedes theory, x-ray computed tomography and optical microscopy [19].

2.1.9 Design for AM

When considering the setup of an AM machine, designers and operators should consider a variety of build related factors, including topology optimization, part orientation and supports removal.

Topology Optimization

Optimization approaches aim to optimize a part's design by modifying the values of design variables to achieve desired goals which are usually linked to structural efficiency or weight, while staying within certain constraints. In order to increase complexity and scope, three main types of optimization problems have been developed for design for AM [15]:

- Size optimization: values of dimensions are determined.

- Shape optimization: shapes of part surfaces are changed.
- Topology optimization: distributions of material are explored.

The main differences between these three categories are the starting geometric configuration and variable selection, all of which may contribute to major structural performance improvements [15].

Topology optimization (TO) was created as an advanced structural design technique to develop customized lightweight and high performance configurations that are difficult to achieve using traditional methods. Nonetheless, some limitations of structural design methods for AM include the performance characterization and scale effects of lattice structures, the anisotropy and fatigue performance of materials and issues with functionally graded materials [9].

As structural optimization approaches, finite element analyses are usually performed during each optimization iteration, meaning that TO can be computationally challenging. Consequently, based on the specified loading conditions, TO solutions can result in structures that are nearly completely stressed or have constant strain energy across the structure geometry [15]. Several topology optimization approaches have been proposed over the last three decades, the most popular of which are the density-based approach, the evolutionary structural optimization (ESO) and the level set method (LSM) [9]. Figure 2.12 shows an example of TO of an aerospace bracket, which was then manufactured by AM.

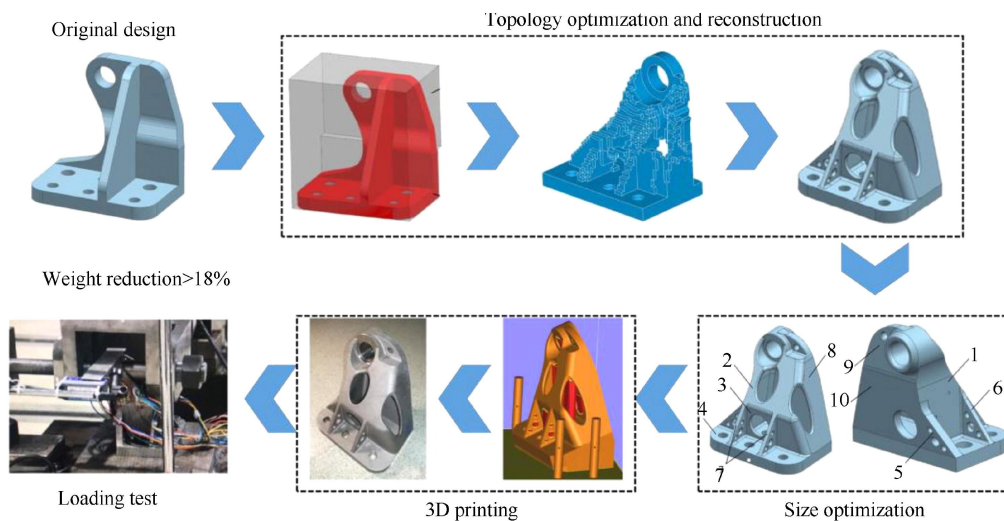


Figure 2.12 Aerospace bracket designed by TO and manufactured by AM [9].

Part Orientation

The part's orientation inside the machine can have an impact on its accuracy. There may not be an optimal orientation for a particular part, as many components will have complex features along different axes. Additionally, it may be more important to preserve the geometry of some features than others, so correct orientation may be a subjective judgment. This decision may also be in contrast with other variables, such as, the amount of time it takes to build a part, whether a particular orientation will produce more supports (can be observed in Figure 2.13) and whether certain surfaces should be built face-up to ensure good surface finish in areas that are not in contact with support structures.

Generally, the performance of upward-facing features in AM is the best, since they are not in contact with the supports required for many methods. The upward-facing features of powder beds are smooth because they solidify against air, while the downward-facing and sideways-facing features solidify against powder, granting them a powdery texture [15].

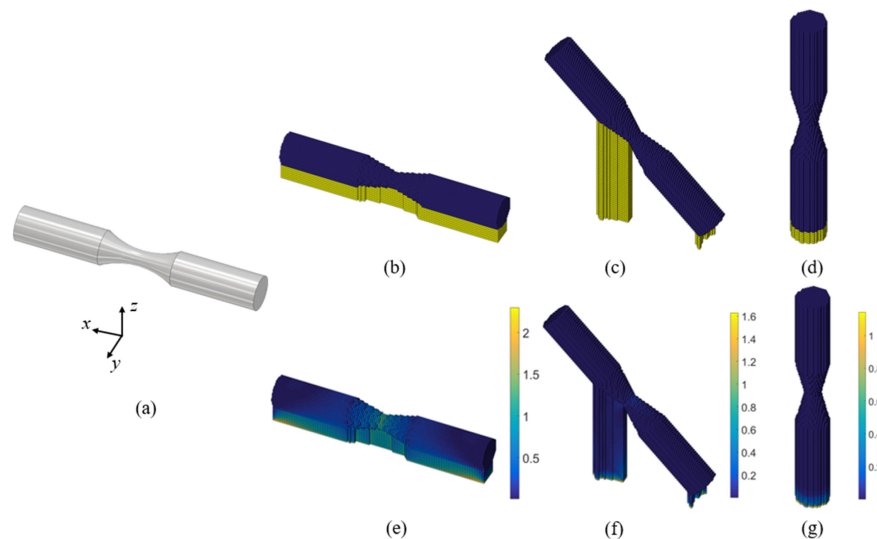


Figure 2.13 Influence of build orientation on a generic dogbone [22].

Support Removal

Despite the fact that the use of support structures is frequently unavoidable, it is best to try to keep the amount as low as possible since there will be small marks where the supports touch the component, which leads up to further part cleanup and post-process finishing. Nevertheless, as certain surfaces can be less critical than others, the component positioning must be balanced against the relative value of an affected surface. Furthermore, removing too many supports can result in the part being disconnected from the baseplate and moving around during subsequent layering [15].

2.1.10 Hybrid AM

Hybrid AM processes combine AM with one or more secondary processes or energy sources that affect a component's efficiency, functionality and process output. The majority of these processes have as their primary aim to increase part quality and performance, rather than process improvement.

Subtractive and transformative manufacturing technologies such as machining, remelting, peening, rolling and friction stir processing are examples of secondary processes and energy sources. As the interest for hybrid AM rises, new economic and sustainability tools as well as sensing technologies that facilitate hybrid processing are required. Hybrid AM has heralded the next evolutionary phase in AM and has the ability to radically transform the way products are obtained [23].

Following a review of multiple concepts by various authors, hybrid manufacturing was divided into two major categories, represented on Figure 2.14.

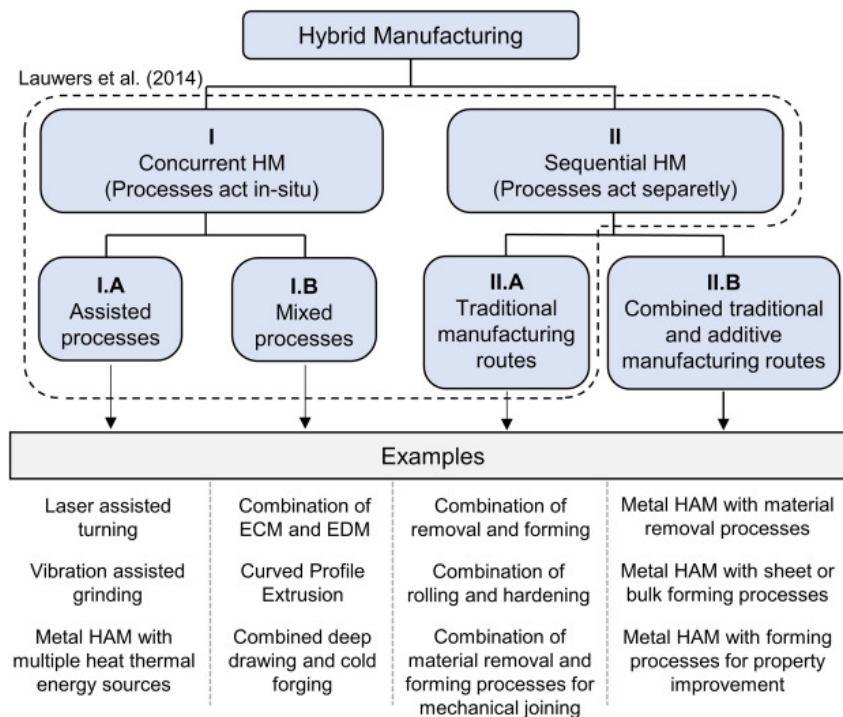


Figure 2.14 Classification of hybrid manufacturing processes [10].

Metal hybrid AM based on the use of multiple thermal energy sources belongs to the category of assisted processes (I.A), since the thermal energy sources only assist the primary AM process. Eventually, the principle of using multiple thermal energy sources was employed in MAM to provide additional energy and improve process stability. MAM hybridization with subtractive processes can be classified into two categories [10]:

- Use of material removal processes at the post-processing level to achieve the geometry precision, dimensional tolerances and surface quality needed.

- Combining material removal processes as part of a manufacturing sequence to obtain parts that would be nearly impossible and very expensive to produce individually either by AM or by subtractive manufacturing.

The second group allows for the production of a wide range of complex parts with intricate features. From this standpoint, the integration of MAM with material removal processes began by combining a previous type of LDED system consisting of a laser with a coupled powder feeding system and a high-speed milling machine to perform material removal operations at intermediate stages of metal deposition.

The first hybrid additive manufacturing systems was developed and commercialized by DMG Mori. The LASERTEC 65 3D Hybrid system from DMG Mori incorporates LDED material deposition with a complete 5-axis milling unit. In reality, due to its greater versatility for incorporating additive and subtractive processes into a single unit, DED is being used in the majority commercial hybrid additive manufacturing systems.

The Lumex Avance-25 by Matsuura was the first hybrid additive manufacturing device based on PBF technology in 2020. The method, which combines LPBF material deposition with high-speed milling, is gaining attraction due to its ability to enhance exterior contours, surface roughness and corrosion characteristics in dies and molds [10].

Figure 2.15 shows two different applications of hybrid AM, produced by DMG Mori.



Figure 2.15 Hybrid AM components: valve body (left) and injection mold (right) produced by DMG Mori [24].

2.1.11 Applications

Engineers from aerospace, automotive and medical device industries quickly realized that AM technologies could be used to produce a variety of components with functional testing purposes.

Aerospace companies began using AM parts for wind tunnel testing, typically instrumented with arrays of pressure sensors which can be designed into the model [15]. AM techniques are suitable for aerospace components since they have the following characteristics [25]:

- Complex geometry: complex shapes are required for integrated functions;
- Difficult-to-machine materials and high buy-to-fly ratio: advanced and expensive materials, such as titanium alloys, nickel-based superalloys and high-strength steel alloys are difficult to manufacture and produce a lot of waste, which AM reduces from 95% to 10-20%;
- Customised production: for small batches, AM is more cost effective than traditional methods, since it does not require expensive tools such as molds or dies;
- On demand manufacturing: AM is capable of producing parts on demand, which significantly reduces maintenance time;
- High performance to weight ratio: components must be lightweight and have high strength and stiffness to weight ratios, in order to minimize costs and emissions.

According to AMPOWER's 2020 report, the industry of aerospace, turbine and helicopters has the highest revenue in system sales in 2019, accounting for 29% of the overall AM sector, as observed in Figure 2.16, and being one of the most promising fields in the future.

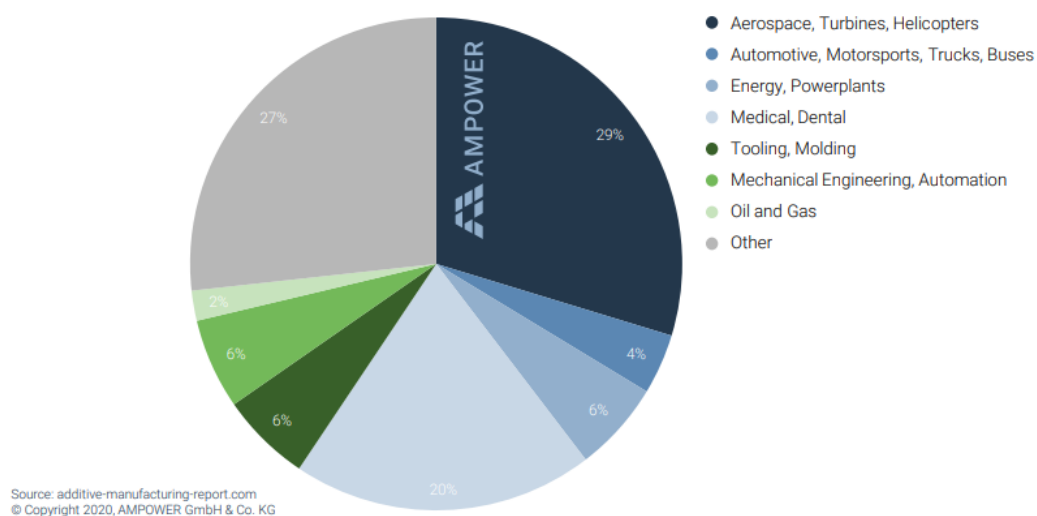


Figure 2.16 System sales revenue by industry 2019 [26].

Examples of components used in aerospace industry produced by MAM are presented in Figures 2.17 and 2.18.

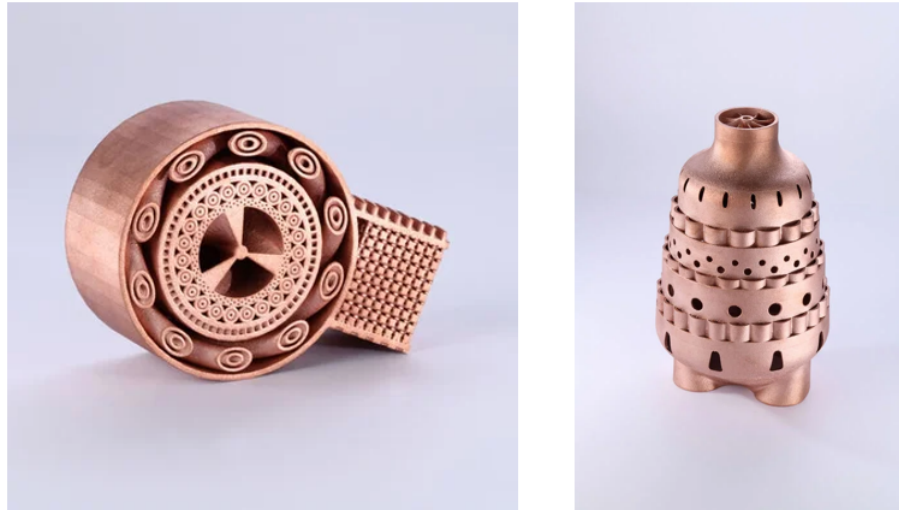


Figure 2.17 Copper Heatexchanger Demopart (left) and Copper Combustion Chamber (right) produced by DMLS [27].



Figure 2.18 ArianeGroup's engine component for Ariane 6 (left) and Satellite bracket from RUAG (right) [27].

In the medical and dental industry, device suppliers were able to nearly double the revenue produced when compared to the previous year. The forecast promises annual sales revenues to increase by 19% by 2024 [26]. Biomedical systems have unique requirements, namely [25]:

- High complexity: new biomedical implants, engineered tissues, organs and managed drug delivery systems can be produced;
- Customization and patient-specific necessities: patient-specific biomedical devices, such as hearing aids and biomedical implants, as well as customized orthotics and prostheses have a lot of potential in AM;

- Small production quantities;
- Easy public access: AM CAD files can be easily shared among researchers so that the same design can be replicated.

Figures 2.19 and 2.20 represent examples of MAM applications on medical and dental industries.

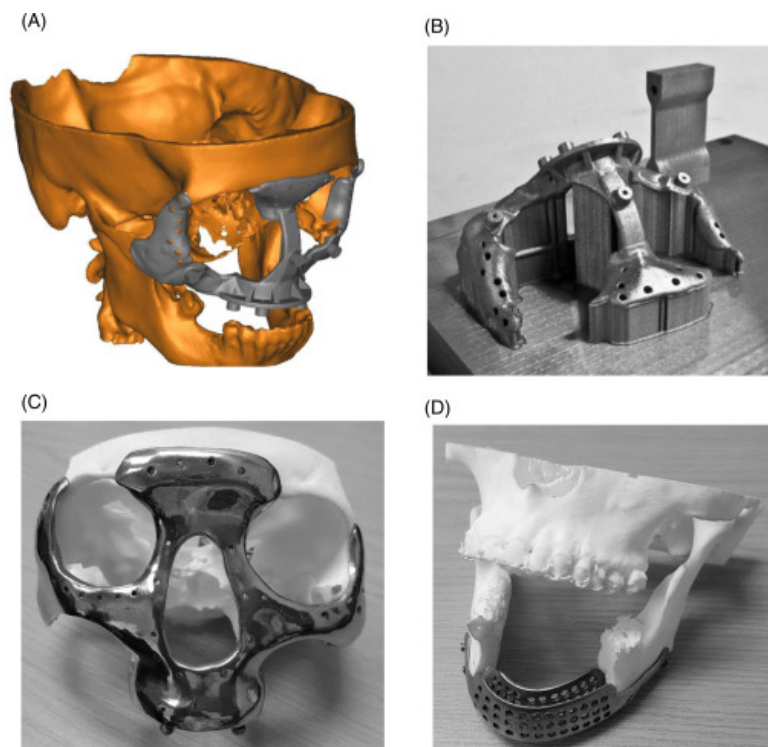


Figure 2.19 SLM Ti based frontal skull implant (C) and mandibular implant (D). Courtesy of the Centre for Rapid Prototyping and Manufacturing, Central University of Technology, Free State, South Africa [28].



Figure 2.20 Orthopaedic Knee Implant by SLM Solutions [29].

Conformal Cooling Channels

For parts that require a high production volume, moulding technologies are remarkably successful. However, cooling the molds after each injection will result in a significant time loss, which can be optimized by using cooling inserts and conformal cooling techniques.

Cooling can be the most time-consuming step of injection moulding operations in some situations and, if performed poorly, can also result in several defects on the injected components. The use of inserts with cooling channels can result in better cooling performance, being the main reason why, over the last decade, the development of conformal cooling strategies has become an industry trend.

This technology consists on the implementation of channels that physically suit the contours of the component to be injected, as represented in Figure 2.21, avoiding the need for cooling channels to be machined or deep drilled, as well as reducing complexity and the risk of uneven cooling pipe interconnection. Additionally, the use of these channels has been shown to improve injection effects like warping and sink marks. In terms of the specific industrial results, in general, total cycle time reductions range between 15% to 60%, depending on component complexity [30].

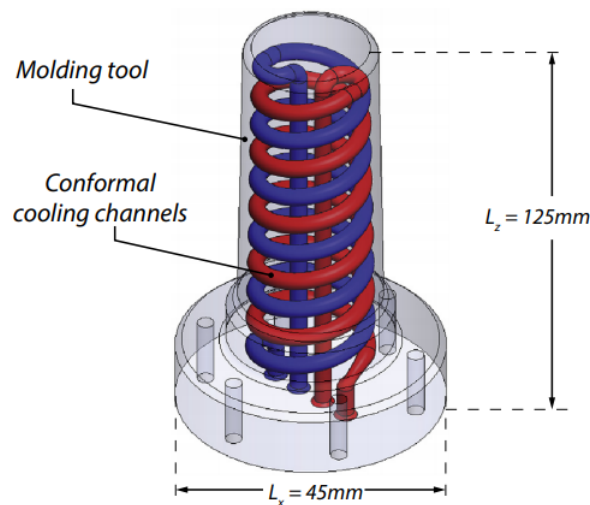


Figure 2.21 PBF cooling die designed with conformal cooling channels to optimize heat transfer rate [31].

Some researches concerning the design of cooling channels focus on the optimal piping layout for particular applications. Cycle times can be reduced by locating the best gates and temperature distribution of cooling channels, which led several authors to improve the procedures by developing algorithms that allowed the device to be validated and dimensioned automatically.

For some AM technologies, such as SLM, the inside channels are expected to have a rough finish since surface finish on interior faces is difficult to achieve. Nevertheless, the interior rugosity can help improving turbulence in the coolant flow, which is a good

attribute for the setting of cooling channels. Aside from that, exterior surfaces can be easily finished and heat treated, resulting in a smooth surface and strong mechanical properties. Consequently, AM not only provides an innovative way to obtain cooling channels, but also unleashes a design revolution for the mold industry's cooling necessities.

In certain industries, such as stock parts manufacturing, switching to AM has been shown to have major effects depending on several variables, namely, moderate production volumes, high number of different orders and relatively high product cost per unit, with one of the most relevant implications being that it can alter business models [30].

Figure 2.22 represent results from a SLM Solutions' study that consisted on the design of six different channel profiles for a tooling insert, including one that resembled a component with conventional cooling to provide a contrast to traditional manufacturing. The channels were optimized by considering factors such as angles of surfaces facing down to minimize the need for supports, minimum wall thickness between channels, dimensions and shapes. Before constructing the various cooling profiles, simulations of water flow and thermal conductivity were performed, revealing that the parts had different cooling behaviour [32]. Another example of this technology's applications is shown on figure 2.23.



Figure 2.22 Tooling insert equipped with conformal cooling channels [32].



Figure 2.23 Die-casting mold insert with conformal cooling channels by SLM Solutions [33].

2.2 Finite Element Method

2.2.1 Introduction

The Finite Element Method (FEM) is a numerical solution approach for the equations that define problems found in nature, whose behavior can generally be explained using differential or integral equations. In addition, the FEM enables users to obtain the evolution of one or more variables describing the behavior of a physical system in space and time. This method is a valuable tool for computing the displacements, stresses and strains in a structure under a series of loads, when it comes to structural analysis.

Analytical and numerical methods differ in that analytical approaches search for universal mathematical expressions that describe the general and "exact" solution to a problem governed by mathematical equations, while numerical methods attempt to provide a numerical solution to the governing mathematical equations. Most numerical methods work by converting mathematical expressions into a collection of algebraic equations that are dependent on a finite set of parameters.

A finite element is a small piece of a larger continuum and the term "finite" distinguishes this part from differential calculus' "infinitesimal" components. The assembly of a set of non-overlapping domains with simple geometry known as finite elements is thought to be responsible for the continuum's geometry: in two dimensions, triangles and quadrilaterals are generally used, while in three dimensions, tetrahedra and hexahedra are commonly used.

A mesh is the way the elements are mapped to the geometry of the problem. Meshes can be finer or coarser, which affects the accuracy and convergence of the solution to the problem. Within each element, a polynomial expansion is used to express the space variance of the problem parameters, such as the displacements in a structure. The FEM only offers an approximation to the exact solution since the "exact" empirical variance of such parameters is more elaborated and usually unknown [34].

The initial equation that defines the problem is transformed into its weak form using the variational principle: a broader mathematical statement that reduces the order of the partial differential equation by multiplying it by a test function and integrating it over the domain, converting a differential formulation into an integral formulation. The shape functions that interpolate the set of nodal variables that determine the problem's unknowns replace the test functions. Shape functions are mathematical expressions that map nodal values into the problem's domain. They can be defined for the entire geometry, as in Rayleigh-Ritz or Galerkin's methods, or for each individual part, as in FEM [35].

Shape functions must attain two mathematical requirements:

- i. must be defined unitary at their respective node and zero at all other nodes;
- ii. the summation of all shape functions must equal the unit at any point in the domain.

Equations 2.1 and 2.2 mathematically describe these two conditions, respectively, where ψ is a shape function, j is the node at which the shape function is defined to be unitary, i is a generic node, N_n is the total number of nodes and Ω_e is the domain of the shape function. ϵ , η and ζ are local coordinates [35].

$$\psi_j(\epsilon_i, \eta_i, \zeta_i) = \begin{cases} 1, & \text{if } i = j \\ 0, & \text{if } i \neq j \end{cases} \quad (2.1)$$

$$\sum_{j=1}^{N_n} \psi_j(\epsilon_i, \eta_i, \zeta_i) = 1, \forall i \in \Omega_e \quad (2.2)$$

2.2.2 FEM within AM

The application of finite element modeling to predict distortion and residual stress in AM arises from previous research on multi-pass welding. This process is a similar to AM in that it requires a heat source to melt material onto a workpiece, which then cools and solidifies. In this technique, thermal gradients cause unwanted distortion and residual stresses, however, using FEM to simulate the AM process creates additional problems: the addition of material during the deposition and the increase in the number of passes and processing time lead up to higher complexity and computational cost [36].

Due to its ability to handle nonlinear problems, finite element analysis (FEA) is widely regarded as the preferred numerical approach. Several commercial finite element-based software packages have recently released AM modules or built-in functionalities capable of simulating various approaches to thermo-mechanical analysis to predict printed part microstructure, stresses and distortions via [37]:

- i. detailed Goldak or Gauss-type heat source definition with micro-scale resolution;
- ii. adaptive meshing approaches in the heat source proximity;
- iii. multi-scale modelling with micro-scale results imported at lower mesh resolution for 3D complex geometries;
- iv. super-layer or block-dump approaches for material deposition with singular moving point nodal surface heat flux representation.

By increasing simulation simplification, computational running times for AM processes with complex engineering components can be reduced to times comparable to the actual printing process. Many research groups are comparing the computational efficiency and accuracy of these simpler methods to results obtained with finer mesh resolution, which is still an on-going area of research. As a result, it is unknown how much simulation simplifications affect residual stress and distortion effects [37].

The various formulations of the AM physical and mathematical model, as well as fundamental equations and FEM implementation in commercial software packages, are discussed in the following sections.

2.2.2.1 Thermo-mechanical simulation

Thermal-mechanical analysis allows for precise specification of processing conditions in time and space, as well as, control over the solution's accuracy. Although this approach is generally more reliable than pure mechanical eigenstrain analysis, it is also computationally more expensive [38].

Nonlinear thermo-mechanical analysis is used in all modeling procedures for AM processes in the literature. This process can be divided into two categories:

- i. performing a pure thermal or heat transfer analysis in order to determine the nodal temperature in the FE based model;
- ii. establishing a structural configuration in order to determine the FE based model's mechanical response under applied nodal temperature gradients and, ultimately, achieve the distortion and residual stresses of the manufactured part.

When the thermal analysis is followed by a structural assessment for each increment, the method is known as fully coupled thermo-mechanical, however, if the mechanical analysis is performed after the thermal assessment is concluded, the method is called decoupled or weakly coupled. The former are characterized by a structural evaluation after each phase of the thermal analysis step, which means that the geometry is modified at each time stage and its displacements affect the workpiece's temperature field. The latter is characterized by a complete thermal simulation performed prior to any structural analysis, implying that the thermal field is unaffected by the component's mechanical response. Due to its lower computational intensity and suitable performance, weakly coupled thermo-mechanical simulation is the most commonly used approach in commercial simulation packages [39, 40].

The heat transfer analysis is based on the body's energy conservation principle and it is expressed in Equation 2.3:

$$Q(\mathbf{X}, t) - \rho C_p \frac{dT}{dt} + \nabla \cdot [k(T) \nabla T] = 0 \quad (2.3)$$

in which \mathbf{X} represents spatial coordinates, t represents time, Q represents body heat source, ρ is material density, C_p represents specific heat of material, k represents conductivity and T is temperature. The temperature history of nodes is obtained by numerically solving this equation for the given geometry and boundary conditions and the nodal temperatures are then added to the structural analysis as a thermal load [39]. The thermal boundary

conditions, including conduction, convection and radiation, are contained in the body heat source [41].

The laser characteristics such as strength, speed, direction, form and performance must be included in the thermal source model. Yan et al [39] experimented with three types of thermal body heat flux distributions: 3D super-Gaussian, 3D Gaussian and 3D inverse-Gaussian beams. According to the authors, the super-Gaussian beam shape with higher laser power as well as the Gaussian and inverse-Gaussian beam shapes with lower laser power may reduce residual stress in the laser traverse direction. In AM modeling studies, the incoming body heat energy has been widely provided by Goldak's model:

$$Q = \frac{6\sqrt{3}\eta Pf}{\pi\sqrt{\pi abc}} \exp\left(-3\frac{x^2}{a^2} - 3\frac{y^2}{b^2} - \frac{z^2}{c^2}\right) \quad (2.4)$$

where P is the laser power, η is the absorption efficiency, f is a weighting fraction and a , b and c are the ellipsoid's longitudinal, transverse and pool depth measurements, respectively, as represented in Figure 2.24 [41].

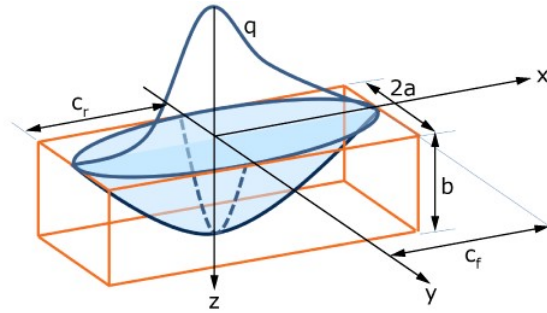


Figure 2.24 The Goldak expression for energy distribution from a laser source [42].

The Stefan-Boltzmann law is used to calculate the thermal radiation q_{rad} :

$$q_{\text{rad}} = \zeta \sigma_b (T_S^4 - T_{\text{env}}^4) \quad (2.5)$$

where ζ is the surface emissivity, σ_b is the Stefan-Boltzmann constant, T_S is the surface temperature and T_{env} is the environment temperature. The convective heat loss is represented in Equation 2.6:

$$q_{\text{conv}} = h(T_S - T_{\text{env}}) \quad (2.6)$$

where h is the convective heat transfer coefficient [41].

Mechanical modeling is based on the equilibrium mechanics of a continuum body and incorporates a constitutive model for the elastic behaviour using Hook's law and plastic behavior through the isotropic or kinematic hardening rules of the built material:

$$\nabla \cdot \sigma = 0 \quad (2.7)$$

$$\sigma = C(\epsilon - \epsilon^p - \epsilon^T) \quad (2.8)$$

where σ is the Cauchy stress, C is the fourth-order elastic stiffness matrix and ϵ , ϵ^p and ϵ^T are, respectively, the total, plastic and thermal strain tensors. The residual stresses and distortions are computed by applying boundary conditions to the mechanical FE model. In order to represent a more realistic simulation of the process, material properties should be considered temperature dependent in both thermal and mechanical analyses [39].

2.2.2.2 Inherent strain

Aside from the adaptive mesh-based approaches that have recently been established, some researchers have used the concept of inherent strain. Ueda et al [43] developed the inherent strain method for quick computation of distortion of welded structures, which is based on the fact that plastic strain causes incompatibility in the welded structure and leads to component distortion. In order to allow residual stress computation using the plastic strain vector within FEM, Equations 2.9 to 2.13 were proposed by Ueda (1989) [43].

$$\mathbf{f} = \int_V \mathbf{B}^T \mathbf{D} \epsilon_{inh} dV \quad (2.9)$$

$$\mathbf{u} = \mathbf{K}^{-1} \mathbf{f} \quad (2.10)$$

$$\epsilon_{tot} = \mathbf{B} \mathbf{u} \quad (2.11)$$

$$\epsilon_e = \epsilon_{tot} - \epsilon_{inh} \quad (2.12)$$

$$\sigma = \mathbf{D} \epsilon_e \quad (2.13)$$

in which \mathbf{f} is the nodal force vector, \mathbf{B} is the deformation matrix, \mathbf{D} is the constitutive matrix, \mathbf{u} is the displacement vector, \mathbf{K} is the stiffness matrix, σ is the nodal stress vector and ϵ_{tot} , ϵ_{inh} and ϵ_e are, respectively, the total, inherent and elastic strain.

The strain scaling factor, which aims to be more suited to a machine's settings through a factor called Strain Scaling Factor (SSF), is the second method of implementing an inherent strain analysis. This is the easiest and fastest simulation by assuming a predefined isotropic plastic strain field in each voxel element [44].

$$\varepsilon_{inh} = SSF \cdot \frac{\sigma_{ys}}{E} \quad (2.14)$$

Keller and Ploshikhin were the first to use the inherent strain principle to determine the distortion of AM parts. By discretizing the model into three separate scales (micro, meso and macro), the authors introduced the concept of mechanical layer equivalent. With a real thermal heat source model and thermal boundary conditions, a pure thermal analysis is performed on a very small geometry that is attached to a substrate which reflects the lower layers in real size. The thermal history of the nodes is described as a small cubic heat source as a result of the micro-scale model. The small cubic heat source is then implemented in the meso-scale fully coupled thermo-mechanical model, with various laser trajectories taken into account (hatching strategies). As a result, the model's plastic strain components are removed and, following that, orthotropic thermal expansions based on plastic strain components are measured and placed on the thermo-elastic macro-scale model, with the temperature of the entire layer increased to unity. Consequently, it is possible to determine the distortion of the macro-scale model that represents the real component. According to the authors, the experimental data and the findings obtained from the inherent strain application to estimate the distortion of an intricate component had a very strong agreement [40].

The previously mentioned method assumes that the distribution of plastic strain is roughly the same for different areas of geometry, however, it varies with volume shape and complexity [40]. The main disadvantage of this approach is that it cannot take into account the effect of different laser scanning paths and geometrical effects since the inherent strain is constant across the whole volume. Despite the inherent strain method's high potential in evaluating the residual stresses and distortions of a specific geometry in AM processes, Bugattin and Semeraro observed that the calibration strategy fails to predict the distortion and, as a result, the residual stress of different geometries [45]. As a result, this approach should be revised in order to better represent the characteristics and functionality of AM processes.

The inherent strain method is used to model the LPBF process but it can also be used to model the DED and DMD processes by adjusting the discretization steps. Liang et al adjusted the inherent strain method concept and applied it to the DED of a 5 to 10 layer thin-walled rectangular. The results of the experimental and modified inherent strain methods concurred very well and the authors reported a 14 and 11 times reduction in computational time when modeling a 10 layer and 5 layer rectangular build, respec-

tively, when compared to conventional thermo-mechanical analysis. This demonstrates the inherent strain method's high capability for larger components [39].

2.2.2.3 Activation methods

The incremental addition of material onto the substrate requires the use of numerical analysis techniques. The most well-known approaches are [39]:

- i. quiet elements activation;
- ii. inactive elements activation;
- iii. hybrid elements activation.

The quiet element activation approach states that the part's final geometry is already present in the model prior to simulation, nonetheless, the material properties of those non-deposited elements are scaled down to the point that they have no significant impact on the analysis results. As the thermal heat source passes over the quiet elements, they are activated and their material properties are updated with real material properties [39]. Additionally, this technique can be easily implemented in many commercial FE packages due to the fact that it requires no additional equation renumbering or solver initialization [40].

In the inactive element activation method, on the other hand, only deposited elements are present in the model and non-deposited elements are added to the model with each increment as the heat source moves. In comparison with the previous method, scaling down the material properties for non-deposited elements causes the stiffness matrix to become ill-conditioned. Consequently, there is a large number of inactive elements at the start of the process, which significantly increases the number of model equations to be solved. However, the stiffness matrix in the inactive element activation method is much smaller and well defined and the renumbering process requires significant computational effort for the FE model.

The hybrid activation method, in which non-deposited layers are removed from the model, was developed to model depositing new elements or layers by combining both previous activation methods. The model only contains the depositing layer and non-deposited elements are scaled down using the quiet element approach. As the next layer is applied to the model, the nodes or elements are renumbered using the inactive element activation process and non-deposited elements become quiet. The major benefit of this activation technique is the fact that it allows for the generation of a both a smaller and less ill-conditioned stiffness matrix, thus, reducing computational effort [39].

Progressive element activation via quiet element or inactive element was developed by Michaleris, who used inactive elements to speed up computational time on initial layers and quiet elements to effectively model material deposition. This technique only uses quiet elements and inactive components would be omitted from the model, which would

drastically reduce computing time [46]. The thermal conductivity, k , is set to a lower value in heat transfer analyses to reduce conduction into quiet elements and the specific heat, C_p , is set to a lower value to regulate energy transfer to quiet elements [47]:

$$k_{quiet} = s_k k \quad (2.15)$$

$$C_{p_{quiet}} = s_{C_p} C_p \quad (2.16)$$

where, k_{quiet} and $C_{p_{quiet}}$ are the thermal conductivity and specific heat used for quiet elements and s_k and s_{C_p} are, respectively, the scaling factors used for the thermal conductivity and specific heat.

The simulation specifies which elements will be activated by initially determine the location of the beam within the current layer and, then, activating all elements that are within the build domain but behind the current beam position along the build path. Figure 2.25 illustrates this method, as the green references represent active elements and the gray references represent the elements that have been quieted. Afterwards, a search for any build elements below the current layer plane is carried out and all identified elements are allowed before the simulation for that increment is performed [46].

As the metal is deposited during production, the interface is constantly changing, which results in the need to create algorithms that calculate the position of the evolving interface and apply surface convection and radiation as required. Consequently, it is difficult to compute the interface between active and inactive (or quiet) elements using user subroutines in general purpose FEA codes, reasoning why it is usual to overlook surface convection and radiation at this interface. This simplification can be sufficient in weld modeling, however, in AM the size of the deposited material compared to the substrate can be significant. Thus, ignoring surface convection and radiation on the interface between active and inactive elements can be a source of error [47].

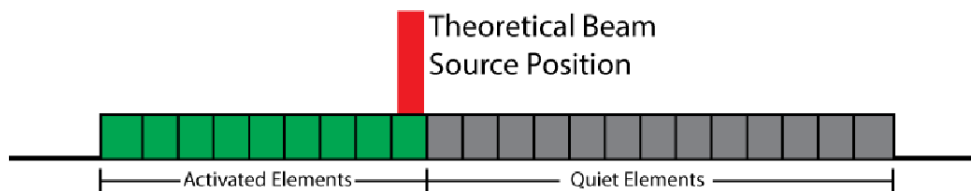


Figure 2.25 Schematic showing the subroutine model deposition of material [46]

2.2.3 Commercial software packages

Metal deposition has reportedly been modelled using a number of general-purpose commercial codes: Ansys, Adina, Abaqus, Comsol and Marc. Nevertheless, these references do not have into account the numerical method used during element activation nor possible sources of errors or numerical performance. Since the size of the deposited material in AM is much larger, element activation errors can be severe [47]. Some commercial FE packages based on the inherent strain method have also been developed, such as, Simufact, Amphyon, GeonX and ESI [40].

These softwares are in different stages of development and provide a variety of features, however, they are mainly based on MAM distortion simulations [15]. The modelling of PBF and DED processes must overcome numerous challenges: progressive material addition, moving heat source input and thermal losses during building.

In this thesis, the software package used to conduct the proposed simulations was Abaqus, due to its special AM plug-in. The plug-in contains predefined tables and modules that allow detailed and efficient modeling. Abaqus not only implements a solution for the previous mentioned issues, but it is also developed in a user subroutine layout and keywords interface that offers lot of flexibility and customization.

In the following sections, several features of Abaqus' AM simulations will be described.

2.2.3.1 Thermo-mechanical simulation

A sequential thermal-stress analysis of an AM process begins with a transient heat transfer analysis of thermal loads introduced by the process on a printing component, which is followed by a static structural analysis guided by the temperature field from the thermal analysis. Support structures, if required, and the substrate on which the component and supports are installed should also be included in the study to account for their effects on thermal conduction, part distortions and residual stresses. The stress analysis is driven by the temperatures from the heat transfer analysis. Furthermore, for accurate stress performance, similar progressive material deposition techniques as the heat transfer analysis and temperature-dependent material properties can be used [48].

Progressive element activation

Progressive element activation is used to model the layer-by-layer deposition of raw material from a roller and the melting process. By assigning a volume fraction of material at the beginning of the increment, the elements with the activation function on can be triggered. There are two types of activation: full and partial [49]. The material volume fraction added for full activation must be 0 or 1, which means that an element's status can only change from inactive to fully activated. On the other hand, the material volume fraction added for partial activation may be any value. In stress-displacement analyses, the material added to an element is presumed to be stress-free.

The elements become active when a toolpath intersects them. The toolpath-mesh intersection module in Abaqus calculates the geometric intersection of multiple toolpaths and the finite element mesh of the component to be manufactured. A toolpath is characterized by a geometric form that moves along a path and is attached to a reference point. Connecting a set of points in space and time defines the direction and an event series defines the collection of points. For toolpath-mesh intersection, three shapes are considered:

- i. a point;
- ii. an infinite line;
- iii. a box.

Depending on the application, these shapes enable different levels of abstraction to characterize the tool's shape. A scan pattern that describes the idealized motion of a tool rather than the actual course of the motion can be used in addition to these three shapes. The schematics and machine tool examples of the shapes are presented in Figure 2.26 [50].


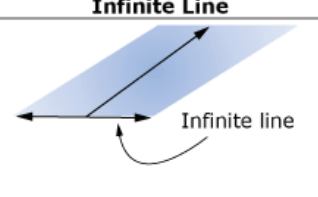
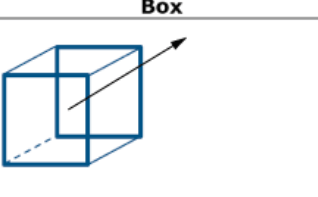
Shape	Point	Infinite Line	Box
Schematic			
Machine tool examples	Point lasers for coarse meshes	Recoater in powder-bed fabrication	Material deposition nozzle in polymer extrusion, wire-feed, laser blob for fine meshes, etc.

Figure 2.26 Point, infinite line and box toolpaths [50].

Moving heat source

The newly deposited layer of material is heated to melting point, allowing it to combine with the solid material underneath it. The modeling of the heat source is needed for this reason. The challenges are capturing the size and shape of the energy flow accurately, as well as estimating the amount of heat absorbed by the printed component.

When the tool's action zone is small compared to the mesh size and can be idealized as a point, such as when the laser beam radius is small compared to the element size, the point toolpath, shown in Figure 2.27, is advantageous. This model calculates the number of toolpath intersections, the coordinates of the start and end points, ξ_s and ξ_e , in the entity reference coordinate system, as well as the start and end times, t_s and t_e , for each intersection for a given element.

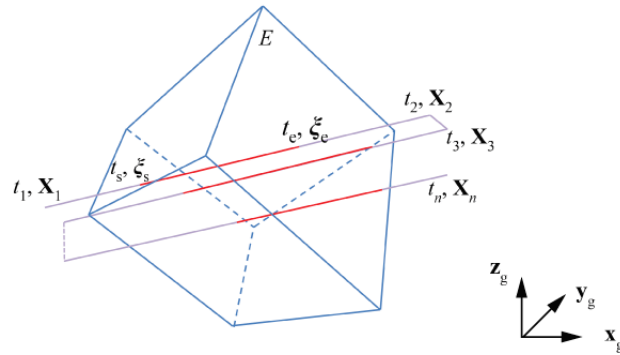


Figure 2.27 Point toolpath-mesh intersection [50].

The infinite line representation can be used, for example, to describe the layer-by-layer material deposition procedure, such as the activation of the roller in PBF. The intersections of an infinite line toolpath with a finite element, E , are shown in Figure 2.28. An infinite line attached to a reference point moves along the path connecting points $(\mathbf{X}_1, \mathbf{X}_2, \dots, \mathbf{X}_n)$, such that the reference point is at \mathbf{X}_i at time t_i , is what defines the toolpath. The infinite line remains perpendicular to the section and the tool moves at a constant velocity over a segment, connecting two successive points in the direction.

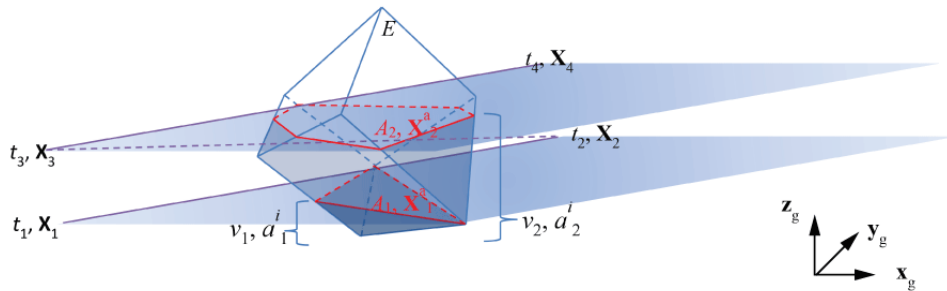


Figure 2.28 Infinite line toolpath-mesh intersection [50].

The first field in the event sequence reflects the tool's state, such as the "on/off" state of a recoater roller. Over the segment connecting \mathbf{X}_n and \mathbf{X}_{n+1} , the field specified for a point \mathbf{X}_n remains constant. The toolpath-mesh intersection module calculates the number of intersections, m , and the volume fraction, v_f , for each intersection for a given element. The module also determines the area, A , the coordinate regarding the element reference coordinate system of the center of intersection of the z plane and the element, \mathbf{X}^a , and the area fractions below the z plane for all sides for each intersection, \mathbf{a}_f^i .

When the tool's action is better represented as a spatially varying distribution, the box shape functionality is intended, for example, modeling a Goldak's double ellipsoid heat source. The sub-segment approach and the sub-element approach are two related algorithms or methods for computing intersections of a box toolpath and a mesh.

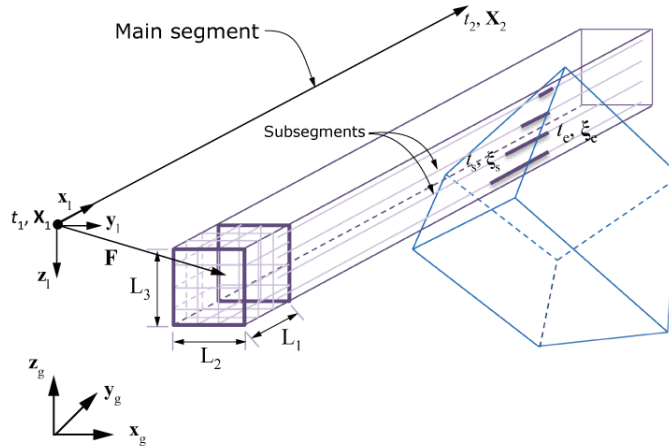


Figure 2.29 Box toolpath-mesh intersection using the sub-segment approach [50].

The toolpath represented in Figure 2.29 is defined by a box attached to a reference point that is moving along the path connecting points $(\mathbf{X}_1, \mathbf{X}_2, \dots, \mathbf{X}_n)$, such that the reference point is at \mathbf{X}_i at time t_i . The box lengths L_1 , L_2 and L_3 are oriented in the local coordinate system's directions. The box is divided into a user-defined number of smaller boxes, with each smaller box's sub-segment beginning at the center and running parallel to the main segment. This formulation calculates the number of toolpath intersections, the coordinates of the start and end points related to the element reference coordinate system, ξ_s and ξ_e , and the start and end times, t_s and t_e , for each intersection [50].

Thermal losses

To ensure that temperature gradients are correctly measured, it is critical to accurately model thermal conduction, free convection and thermal radiation. During the AM process, previously exposed material surfaces are replaced with new material and new free surfaces are produced over time. Abaqus keeps track of the changing free surfaces that represent the current shape of a printing component at any given point in the build and only applies film and radiation loadings to those surfaces.

In both convection and radiation mechanisms, a room temperature must be applied and experimental analysis is widely used to extract the film coefficient and the material surface emissivity [48].

2.2.3.2 Eigenstrain-based simulation

An AM process eigenstrain analysis (also referred to as inherent strain, assumed strain or "stress-free" strain) consists of a single static stress analysis of a printing component with a predefined field of eigenstrains added to each portion upon activation, reflecting the inelastic deformation induced by the process. The major cause of residual stresses and overall part distortion is inelastic deformations, therefore, the aim of an eigenstrain

analysis is to predict distortions and residual stresses in the part. When eigenstrains are added to a newly deposited sheet, they can cause residual stresses and distortion in the layers below.

In Abaqus, eigenstrains can be assigned to a new material that is attached to an element. Furthermore, when a solid element is first activated, the local orientation can be changed. A sudden application of eigenstrains, including thermal strains, may cause convergence issues. As a result, Abaqus allows the eigenstrains to be linearly ramped up using the formula:

$$\epsilon^{eig} = \begin{cases} \frac{t-t_{act}}{\tau_{eig}} \epsilon_0^{eig}, & t_{act} \leq t \leq t_{act} + \tau_{eig} \\ \epsilon_0^{eig}, & t > t_{act} + \tau_{eig} \end{cases} \quad (2.17)$$

where ϵ^{eig} is the applied eigenstrain, ϵ_0^{eig} is the value of the eigenstrain at the beginning of the increment at which the element is activated, t_{act} is the activation time and τ_{eig} is a user-specified time constant, which default value is zero.

The location of the nodes shared by active and inactive elements in general will shift in a static analysis until the elements are activated. The configuration at the time of element activation differs from the initial element configuration in this situation. The stress in the element is determined by the deformation caused by this new configuration, which is presumed to be stress-free [51].

Trajectory-based eigenstrain analysis

An eigenstrain analysis based on a given trajectory of new material being fused or bonded to the underlying layer activates elements and applies eigenstrains. The trajectory of a PBF process, for example, is the same as the heat source scan path and the nozzle path is the trajectory of guided energy deposition and material extrusion processes. The toolpath-mesh intersection module processes the trajectory immediately after it is described using an event sequence. The material orientation can be changed to comply with the trajectory if desired. The analysis is similar to the stress analysis used in thermo-mechanical simulations, except it is motivated by eigenstrain loadings rather than temperature results [51].

Pattern-based eigenstrain analysis

Pattern-based eigenstrain analysis activates elements layer-by-layer, applying eigenstrain to each layer based on a given in-plane eigenstrain pattern. A domain is divided into eigenstrain patterns by a "quilt" of one or more patches. Each patch is a region with a specific eigenstrain value or eigenstrain rotation angle as a result of a specific trajectory in that region. The eigenstrain patterns for PBF processes, for example, are related to the heat source's in-plane scan pattern, while the eigenstrain patterns for guided energy

deposition and material extrusion processes are related to the nozzle's in-plane moving pattern.

The definition of a trajectory is not needed for a pattern-based eigenstrain analysis. The study only considers layer-by-layer construction sequences, ignoring extensive material deposition or scanning sequences within layers. Elements are activated layer-by-layer in the user subroutine and the toolpath-mesh intersection utilities are used to determine which eigenstrain patch an element in the last activated layer belongs to, and then the eigenstrains are applied to the element. The material orientation can also be changed, for example, to correlate with the rotation angle of the patch's eigenstrain [51].

Scan pattern–mesh intersection

A scan pattern represents the movements of a tool as it moves or scans regions of a cutting plane or slice. The scan pattern is made up of a rectangular unit cell that is repeated until the cutting plane is covered. The rectangular unit cell is made up of several smaller rectangular patches, each of which can describe a local angle, φ , between the tool's scanning motion and the I -axis, as represented in Figure 2.30. Each of the pattern patches can be assigned an eigenstrain tensor, which represents the inelastic deformation caused by the operation.

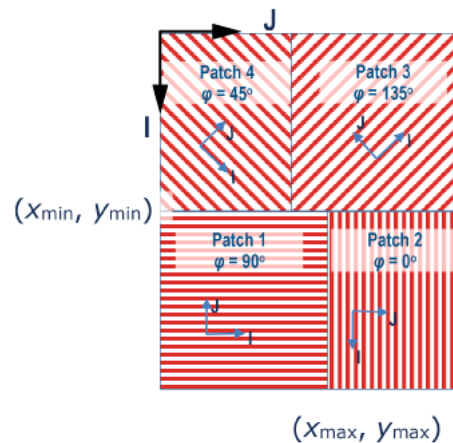


Figure 2.30 A scan pattern with four patches with local orientations rotated by 90° , 0° , 135° and 45° [50].

The toolpath-mesh intersection module calculates the number of slices, m , within an element for a given increment for a given element (see Figure 2.31). It determines which pattern patch contains the center of each slice in that element, as well as the patch's local orientation, based on the layer to layer rotation, θ and the local rotation of the scanning direction in that patch, φ . The partial volumes of the element beneath each slice, v_f are also computed by the module [50].

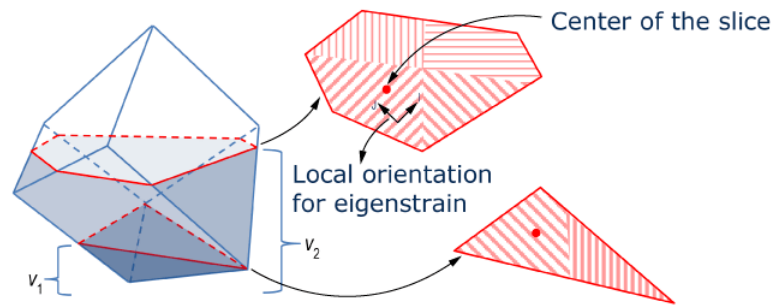


Figure 2.31 Scan pattern overlaid on an element [50].

This page was intentionally left blank.

Chapter 3

Simulation Details and Methods

In this Chapter, the performed simulations are described and presented, along with their defining parameters and context. While the results will be discussed in Chapter 4 and concluding remarks will be found in Chapter 5, relevant decisions about the simulation's setup are shown in this chapter.

3.1 Introduction

The fundamental purpose of this thesis, as stated in the introductory chapters, is to develop a numerical model of the PBF process using Abaqus and compare the results to the experimental data made available through INEGI's ongoing research projects. Furthermore, a numerical model of the Direct Energy Deposition process was also developed, in order to better understand the difference between the mechanical properties of parts produced by both MAM techniques.

The goal of this chapter is to describe the selected parts and materials, as well as to provide an overview of all simulation parameters and objectives, so that the reader can easily understand the results.

3.1.1 Physical specimens

The numerical simulations were conducted using two different specimens: a quadrangular right prism, which can be found in Figure 3.1, and an AM benchmark piece, represented in Figure 3.2, that will be referred to as a benchmark bridge, which was inspired in the NIST round robin exercise [52].

The prism will be used in both PBF and DED numerical models, while the benchmark bridge will be only considered in the PBF model, since the very thin walls of 0.5 [mm] and the angles of the legs cannot be reproduced by DED because of the larger beam size used in this process.

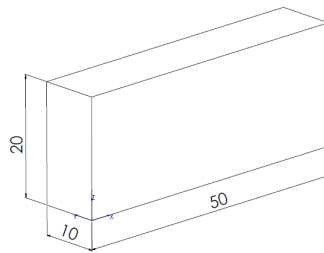


Figure 3.1 Prism dimensions and coordinate system (dimensions in millimetres).

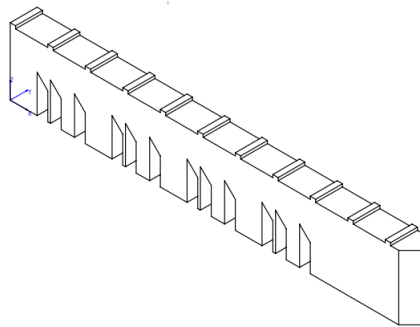


Figure 3.2 Benchmark bridge and coordinate system.

The numerical results of both parts produced by PBF will be compared, in terms of residual stresses, to the experimental results of FCTUC's study. Additionally, the numerical results achieved for the prism in both models (LPBF and DED) will be compared. Although the two processes present different ranges of values for some parameters (including the layer thickness and the scan speed), in this case, the parameters defined for the PBF model were applied to the DED model in order to establish a more direct comparison between the processes.

To avoid adding complexity to the numerical analysis, each part is attached to a substrate, which acts like a heat conduction sink. Additionally, each substrate has the dimensions of 160x60x20 [mm] and is from the same material as the part, however, in the experimental studies the substrates are made of carbon steel. There are not supports connecting the parts to the substrates.

Prism

Despite being a simple geometry, it is ideal to employ in most parametric and convergence simulations. Due to the prism's simple shape, it can be easily and quickly discretized, with both coarser and finer meshes being able to adequately represent it, and it does not require support structures. Additionally, this geometry avoids large thermal boundaries and highlights parametric variables. Since the goal of parametric simulations is to emphasize a variable's influence in the residual stress field, external errors caused by undesirable elements are minimized.

The material used in both numerical and experimental cases is AISI 316L stainless steel. Due to its exceptional corrosion resistance, high specific strength, ductility and fracture toughness, 316L stainless steel is widely used as structural material in industries such as petrochemistry, transportation, ultra-supercritical power and nuclear power plants [53].

The variables presented in Table 3.1 correspond to the machine settings which define the prism's manufacturing process. The scanning strategy used in the experimental study is based on individual stripes with repeating orientation every three layers, implying patterns with a 120° lag between them.

Table 3.1 Machine settings used in the AM process of the prism.

Layer thickness	Laser Power	Scan Speed	Laser Diameter	Hatch Space
0.04 [mm]	400 [W]	860 [mm/s]	0.175 [mm]	0.095 [mm]

Benchmark bridge

The benchmark bridge component is a bridge structure with twelve legs (four repetitions of three legs with varying widths) supporting a bulk volume of $75 \times 5 \times 5$ [mm], with additional minor prominences of $1 \times 5 \times 0.5$ [mm]. The structure has a 2.5 [mm] chamfer at one of its extremities. Figure 3.3 shows the dimensions of the bridge.

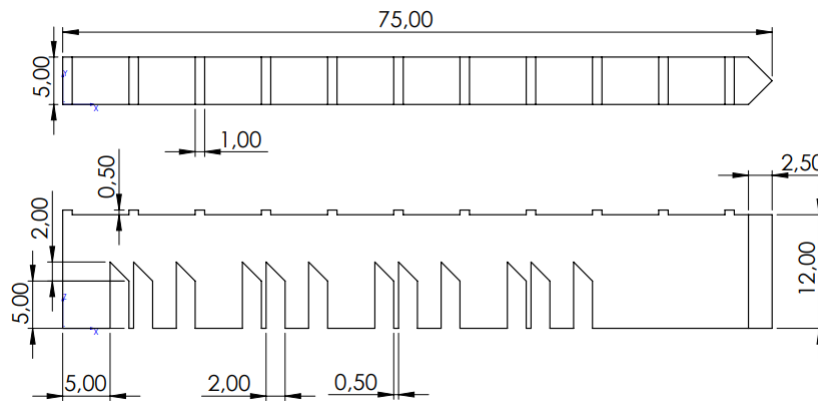


Figure 3.3 Bridge dimensions (in millimetres).

The benchmark bridge's very narrow section areas are one of the main challenges in the printing and simulation processes: the smallest bridge leg is only 0.5 [mm] thick, requiring a reasonably fine mesh to accurately characterize this particular region.

The variables displayed in Table 3.2 correspond to the machine settings which define the bridge's manufacturing process. Two scanning strategies were used in the experimental study, however, for the numerical study only one of them will be considered: a continuous line strategy, where even layers were vertically scanned (90°) and uneven layers were

scanned horizontally (0°). The bridge and substrate are made of 18Ni300 maraging steel in the numerical model.

Table 3.2 Machine settings used in the AM process of the benchmark bridge.

Layer thickness	Laser Power	Scan Speed	Laser Diameter	Hatch Space
0.03 [mm]	200 [W]	950 [mm/s]	0.175 [mm]	0.110 [mm]

3.1.2 Material Definition

316L stainless steel

316L stainless steel is employed in most convergence and parametric simulations and it is a dominant material in the universe of metallic AM. It is similar to ordinary 316 stainless steel, but with reduced carbon and sulphur levels. Lower carbon percentages provide additional resistance to carbide precipitation at grain boundaries, a problem that is exacerbated when the material is heated to temperatures of around 500°C to 800°C . At these temperatures, chromium precipitates in grain boundaries, depleting certain areas that become corrosion prone, a problem that molybdenum is known to prevent [2].

Steel 316L is frequently selected over other austenitic types as a structural material because of its stronger corrosion resistance and better mechanical features at low and high temperatures [54].

Due to their potential to allow fast near net-shape production of complex geometric components without the use of molds, laser additive manufacturing (LAM) of 316L parts, such as laser melting deposition (LMD) and selective laser melting (SLM), has recently attracted a lot of attention. In comparison to SLM, LMD has a higher construction rate, making it more suited to large-scale component production. However, due to epitaxial growth and a slower cooling rate, 316L steel prepared by LMD typically has large columnar grains, resulting in low yield strength and anisotropic mechanical properties, limiting its use in some extreme working situations [55].

The chemical composition of the commercial type 316L austenitic stainless steel employed in this study is presented in Table 3.3.

Table 3.3 Chemical composition, in wt.%, of type 316L austenitic stainless steel [2].

C	Si	Mn	P	S	N	Cr	Mo	Ni	Cu	Co
(%)	(%)	(%)	(%)	(%)	(%)	(%)	(%)	(%)	(%)	(%)
0.018	0.38	1.84	0.035	0.029	0.078	16.6	2.02	10.2	0.36	0.18

Many heat transfer problems involving phase change must account for latent heat effects, which can be significant. It is presumed that latent heat exists in addition to the specific heat effect. The latent heat is thought to be released over a temperature range of

lower (solidus) to higher (liquidus) temperatures [56]. These values are presented in Table 3.4 and the thermo-physical properties of this material are shown in Table 3.5.

Table 3.4 Latent heat properties [3].

Latent heat of fusion [kJ/kg]	Solidus Temperature [K]	Liquidus Temperature [K]
290	1675	1708

Table 3.5 Thermo-physical properties of AISI 316L steel [4].

Temperature [°C]	Specific Heat [kJ/kg/°C]	Conductivity [W/m/°C]	Density [kg/m ³]	Thermal expansion [mm/mm/°C]
20	0.492	14.12	7966	14.56×10^{-6}
100	0.502	15.26		15.39×10^{-6}
200	0.514	16.69		16.21×10^{-6}
300	0.526	18.11		16.86×10^{-6}
400	0.538	19.54		17.37×10^{-6}
500	0.550	20.96		17.78×10^{-6}
600	0.562	22.38		18.12×10^{-6}
700	0.575	23.81		18.43×10^{-6}
800	0.587	25.23		18.72×10^{-6}
900	0.599	26.66		18.99×10^{-6}
1000	0.611	28.08		19.27×10^{-6}
1100	0.623	29.50		19.53×10^{-6}
1200	0.635	30.93		19.79×10^{-6}
1300	0.647	32.35		20.02×10^{-6}
1400	0.589	33.78		20.21×10^{-6}

A Poisson's ratio of 0.294 and a temperature dependent Young's modulus, reported in Table 3.6, were utilized to describe the elastic behavior of AISI 316L steel.

A Johnson–Cook's (J–C) material constitutive equation was used to model the thermo-visco plastic behavior of AISI 316L steel, which may be represented as follows:

$$\sigma_{eq} = (A + B\varepsilon^n)(1 + C \ln(\frac{\dot{\varepsilon}}{\dot{\varepsilon}_0}))(1 - (\frac{T - T_{room}}{T_m - T_{room}})^m) \quad (3.1)$$

where ε is the plastic strain, $\dot{\varepsilon}$ is the strain rate (s^{-1}), $\dot{\varepsilon}_0$ is the reference plastic strain rate (s^{-1}), T is the temperature of the work material ($^{\circ}C$), T_m is the melting temperature of the work material ($1399^{\circ}C$) and T_{room} is the room temperature ($20^{\circ}C$). The yield strength [MPa], the hardening modulus [MPa], the strain rate sensitivity coefficient, the hardening coefficient and the thermal softening coefficient are respectively represented by the coefficients A , B , C , n and m [5].

Table 3.6 Young's modulus of AISI 316L steel [4].

Temperature [°C]	Young's Modulus [GPa]
20	195.6
100	191.2
200	185.7
300	179.6
400	172.6
500	164.5
600	155.0
700	144.1
800	131.4
900	116.8
1000	100.0
1100	80.0
1200	57.0
1300	30.0
1400	2.0

Table 3.7 lists five different sets of work material constants discovered by various researchers for use in the J–C constitutive equation.

Table 3.7 AISI 316L's material constants for J–C constitutive model [5].

	A [MPa]	B [MPa]	C	n	m	$\dot{\epsilon}_0$
M1	305	1161	0.01	0.61	0.517	1
M2	305	441	0.057	0.1	1.041	1
M3	301	1472	0.09	0.807	0.623	0.001
M4	280	1750	0.1	0.8	0.85	200
M5	514	514	0.042	0.508	0.533	0.001

The five different methods were compared to an experimental study of AISI 316L's plastic properties [57], in order to understand their behaviour and choose the most accurate and appropriate model for this particular case. In the experimental study, the temperature of the work material was 200°C and, therefore, the same value was applied to the five models. A value of 0.01 was arbitrated for the strain rate.

As shown in Figure 3.4, models M1 and M5 have similar behaviours to the experimental study. A parametric study in which the strain rate and the temperature of the work material took different values was conducted in order to determine which model promotes the most accurate values, when compared to the experimental results obtained for the residual stresses. It was concluded that the best option was model M5, since it had a most appropriate behaviour throughout the different temperatures. Thus, this approach was applied to both models, LPBF and DED.

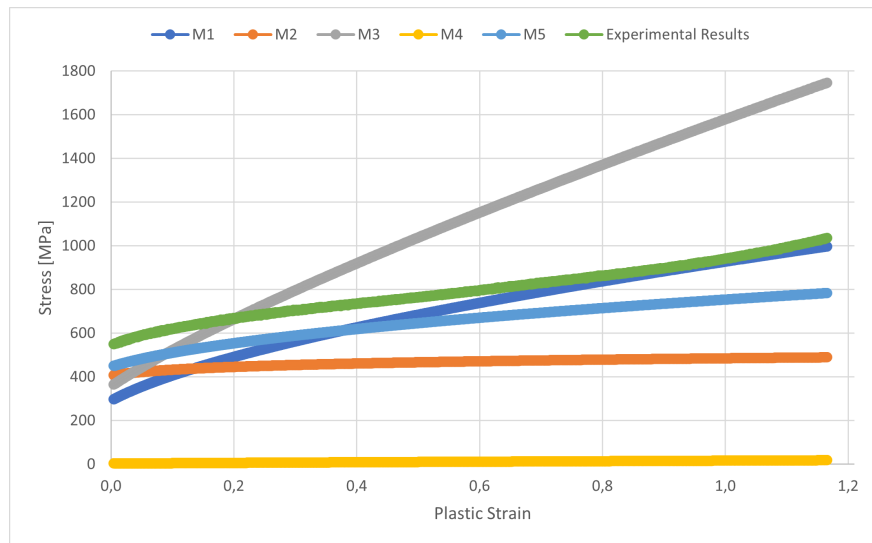


Figure 3.4 Behaviour of the five J-C's models and the experimental study of AISI 316L.

18Ni300 Maraging Steel

Maraging steels are iron-nickel alloys that have outstanding strength and toughness without sacrificing ductility. These alloys are primarily made of iron (65-75%Fe) and nickel (17-26%Ni), with additions of cobalt, molybdenum, titanium and aluminium, while carbon percentage is kept to a minimum (0.03%C). Because of their low carbon content, these alloys require several hours of heat treatment to precipitate intermetallic compounds, which result in the excellent mechanical properties previously mentioned [58].

Due to their nearly complete lack of interstitial alloying elements and exceptional weldability, maraging steels are often employed in AM [59]. When the material is melted by the laser to temperatures above the martensite start temperature (M_s) and then rapidly cooled to temperatures below the martensite finish temperature (M_f), it undergoes a quenching change from austenitic to soft martensitic structures.

In LPBF, a small amount of powdered material is melted, producing a melt pool, and is followed by rapid cooling and subsequent solidification. The precipitation hardening heat treatment may be then applied to the LPBF part, resulting in coherent intermetallic precipitation phases that provide the material with strength and hardness while maintaining ductility [60].

The properties of this material are not as well defined and available in the literature as steel 316L. Therefore, the values of the thermal properties were achieved experimentally [57] and are shown in Table 3.8. The values used for Poisson's ratio and Young's Modulus were, respectively, 0.3 and 190 [GPa]. Regarding the material's plastic properties, a J-C model was applied using values found in the literature [6], which are presented in Table 3.9.

Table 3.8 Thermo-physical properties of 18Ni300 maraging steel [4].

Temperature [°C]	Specific Heat [kJ/kg/°C]	Conductivity [W/m/°C]	Density [kg/m ³]	Thermal expansion [mm/mm/°C]
20	0.4449	15.81	8000	1.837×10^{-6}
100	0.4747	17.46		10.797×10^{-6}
200	0.5121	19.52		21.997×10^{-6}
300	0.5495	21.58		33.197×10^{-6}
400	0.5869	23.64		44.397×10^{-6}
500	0.6243	25.70		55.597×10^{-6}
600	0.6617	27.76		66.797×10^{-6}
700	0.6991	29.82		77.997×10^{-6}
800	0.7365	31.88		89.197×10^{-6}
900	0.7739	33.94		100.397×10^{-6}
1000	0.8113	36.00		111.597×10^{-6}

Table 3.9 Maraging steel's material constants for J-C constitutive model [6].

A [MPa]	B [MPa]	C	n	m	$\dot{\epsilon}_0$
758.423	172.147	0.0522	0.2258	0.7799	70

3.2 Thermo-mechanical Simulations

The main goals of an AM simulation are calculating the residual stresses in a component, reducing the gap between the intended and manufactured parts by optimizing the manufacturing process and examining how a part performs in an assembly with other components under realistic loading circumstances.

The toolpath-mesh intersection module is one of the basis of the Abaqus AM technology. For the simulation of an AM process, Abaqus offers two options: a thermo-mechanical simulation and an eigenstrain-based simulation.

Abaqus provides general-purpose simulation tools, allowing the user to specify the boundary conditions, loads, interactions, restrictions and material models needed to describe the physics of AM processes. In addition, for these simulations, multiple analytical approaches are available, which take into consideration machine information and process parameters such as laser power, layer thickness and toolpath.

The feature for AM processes simulation in Abaqus is built on a user subroutine infrastructure and keyword interface that allows for a high level of control and customization [61].

3.2.1 Thermo-mechanical analysis of PBF process

A single layer of raw material is deposited by a recoater or a roller blade in a powder bed-type additive manufacturing process. The part is then scanned with a high powered laser in a single cross-section across the raw material layer to fuse it with the previously

deposited layer underneath. In a structural or thermal analysis, layer-upon-layer raw material deposition is represented by progressive element activation and laser-induced heating is simulated by a moving heat flux [42].

Specifying progressive element activation

Progressive element activation in a structural or thermal study is used to model the layer-by-layer deposition of raw material from a recoater. In this study, full activation is used, which means that the volume fraction of an element is set to one when it is active. To fully define the deposition process, the following steps are required:

- i. Defining the motion of the recoater's center point, following the convention for infinite line toolpath-mesh intersection;
- ii. Creating a table collection with the name "ABQ_AM". A parameter table of type "ABQ_AM_MaterialDeposition" must be included in the table collection;
- iii. Include a reference to the material deposition event series in the parameter table and set the deposition process type to "Roller";
- iv. In the progressive element activation, refer to the table collection.

Abaqus automatically activates elements based on the material deposition sequence. All of the definitions required for special-purpose AM processes are available in a dedicated collection of parameter table, property table and event series types [42].

Radiation and convection cooling occur on the continuously evolving free surfaces in an AM process. Abaqus keeps track of the free surfaces that correspond to the construction part's present shape. During progressive element activation, film and radiation conditions are applied to the facet region of an element [62].

Specifying a concentrated moving heat source

If the size of the finite elements utilized in a thermal analysis is substantially bigger than the size of the laser spot, the laser spot can be approximated as a concentrated moving heat flux. To completely characterize the focused moving heat source, the required steps are:

- i. Defining the laser's scanning trajectory and power, using the convention for point toolpath-mesh intersection;
- ii. A parameter table of type "ABQ_AM_MovingHeatSource" must be present in the table collection "ABQ_AM";
- iii. Include a reference to the event series for the point heat source in the parameter table and set the heat source type to "Concentrated".

Abaqus automatically computes and applies moving heat fluxes to each element based on the scanning trajectory [42].

3.2.2 Thermo-mechanical analysis of LDED-type processes

During LDED, the material is deposited by a nozzle mounted on a multi-axis arm while being melted by laser beam. To accurately capture the melting effect in structural analysis, an initial temperature representing a relaxation temperature above which thermal straining induces negligible thermal stress is frequently assigned. The initial temperature of the prism in the structural analysis is set to the melting temperature of the steel 316L, 1399°C [63].

Specifying progressive element activation

Progressive element activation is used in a structural or thermal study to replicate raw material deposition from a moving nozzle. The nozzle's cross-section and the material-depositing bead are both considered to be rectangular. To fully specify the deposition process, the user will need to follow several steps:

- i. In an event sequence, define the nozzle's motion;
- ii. A parameter table of type "ABQ_AM_MaterialDeposition" and a parameter table of type "ABQ_AM_MaterialDeposition_Bead" must be present in the table collection "ABQ_AM";
- iii. Include a reference to the nozzle motion event series in the parameter table of type "ABQ_AM_MaterialDeposition," and set the deposition process type to "Bead";
- iv. Define the process parameters, such as the height and breadth of the bead, in the parameter table of type "ABQ_AM_MaterialDeposition_Bead";
- v. In the progressive element activation, refer to the table collection.

Abaqus automatically activates parts based on the specified nozzle trajectory [64]. During printing, previously exposed material surfaces are covered and new free surfaces are created by the deposition of new material. Surface convection and radiation are defined on the ever-changing free surfaces [63]. Figure 3.5 shows a representation of the element activation in the LDED process.

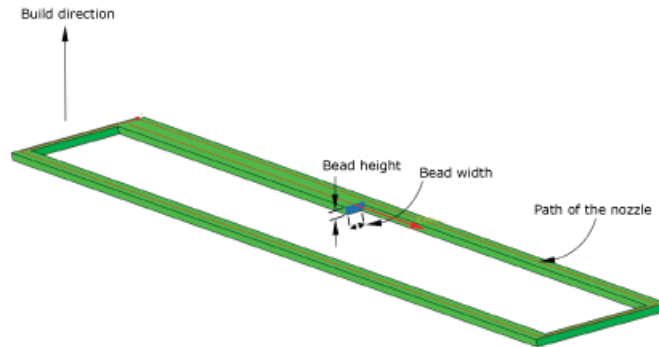


Figure 3.5 Progressive element activation for LDED process [64].

Specifying a moving heat source with a Goldak distribution

The heating by the laser during deposition is modeled using a moving heat flux with a Goldak distribution. It is assumed that the laser beam spot at the intersection with the part surface is circular. The laser scanning path is defined by the same event sequence that is used to define the material deposition sequence. The energy absorption efficiency has been calibrated to be 40% when using this distribution [63].

The laser power can be spread throughout a volume using the Goldak rule of laser energy distribution if the size of the finite elements employed in a thermal study is comparable to the size of the laser spot. To completely characterize the moving heat source, it is necessary to:

- i. Define the laser spot's trajectory in an event sequence, similar to how the concentrated moving heat source is defined;
- ii. A parameter table of type "ABQ_AM_MovingHeatSource" and a parameter table of type "ABQ_AM_MovingHeatSource_Goldak" must be present in the table collection "ABQ_AM";
- iii. Include a reference to the moving heat source's event series in the parameter table of type "ABQ_AM_MovingHeatSource" and set the heat source type to "Goldak";
- iv. Define the Goldak distribution parameters in the parameter database of type "ABQ_AM_MovingHeatSource_Goldak".

Abaqus automatically computes and applies moving distributed heat fluxes based on the Goldak distribution and scanning trajectory [42].

3.2.3 Toolpath and scanning strategy

Abaqus AM plug-in introduces the laser movement along the part as well as the roller deposition using event series files. *Simplify3D Software* was used to produce G-code files.

Then, a Python script provided by *Simulia Dassault Systems* converted the resulting G-code into the laser and roller event series. The laser power (Watts), roller deposition duration (seconds) and roller position on the build plate are all introduced by the user. The values for the prism are, respectively, 400, 1 and 0.5 and, for the bridge, the values are 200, 1 and 0.5. The final value indicates that the roller is centered in relation to the component. The laser takes approximately 15.7 seconds to complete one layer of the prism and 15.4 seconds to complete one layer of the bridge.

3.2.4 Level of fidelity

In terms of both time and space, AM is a multi-scale subject. The mesh size and time step incrementation allows the user to adjust the scale and quality of the solution. At the high end of the fidelity spectrum, there are often two types of thermo-mechanical simulations: process-level simulation (High fidelity) and part-level simulation (Low fidelity).

A detailed process simulation is performed using:

- i. A refined mesh size: at least one element per powder layer thickness and a few elements across a melting-affected portion are used in a full process simulation;
- ii. A short time increment, usually on the millisecond scale;
- iii. A thorough laser energy distribution as well as a volumetric input tool geometry.

This level of detail enables to capture the HAZ's fast and large temperature gradients, resulting in correct residual stresses and distortions. In the thermal model, the latent heat of fusion is used to describe thermal energy release and absorption. The annealing temperature used in the material's plasticity model captures the influence of melting on thermal strains in the mechanical model. On the other hand, this kind of simulation requires a high computational cost and convergence difficulties produced by non-linear material qualities under rapidly changing temperature conditions might also affect it.

The part-level simulation is a computationally efficient method for accurately predicting distortions and stresses in printed parts. This simulation is performed using:

- i. A coarse mesh: has a small number of physical layers per element;
- ii. A big-time increment: the events are grouped together in time. Each element layer has one or more time increments;
- iii. A discrete point tool geometry without laser energy distribution.

Because the heat source's movement is lumped in space and time, the heat transfer analysis can usually capture far-field temperatures but not local rapid temperature evolution. As a result, the models rarely include an accurate melting and solidification history. To appropriately model melting effects in the stress analysis, a temperature indicating the material's relaxation temperature at which thermal straining causes minimal thermal

stress must be assigned. The relaxation temperature is the temperature at which the initial thermal contraction occurs when an element is activated, and it can be calibrated using physical tests or detailed-process level simulations [48]. The relaxation temperatures, $\Theta_{SR} = 565^\circ\text{C}$ and $\Theta_{SR} = 550^\circ\text{C}$, for Steel 316L and Maraging Steel, respectively, are taken from the literature [65, 66]. This variable is implemented in the material's plasticity model.

3.2.5 Boundary conditions and interactions

The boundary conditions (BC) are critical in the process's corrective modeling. In the thermal models, the initial temperatures of the part and build plate are set to 25°C . The thermal data for each increment from the transient heat transfer study is used as predefined field in the structural analysis. The fundamental BC in the mechanical models is the fixing constraint of the substrate's bottom surface. The three degrees of freedom of the displacement are all set to zero. This eliminates distortion of the baseplate caused by the printing process.

The contact interaction between the substrate and the part is modelled as a "tie" constraint used in the thermal model to unify the temperatures of the two surfaces in contact. The interaction is applied to the same surface for the structural analysis. A "tie" condition is used once more, which means that the nodes belonging to the two components unify their translational and rotational movements.

3.2.6 Printing parameters

The printing process can be customized using a number of settings, for example, the energy absorption coefficient, laser energy distribution parameters, element activation type and inactive element behavior. For the LPBF model, an absorption coefficient η equal to 0.46 was selected. This parameter's accuracy is critical since it restricts proportionally the amount of energy that the part receives from the laser.

Table 3.10 summarizes the parameters that make up the Goldak spatial energy distribution, represented in Figure 2.24. They match the melting pool dimensions calculated by Keller using similar printing settings in his experimental simulation work [7].

Table 3.10 Goldak's spatial energy distribution parameters [7].

Parameter	Value
a	0.03
b	0.085
c_f	0.03
c_r	0.03
f_f	1
f_r	1

Each simulation is carried out in three steps. In the first step, the deposition process is modeled with a small time increment. The second and third steps, with larger time increments of 10 seconds and 100 seconds, simulate additional cooling periods after the build.

Lastly, the follow deformations option controls whether or not inactive elements can move and follow the part's expected deformation. Inactive elements do not contribute to the overall response of the model by default and their degrees of freedom aren't part of the solution. This method only works in stress-displacement analysis when the displacements are minimal. If this is not the case, the dormant pieces may become overly deformed before being triggered, causing problems with convergence or unsatisfactory outcomes so, as a result, the option is enabled [67].

3.2.7 Cooling

The two heat-transfer mechanisms of cooling to the environment are convection and radiation. Both are subjected to a sink temperature of 25°C. All of the free surfaces of the model, except the bottom surface of the build plate, are set to a typical film coefficient for inert gas atmosphere of 0.018 [mW/(mm²·°C)]. The emissivity of the surface exposed to the atmosphere is a critical characteristic in the radiation, the selected value was 0.45 [68].

3.2.8 Mesh

A 3D 8-nodes linear brick element was employed in both the thermal and mechanical simulations. The structural element has the designation C3D8 and the heat transfer element is DC3D8. Along the printed area, the spatial distribution of the elements is uniform or "mapped." The printing simulation's results are influenced by the element sizes. In order to acquire correct findings in an acceptable computational time, each model undergoes a convergence study to the component mesh.

3.3 Parametric analysis

Parametric simulations are those in which all of the parameters are kept the same except for one, in order to examine the final result sensitivity to input variation. When dealing with commercial software packages, parametric studies are critical, because without a solid understanding of the effects of a simulation's user-controlled parameters, valid inferences cannot be drawn from the results. Furthermore, this approach enables the determination of the minimum parameters that ensure solution convergence while reducing computational effort.

Researchers have used different methodologies to evaluate the residual stress and explore scanning strategies with the intention of lowering or distributing this stress more

uniformly across the part [69]. Understanding the influence of the scanning strategy on SLM parts is a challenge in itself since there is a multitude of parameters connected to this parameter. Changing the length of the scan vectors, their direction, the order of scanning and the rotation of each consecutive layer can result in a wide range of scanning tactics [70].

Although processing variables such as laser power, scan speed, layer thickness and volumetric energy density have a high influence on the residual stresses developed in PBF processing, it is frequently reported that the effect of one variable in particular overshadows the others: preheating the baseplate. It is commonly accepted in the literature, and it has been demonstrated by both experimental analysis and simulations, that increasing the temperature of the baseplate reduces the magnitudes of residual stress [20].

The main objective of these simulations was the study of three different variables:

1. Mesh refinement;
2. Laser scanning;
3. Preheat of the baseplate.

The sets of simulations performed and the values chosen for each variable that was taking into account for the parametric studies are presented in Table 3.11.

Table 3.11 Description of the performed simulation's conditions.

Process	Part	Laser Strategy	Mesh	Preheat Temperature
PBF	Prism	0°, 120°, 240°	0.5, 1.0, 2.5	N/A
		0°	1.0	N/A
		90°	1.0	N/A
PBF	Pism	0°, 120°, 240°	1.0	100°C, 250°C
PBF	Bridge	0°, 90°	0.5	N/A
		0°, 120°, 240°	0.5	N/A
DED	Prism	0°, 120°, 240°	1.0	N/A
		0°	1.0	N/A

Firstly, the influence of the mesh size on the residual stresses of the PBF model was studied, using the prism and the scanning strategy defined previously, repeating orientation every three layers (0°, 120°, 240°). The mesh size dimensions vary from 2.5 [mm] to 0.5 [mm].

The next step was to study the influence of the laser strategy by performing two more simulations which had a single orientation for all the layers: 0° and 90°.

The last study directed with the prism was the influence of the substrate's preheat temperature. In the early simulations, as previously mentioned, the initial temperature of the baseplate is set at 25°C, however, according to the literature, results can be highly affected when the baseplate is formerly heated. In order to analyse the influence of this variable, the results of three temperatures were compared: 25°C, 100 °C and 250°C.

Following a thorough analysis of the PBF model, the second numerical model developed during this dissertation was also examined. Similar parameters were applied to the DED model with the intention of acknowledging the difference between the residual stresses induced by both models. The prism with the mesh size of 1 [mm] was used for this effect. A study of the influence of the scanning strategy on the DED process was also conducted.

After evaluating multiple parameters on the simpler geometry, the residual stresses on the maraging steel benchmark bridge were analysed, using the PBF model. Since it is a much complex geometry, it was necessary to choose smaller mesh sizes to promote accurate results. A mesh of 0.5 [mm] was applied and the evolution of the residual stresses in different locations was examined.

A comparison between the numerical results achieved for the prism and the bridge using the PBF model and the experimental data obtained from the MAMTool study was conducted, in order to determine the accuracy of the model. In the experimental study, the analysis of the prism is very thorough, as the residual stresses in the longitudinal, transverse and build directions are measured in different surfaces (planes xy , xz and yz). Regarding the maraging steel bridge, in the experimental study four parts printed on the same baseplate were analysed. In this case, two different laser scanning strategies were used and the residual stresses were measured on the bridges' top prominences, in the $y=2.5$ [mm] plane. The specific conditions of the experimental studies are further explained in Chapter 4.

Lastly, a study of the displacement field when the bridge is gradually removed from its baseplate was conducted and the results were compared to experimental results.

Chapter 4

Results and Discussion

In this Section, the results of the numerical simulations described in Chapter 3 are presented and discussed in further detail.

4.1 Parametric simulations

The residual stress generated by this unique thermal cycle in MAM is a major concern for the fabricated parts, since high residual stress gradients can cause component distortion.

In most simulations, the monitored nodal variable outputs were consistent throughout. In the case of the prism, the residual stresses in the longitudinal, σ_{xx} , and transverse, σ_{yy} , directions were the monitored nodal variable outputs on the $z=20$ plane. On the other hand, on the xz plane ($y=0$), the monitored nodal variable outputs were the longitudinal stresses and the stresses on the build direction, σ_{zz} . Figures 4.1 and 4.2 represent the nodes established to measure these variables.

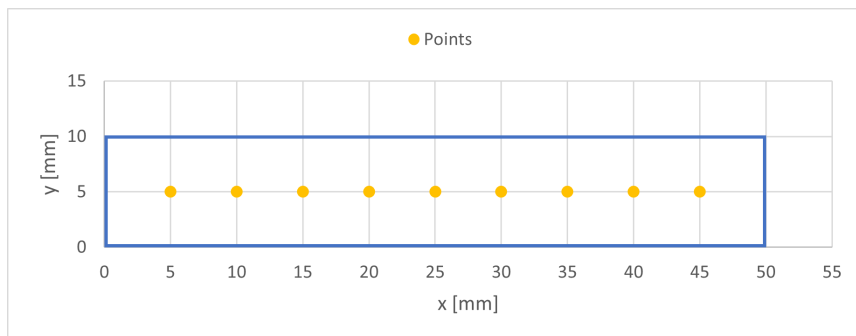


Figure 4.1 Representation of the analysed nodes on the $z=20$ plane.

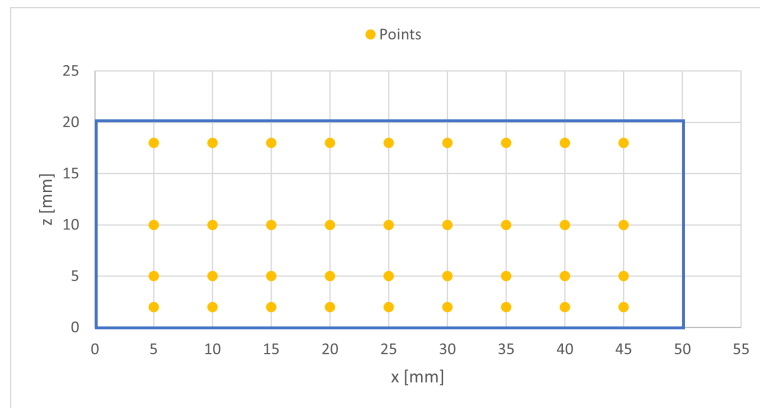


Figure 4.2 Representation of the analysed nodes on the xz plane.

The following sections present the results of the different simulations and models developed. Firstly, the PBF model will be thoroughly examined using the prism made of 316L steel, which will include studies on the influence of three variables on the residual stresses:

1. Mesh size;
2. Scanning strategy;
3. Preheat temperature.

Secondly, the DED model's results will be presented and, then, a comparison between the two models will be conducted. Afterwards, the results of the benchmark bridge made of maraging steel are also explored, in order to analyse the performance of the PBF model with a more complex geometry. The numerical results of the two parts used in the PBF model will be compared to experimental data and, lastly, an analysis of the displacement field when the bridge was gradually removed from its baseplate is performed and compared to experimental results.

4.2 Mesh size

The results of the mesh size's effects on residual stress are examined in this section. The studied component is the prism made of 316L Stainless Steel. Three simulations were performed using the same scanning strategy for the three different sizes represented in Figure 4.3: 0.5 [mm] will be referred to as mesh 1, 1.0 [mm] will be referred to as mesh 2 and 2.5 [mm] will be referred to as mesh 3. The laser strategy implemented in this study was the repeating orientation every three layers (0° , 120° , 240°).

The results of each variable output are presented in the following sets of graphs. Figure 4.4 explores the data pertaining to the residual stresses in the x and y directions on the top surface of the prism ($z = 20$).

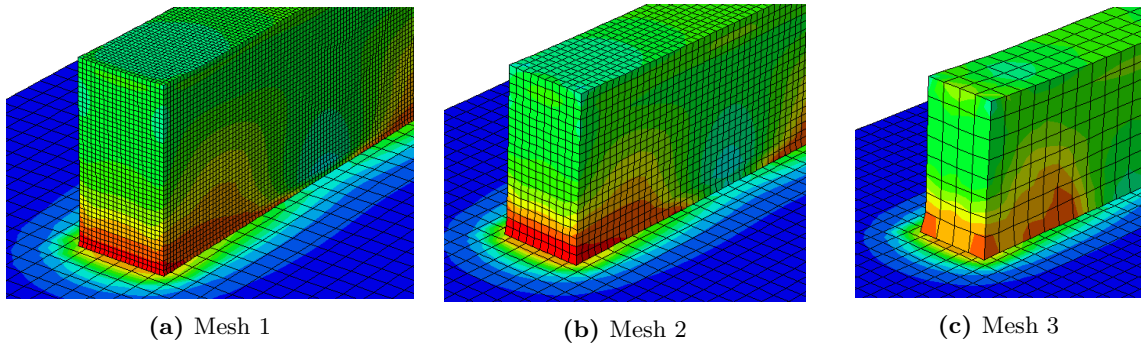


Figure 4.3 Abaqus’ mesh refinement of the prism and substrate (von Mises distribution).

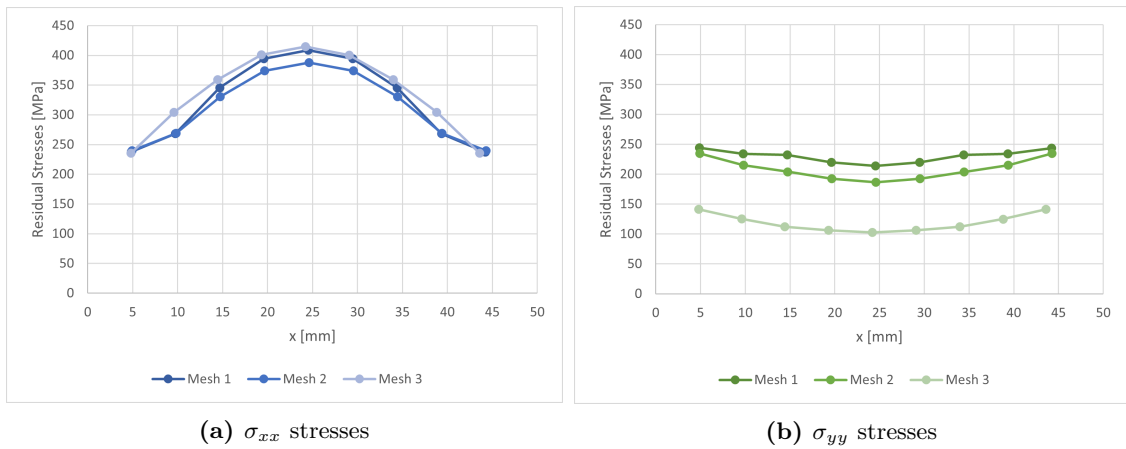


Figure 4.4 Evolution of the σ_{xx} and σ_{yy} stresses throughout the $z=20$ plane.

Due to the rapid cooling rate that occurs in the SLM process, the shrinkage is considered to be anisotropic. As a result, the distribution of residual stress in the top surface layer is not uniform. Below the top surface layer, there are tensile and compressive residual stresses.

Regarding the σ_{xx} stresses, the three simulations show similar behaviour throughout the nodes, however, the values vary between each mesh size. At the plane’s midpoint, approximately $x=25$ [mm], there’s a significant difference between the three meshes, which is presented in Table 4.1.

Table 4.1 Residual stresses at the midpoint of xy plane ($x=25$).

	Mesh 1	Mesh 2	Mesh 3
σ_{xx} [MPa]	408.9	387.5	414.5
σ_{yy} [MPa]	214.0	186.5	102.8

On the other hand, the σ_{yy} stresses of the three meshes are notably different, particularly the values obtained for mesh 3. This can indicate that mesh 3 does not promote an accurate description of the residual stresses developed in the prism during the AM process

given that its width is only 10 [mm], therefore, the mesh contains only four elements in the y direction. Because of the greater number of elements in the x direction, these issues were not as noticeable in the longitudinal stresses. Since the absence of elements covering the prism in the y direction was extremely detrimental in calculating transverse stress, a smaller mesh size should be taken in consideration to simulate this process.

After analysing the xy plane, the stresses in the x and z directions were examined on plane xz . The analysis consisted in collecting values at four levels: $z=18$, $z=10$, $z=5$ and $z=2$. Figures 4.5 and 4.6 represent the evolution of the residual stresses throughout the frontal face of the prism.

Regarding the σ_{xx} stresses, the curves present a parabolic and symmetric behaviour. Mesh 3 shows once again a significant discrepancy compared to the other sizes, however, meshes 1 and 2 have a more similar behaviour at all levels. The stresses at the higher level ($z=18$) are smaller than the ones developed at the lower levels. The maximum values are at the midpoint ($x=25$), except for the lowest level ($z=2$), where the stresses are higher at the extremities of the prism.

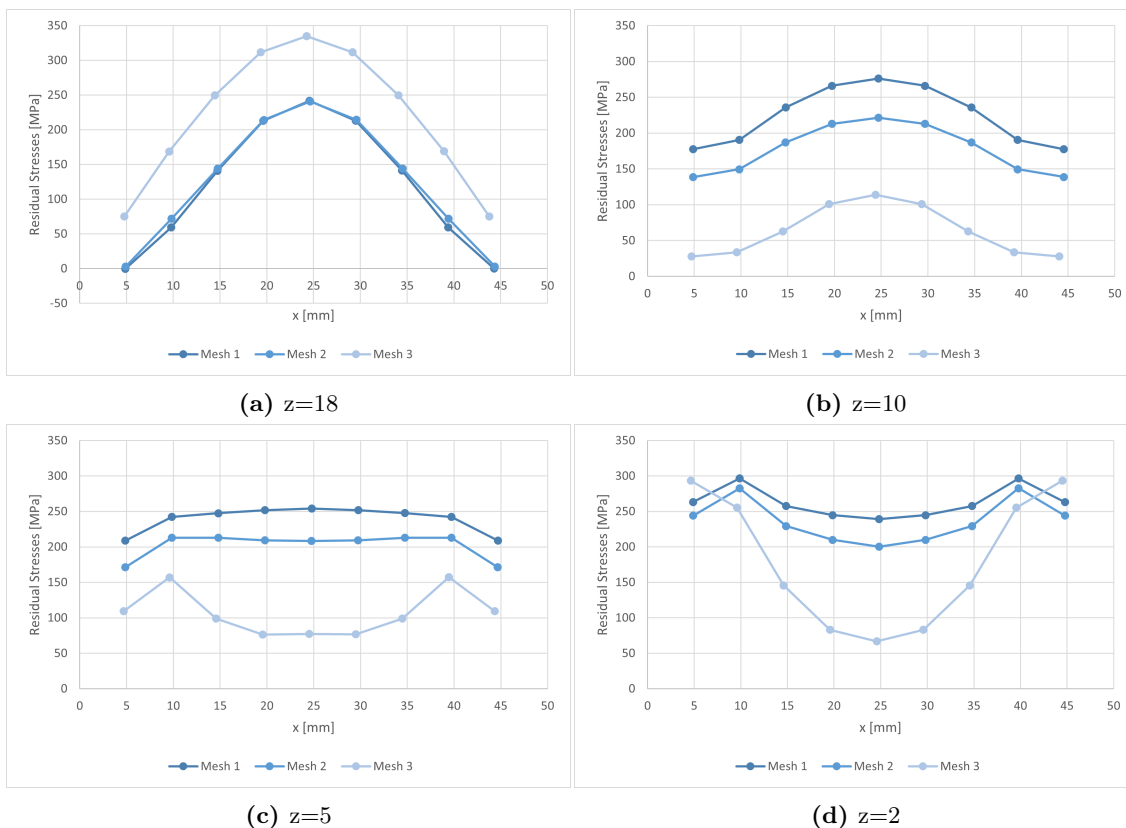


Figure 4.5 Evolution of σ_{xx} stresses throughout the $y=0$ plane.

The stresses on the build direction, σ_{zz} , are considerably higher than the other directions. For example, at $z=10$, the stress of the midpoint reaches 320 [MPa] and the stresses developed at the prism's extremities are close to 450 [MPa]. In the first layers, the residual stresses are higher and more irregular throughout the length due to the severe thermal shock that occurs between the part and the substrate since, in this case, the substrate was not preheated. In a LPBF process, with the increasing number of layers, the heat accumulates in the formed layers reducing the temperature gradient in the component. As a result, the tensile stress in the upper layers are smaller.

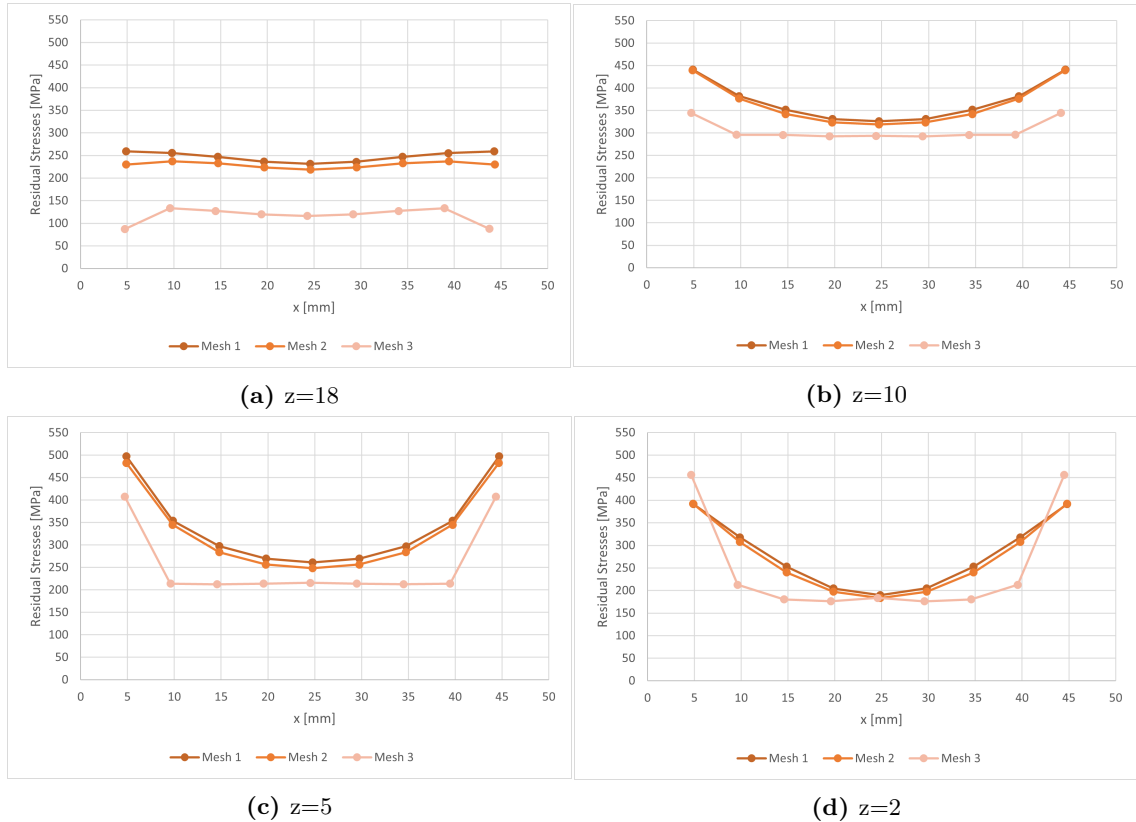


Figure 4.6 Evolution of σ_{zz} stresses throughout the $y=0$ plane.

After analysing the influence of the mesh size on the residual stresses, mesh 2 was elected to be used in the following simulations since the two most refined sizes (mesh 1 and mesh 2) presented similar behaviours for the studied variable outputs, however, mesh 2 reduces considerable the computational time: the total CPU time decreases from 97.8 hours to 15.1 hours, for the prism simulation.

Figures 4.7 to 4.9 represent the stress distribution of the prism in the different directions, extracted from $y=5$ [mm] plane. Oppositely to the superficial distributions (Figures 4.5 and 4.6), in this case the stresses are mostly compressive. These compressive stresses diminish from the bottom to the top, converting to tensile stress in the upper layers.

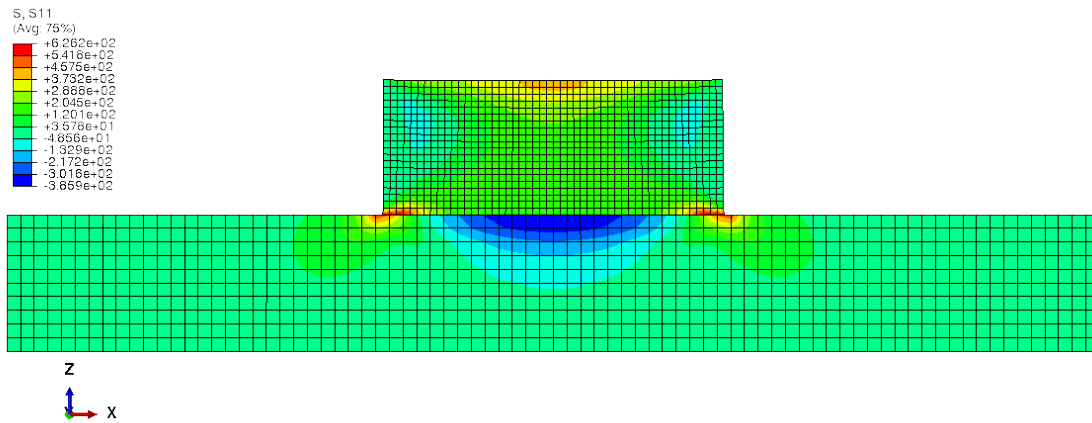


Figure 4.7 σ_{xx} stress distribution, extracted from $y=5$ plane in the prism.

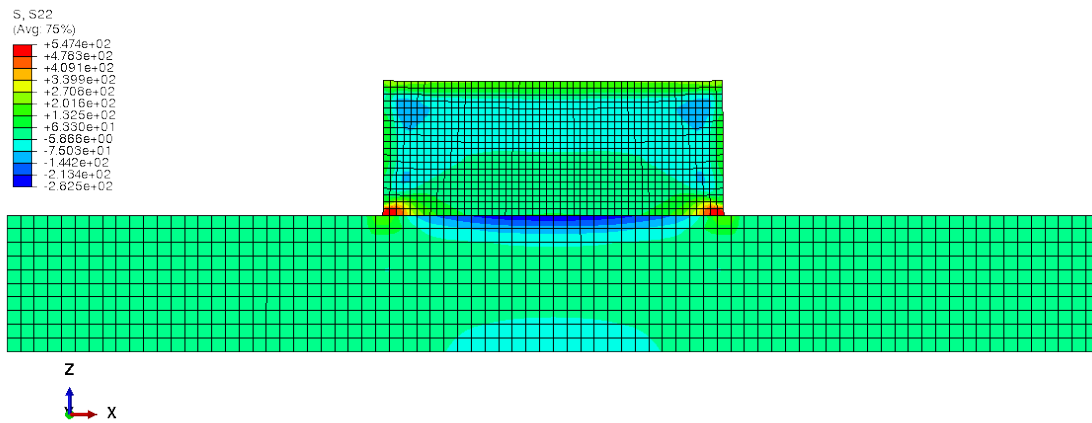


Figure 4.8 σ_{yy} stress distribution, extracted from $y=5$ plane in the prism.

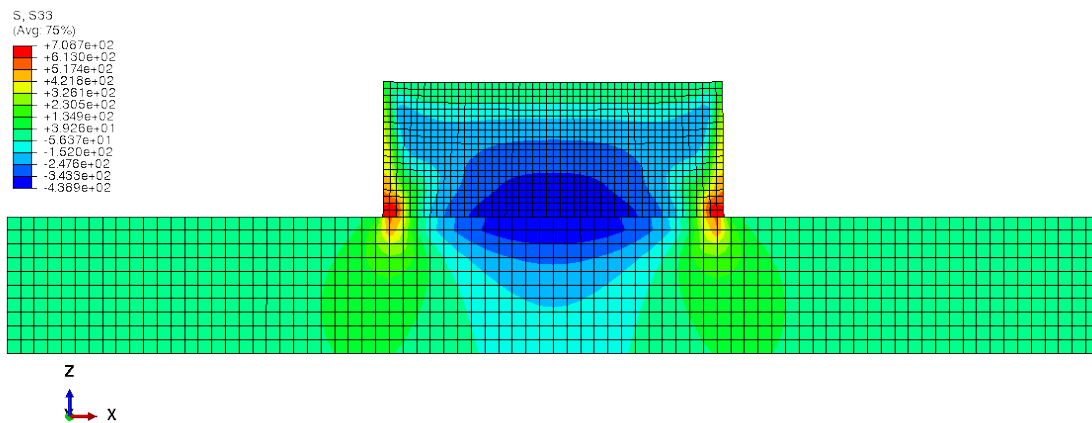


Figure 4.9 σ_{zz} stress distribution, extracted from $y=5$ plane in the prism.

4.3 Scanning strategy

There is a wide number of possible ways to scan a single layer and various scan strategies have been studied in regards of residual stresses. The general result from these studies is that restricting the length of the scan vectors is advantageous and modifying this length has the greatest conceivable impact on deformations and residual stresses when compared to other process variables, except preheating [71].

In this section, the influence of the scanning strategy on the residual stresses of the prism is studied. Three types of scan strategies were used: zig-zag with indication of the 120° rotation for consecutive layers (0°, 120°, 240°), which will be referred to as Laser 1, zig-zag with 90° orientation for every layer, which will be referred to as Laser 2, and zig-zag with 0° orientation for every layer, which will be referred to as Laser 3.

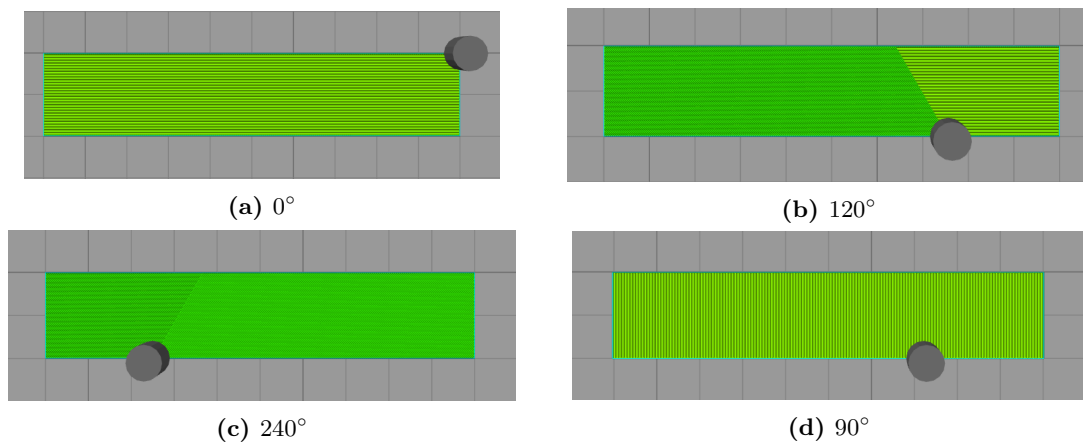


Figure 4.10 Representation of the four used orientations: 0°, 120°, 240° and 90°.

The following sets of figures represent the achieved results for the same variables outputs analysed in Section 4.2: the evolution of the σ_{xx} and σ_{yy} stresses throughout the xy plane and the evolution of the σ_{xx} and σ_{zz} stresses throughout the xz plane.

By analysing Figures 4.11, 4.12 and 4.13, it is possible to conclude that, in this case, the orientation of the laser during the layers' construction does not have a significant impact on the developed residual stresses. According to the literature [71], this values can be severely affected if the scan strategy is more complex, for example, using the island scanning with a 90° rotation or the fractal scanning pattern, however, *Simplify3D Software* does not support these options. Additionally, these results may be related to the fact that the part has a very simple geometry and does not require the need for supports. This variable may have a more significant impact when the geometry is more complex.

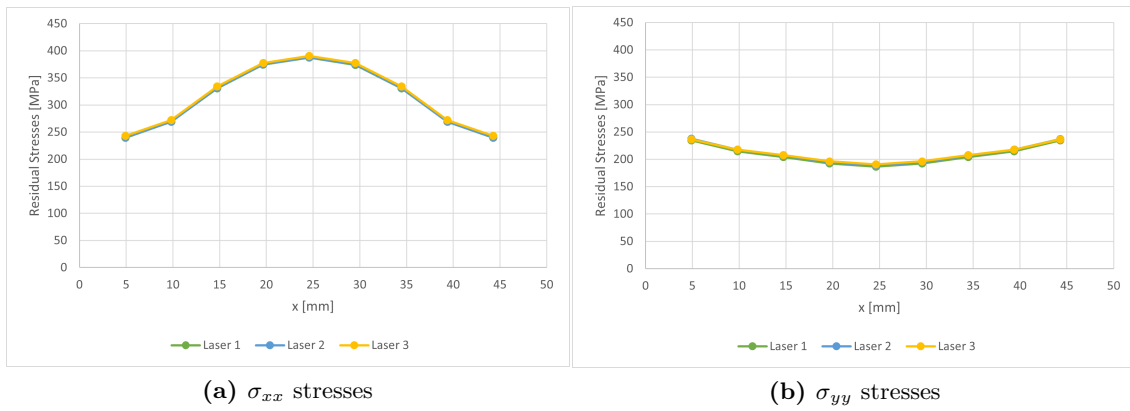


Figure 4.11 Evolution of the σ_{xx} and σ_{yy} stresses throughout the $z=20$ plane (laser scan strategy effect).

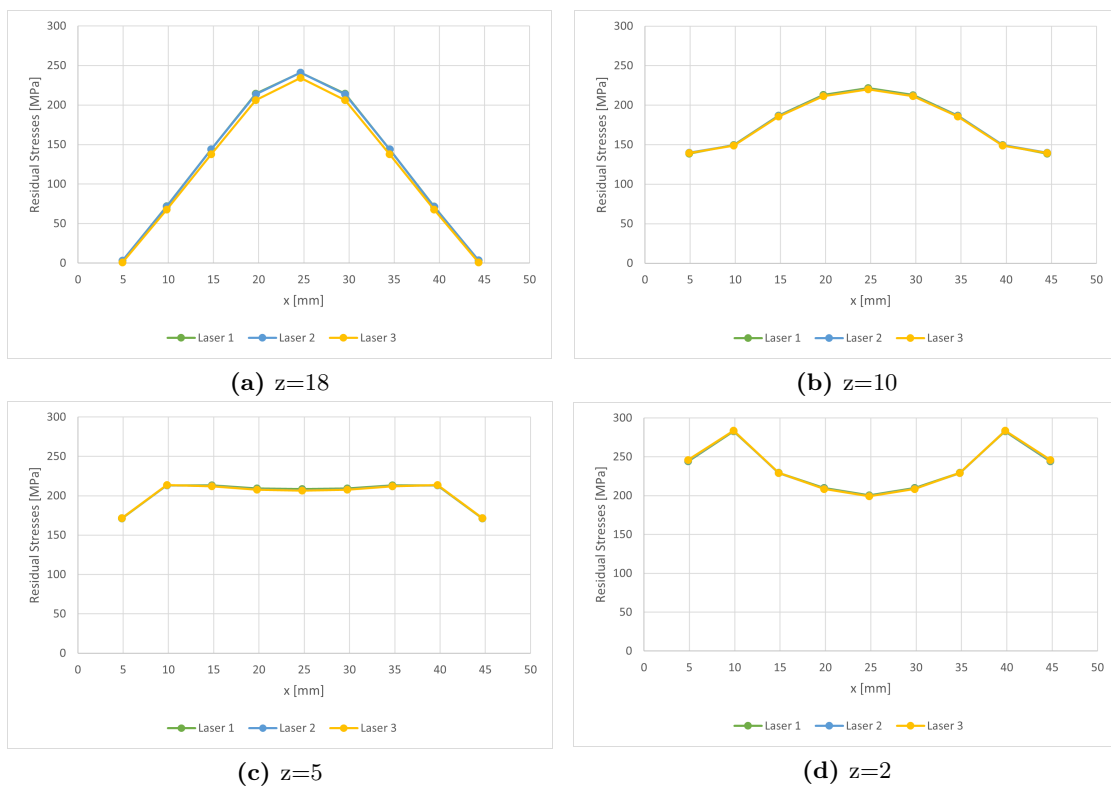


Figure 4.12 Evolution of σ_{xx} stresses throughout the $y=0$ plane (laser scan strategy effect).

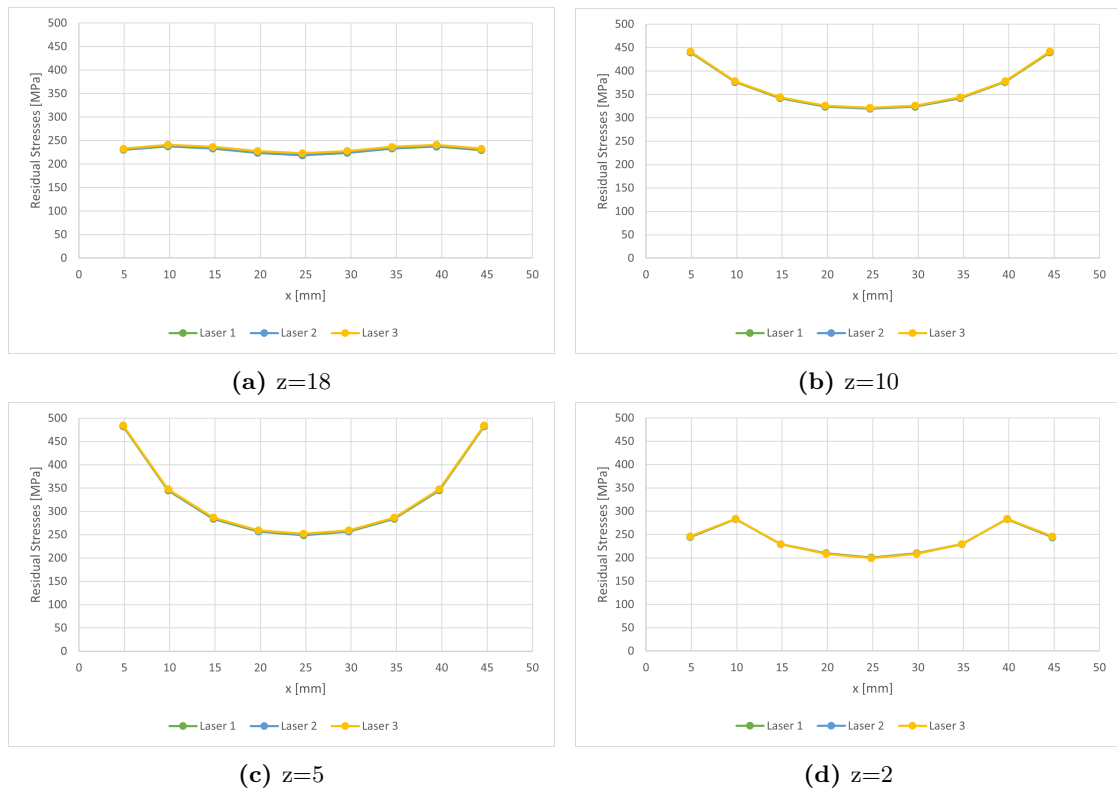


Figure 4.13 Evolution of σ_{zz} stresses throughout the $y=0$ plane (laser scan strategy effect).

4.4 Preheat Temperature

During the build stage of the process, the preheat temperature is the temperature at which the baseplate is heated. This temperature is crucial in order to avoid higher heat gradients caused by the temperature difference between the metal in its melting phase and the surrounding environment. Lower distortions and, as a result, smaller residual stresses are predicted to result from higher preheating temperatures.

In this section, the influence of the preheat temperature on the final residual stresses is analysed. The values used to conduct these simulations were 25°C, 100°C and 250°C. The curves of 25°C are used as the reference points, since in the experimental study and in all the previous simulations, the substrate was not preheated but maintained at 25°C.

By analysing Figures 4.14 to 4.16, it is possible to conclude that when the baseplate is heated, the final residual stresses are smaller, particularly in the midsection of the prism. Using the values of the 25°C curve as a reference, it is visible that the residual stresses decrease as the preheat temperature increases, as the highest difference observed is for the temperature of 250°C. However, it is reasonable to assume that, if higher temperatures were continuously applied to the substrate, this variable would stop having an impact on the residual stresses' values and they would eventually stabilize.

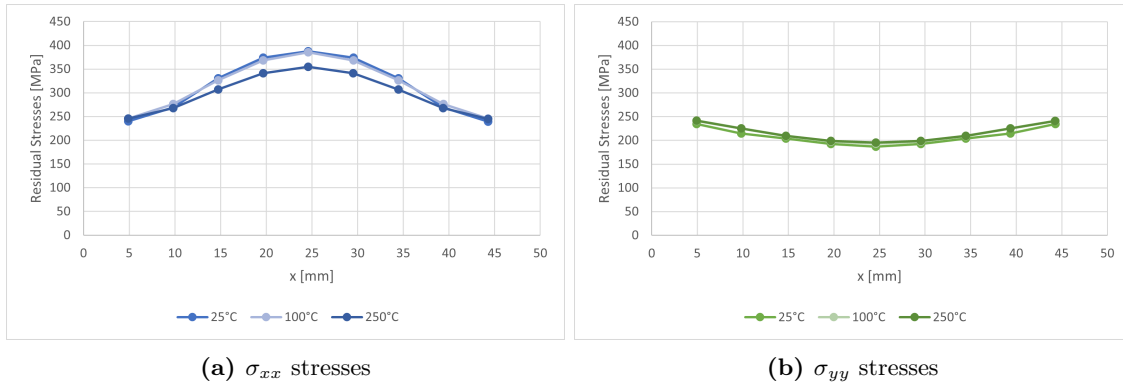


Figure 4.14 Evolution of the σ_{xx} and σ_{yy} stresses throughout the $z=20$ plane (preheat temperature effect).

Regarding the xy plane, this variable has a greater influence on the longitudinal stresses, as a decrease of approximately 35 [MPa] can be achieved when using a temperature of 250°C.

The stresses in the build direction are still very high and the heating of the substrate does not seem to have neither a big or regular impact on the results. Nonetheless, a decrease of 27 [MPa] was achieved for the lowest level ($z=2$) when using a temperature of 250°C, which can represent the higher effect of this variable on the initial layers, as the temperature gradients in the component can be severe.

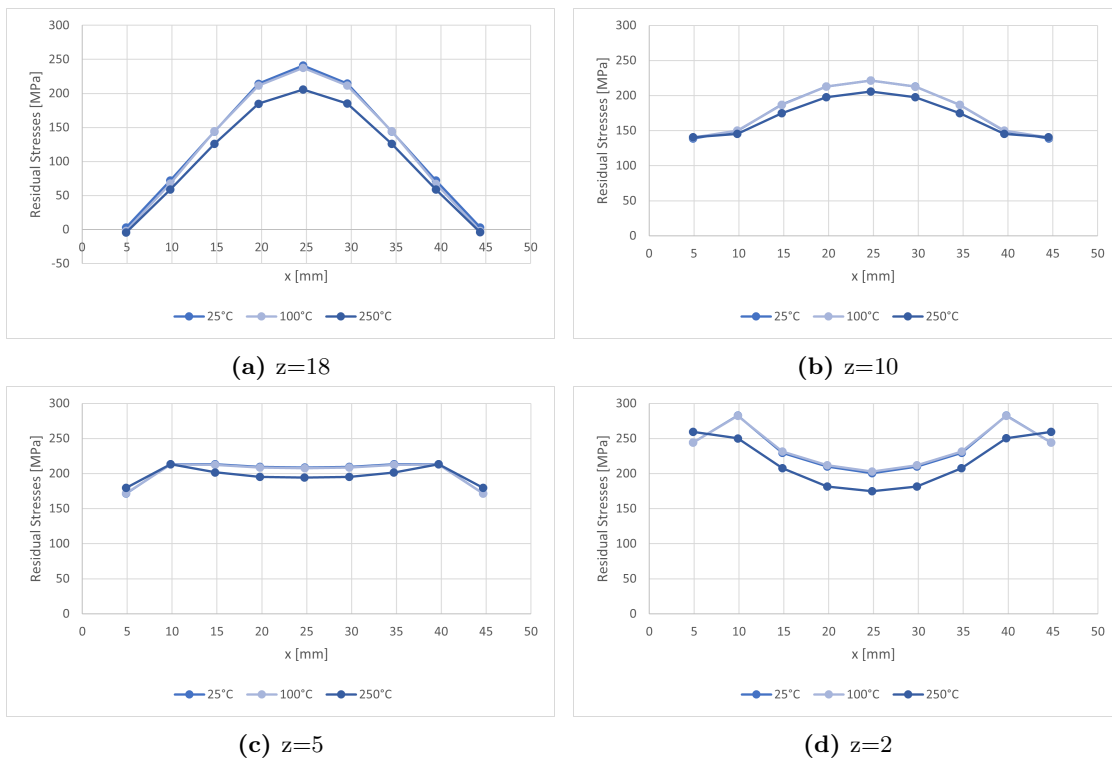


Figure 4.15 Evolution of σ_{xx} stresses throughout the $y=0$ plane (preheat temperature effect).

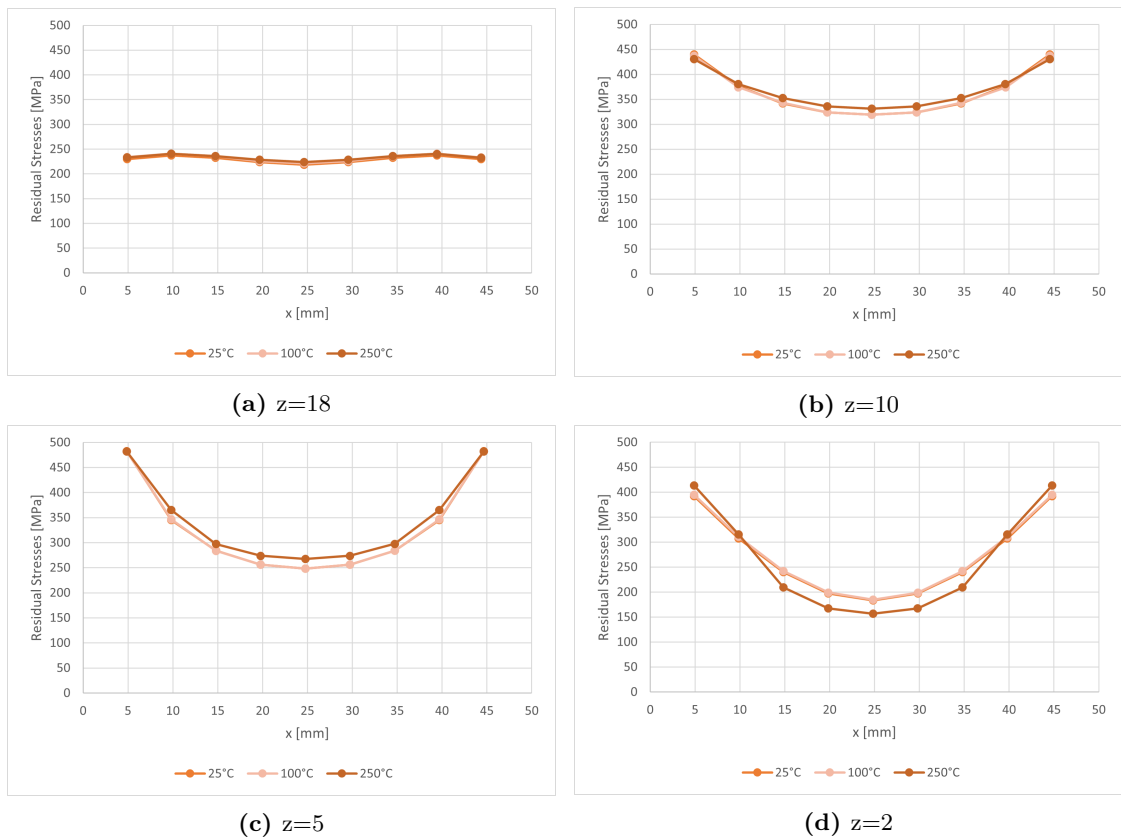


Figure 4.16 Evolution of σ_{zz} stresses throughout the $y=0$ plane (preheat temperature effect).

4.5 DED results

In order to analyse the DED process, a mesh size of 1 [mm] and two different scanning strategies were used: the zig-zag with indication of the 120° rotation for consecutive layers, which will be referred to as Laser 1, and the zig-zag with 0° orientation for every layer, which will be referred to as Laser 2.

In Figure 4.17 it can be observed that the two scan strategies induce different residual stresses throughout the prism's length. In comparison to the graphs analysed in Section 4.3, it can be concluded that this variable has a more significant impact on the results of this model than on the PBF model. Table 4.2 contains the values of σ_{xx} and σ_{yy} for a chosen point ($x=40$), where the influence of the scan strategy is more noticeable.

In the xz plane, this oscillation of values between the two strategies is also visible in both x and z directions, which are represented in Figures 4.18 and 4.19. In the x direction, this difference is slightly higher and can be of 10 [MPa] for the same location. Similarly to PBF, the higher stresses are developed at the lower levels and the curves have approximately a parabolic behaviour, however, not symmetric.

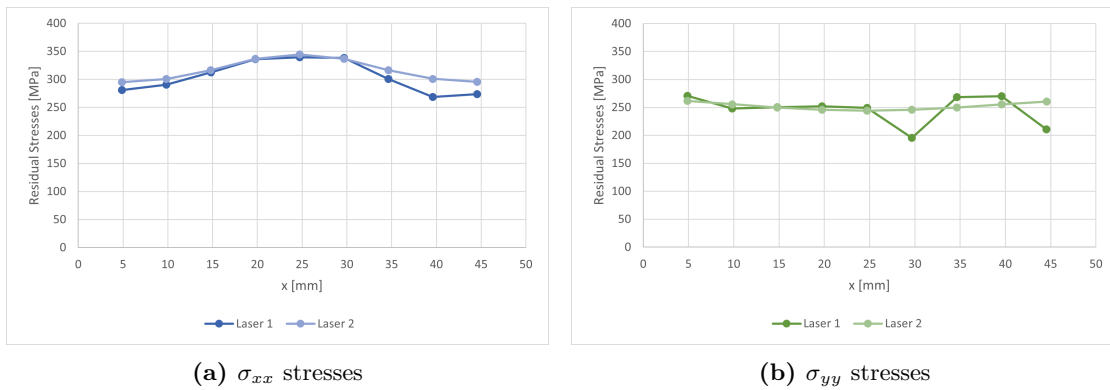


Figure 4.17 Evolution of the σ_{xx} and σ_{yy} stresses throughout the $z=20$ plane, extracted from the DED model.

Table 4.2 Residual stresses of the different scanning strategies at a reference point ($x=40$).

	Laser 1	Laser 2
σ_{xx} [MPa]	269	301
σ_{yy} [MPa]	270	256

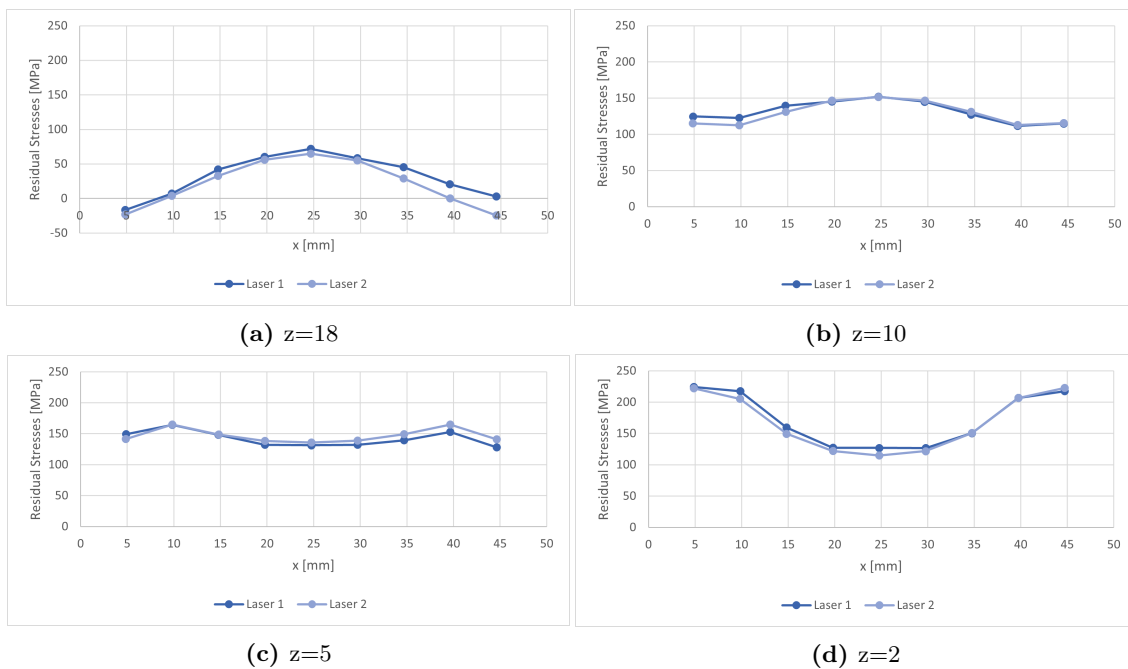


Figure 4.18 Evolution of σ_{xx} stresses throughout the $y=0$ plane, extracted from the DED model.

Figures 4.20, 4.21 and 4.22 represent the stress distribution of the DED model in the different directions, extracted from $y=5$ [mm] plane. Similarly to the PBF, σ_{zz} stresses are mostly compressive and convert into tensile stress in the top layers.

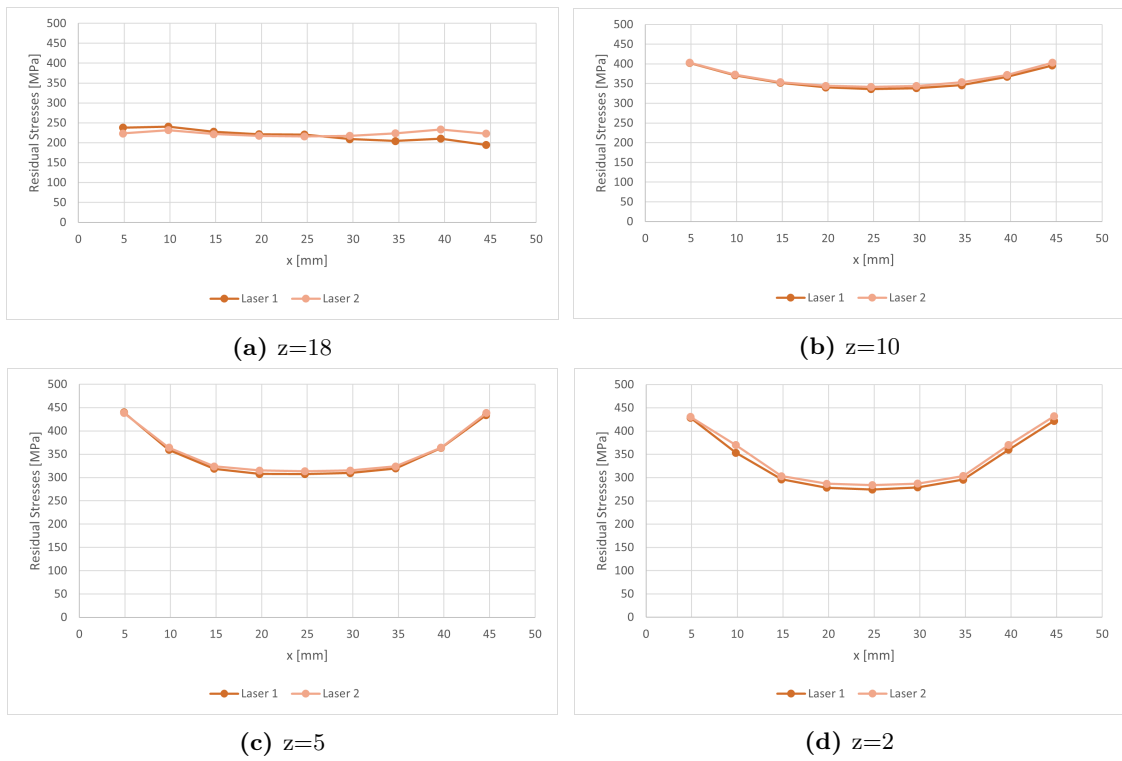


Figure 4.19 Evolution of σ_{zz} stresses throughout the $y=0$ plane, extracted from the DED model.

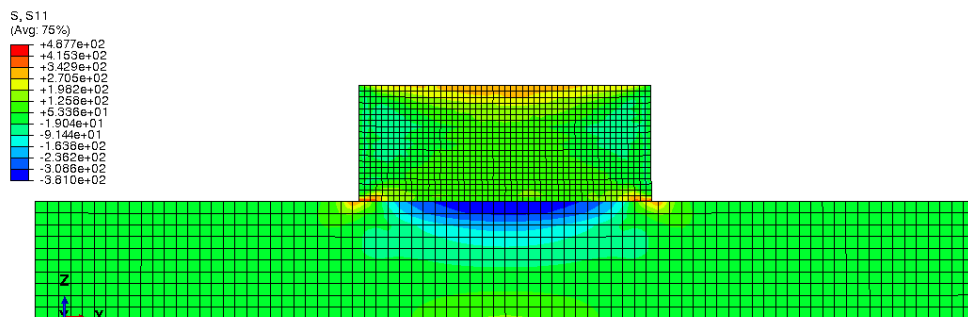


Figure 4.20 σ_{xx} stress distribution of the DED model, extracted from $y=5$ plane.

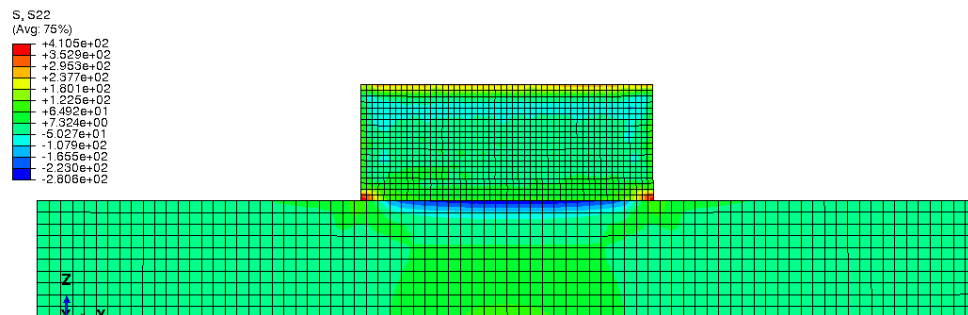


Figure 4.21 σ_{yy} stress distribution of the DED model, extracted from $y=5$ plane.

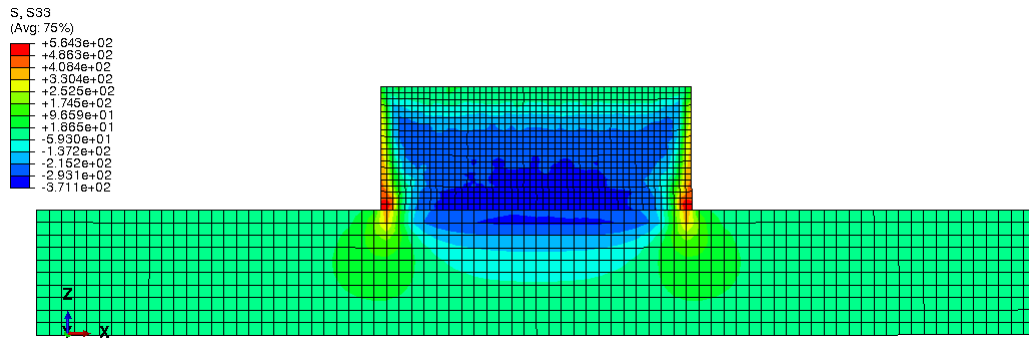


Figure 4.22 σ_{zz} stress distribution of the DED model, extracted from $y=5$ plane.

4.6 Comparison between the PBF and DED results

One of the objectives of this thesis is to establish and understand the difference between the residual stresses developed in the two most used metal AM processes. A direct comparison between the variable outputs was conducted and is represented in the following sets of figures.

For a similar reason as SLM, significant residual stresses could also be developed in a part processed by DED. Along the top plane, the PBF process appears to have a smoother behavior, unlike the DED process, which seems to have a rather irregular behaviour, as shown in Figure 4.23. The σ_{xx} stresses are higher in the PBF model, however, this process develops smaller stresses on the transverse direction.

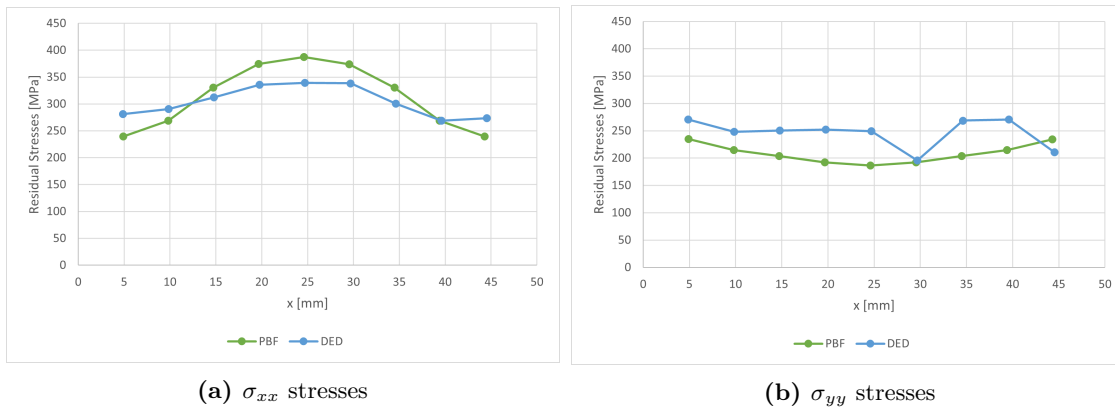


Figure 4.23 Comparison between the evolution of the σ_{xx} and σ_{yy} stresses throughout the $z=20$ plane (PBF and DED).

Throughout the front plane (Figures 4.24 and 4.25), DED presents significantly lower σ_{xx} stresses than PBF for all levels, however, regarding the σ_{zz} stresses, the behaviour is not the same. In the higher levels, the stresses in the build direction are identical for both processes, but for $z=5$ and $z=2$, the residual stresses developed in the PBF model are smaller.

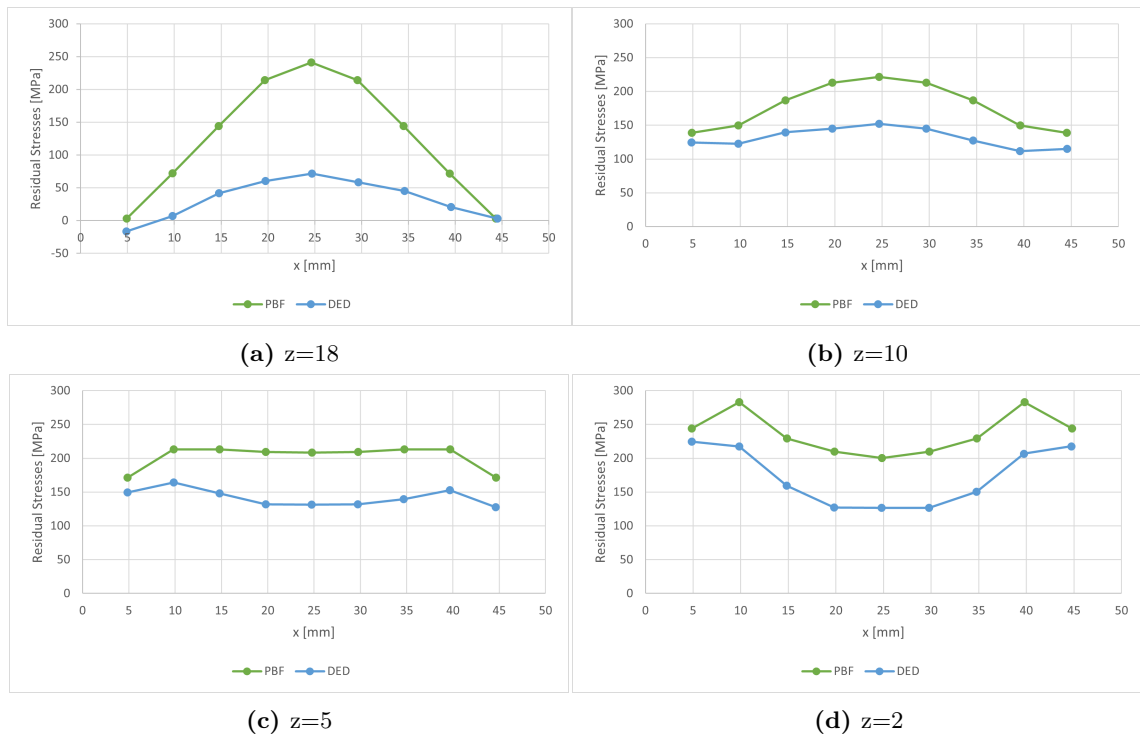


Figure 4.24 Comparison between the evolution of σ_{xx} stresses throughout the $y=0$ plane (PBF and DED).

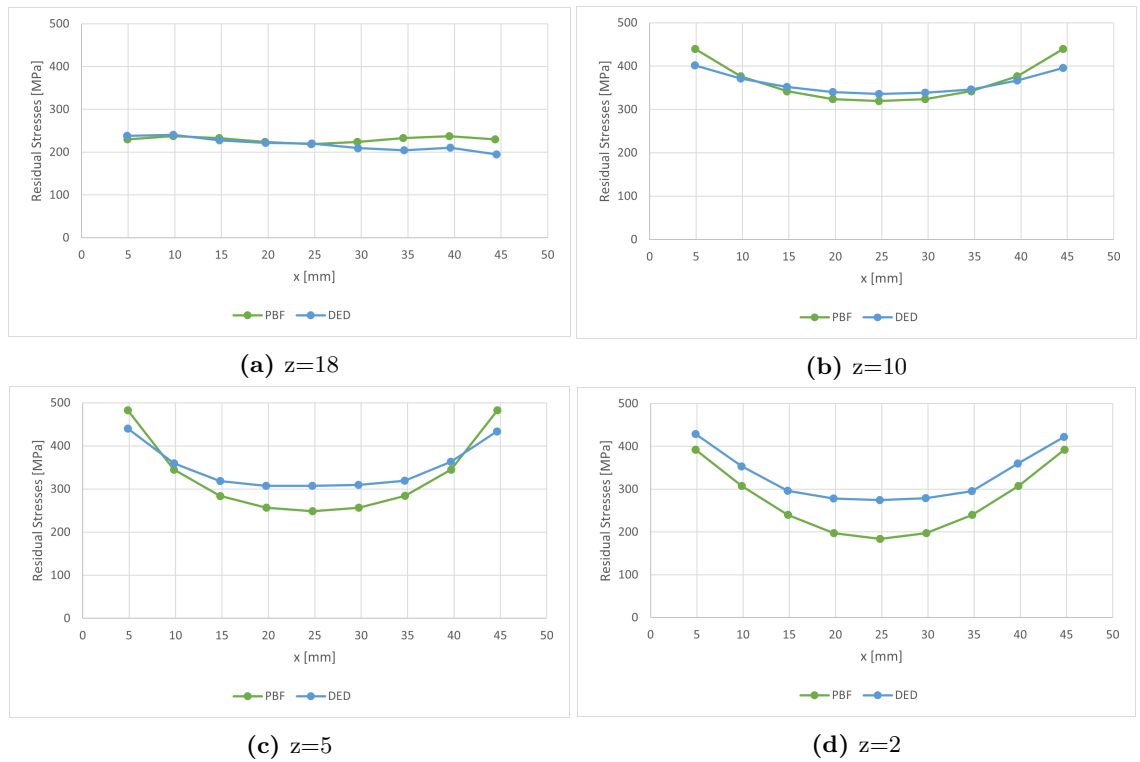


Figure 4.25 Comparison between the evolution of σ_{zz} stresses throughout the $y=0$ plane (PBF and DED).

Even though the two processes are widely used to obtain metal components, each one of them has specific parameters and applications, which makes it more difficult to directly compare both techniques. This analysis was made with the objective of comparing the residual stresses that are produced during these processes, when using the same part, substrate, material, laser parameters, boundary conditions, constraints, interactions and cooling conditions. Even so, the development of each numerical model is different and requires the input of specific variables, which makes this comparison to be almost impossible to reproduce experimentally.

4.7 Benchmark bridge

The benchmark bridge was used in the PBF model with the objective of exploring its behaviour when using more complex geometries. Initially, the sections elected to be analysed were the small prominences in the top plane, represented in Figure 4.26 ($z=12.5$). However, since these prominences have only a height of 0.5 [mm] and do not provide an accurate representation of the stresses in the bridge, it was necessary to examine different levels of the component to further understand the distribution of the residual stress in the x and y directions.

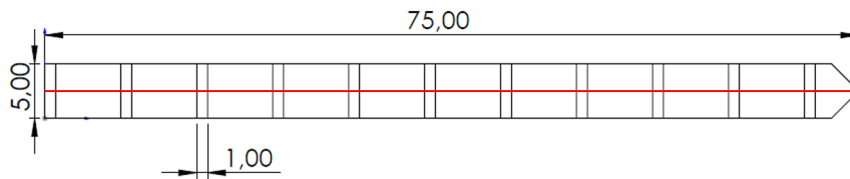


Figure 4.26 Representation of the analysed nodes on the the xy plane.

Figures 4.27 and 4.28 represent the longitudinal, σ_{xx} , and transverse, σ_{yy} , stresses of the initial analysis. The extreme irregularities (peaks) observed in both graphs correspond to the eleven prominences of the bridge, which indicates that these points have a different behaviour than the remaining part.

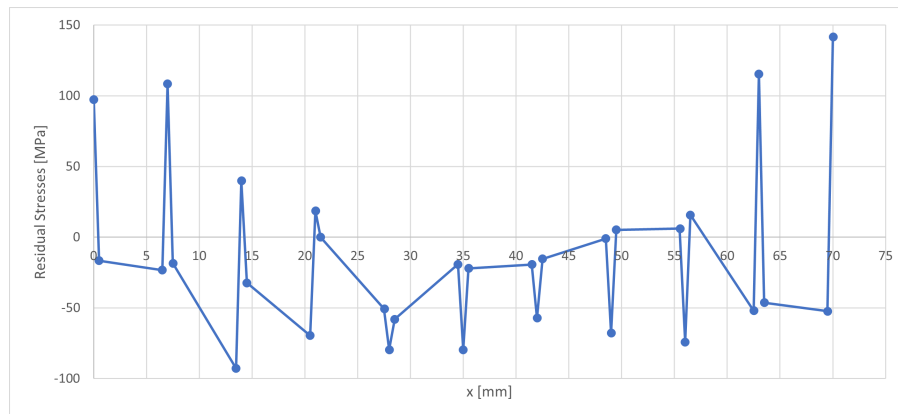


Figure 4.27 Evolution of σ_{xx} stresses on the bridge's prominences.

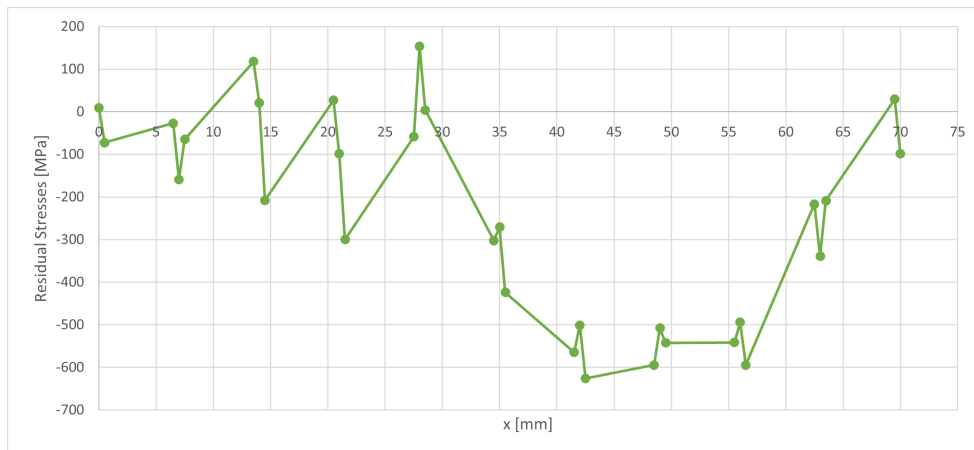


Figure 4.28 Evolution of σ_{yy} stresses on the bridge’s prominences.

Since the previous analysis did not provide an accurate representation of the bridge’s stress distribution, three other levels of the bridge were examined: $z=12$, $z=11.5$ and $z=10$. The results are presented in Figures 4.29 and 4.30 and it can be concluded that the σ_{xx} stresses vary a lot along the bridge’s length and height, however, compression stresses are mostly developed in the extremities of the bridge and tensile stresses are observed in the majority of the component. Additionally, the values for the lowest level are substantially smaller than on higher levels.

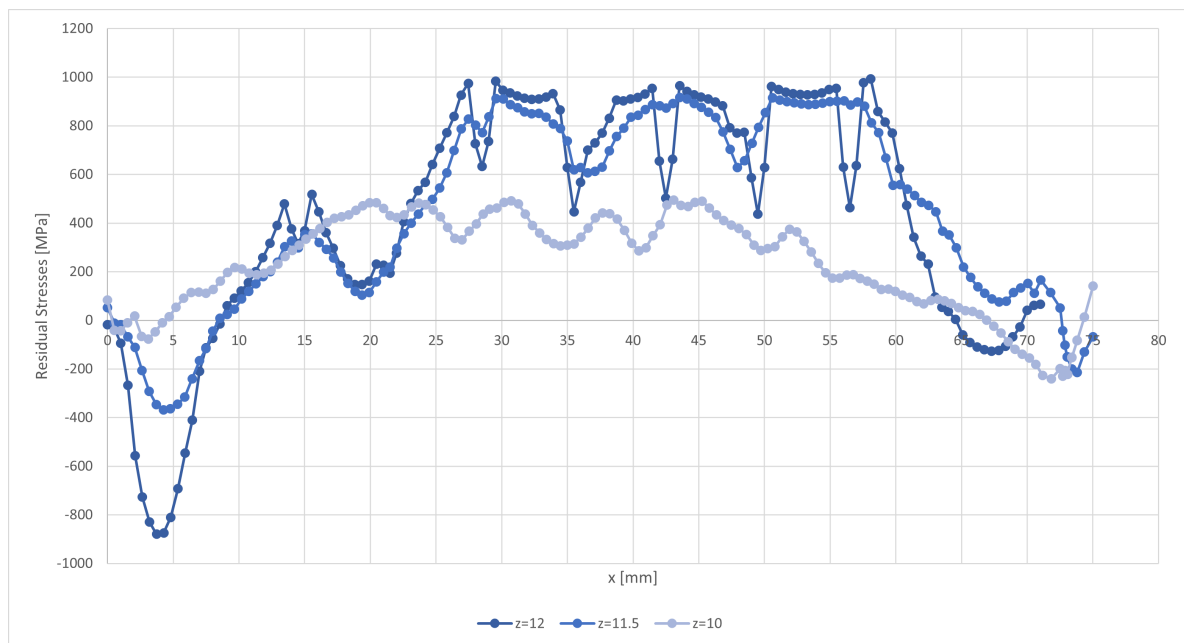


Figure 4.29 Evolution of σ_{xx} stresses on different levels.

Regarding the σ_{yy} stresses, for $z=12$ and $z=11.5$, multiple discrepancies on the values can be observed along the length, however, the majority of the part is subjected to tensile stresses. At the lowest level, the discrepancies are not as obvious and the stresses are

mostly compressive along the length. This analysis is an evidence that high and irregular stresses are developed in the bridge's printing process.

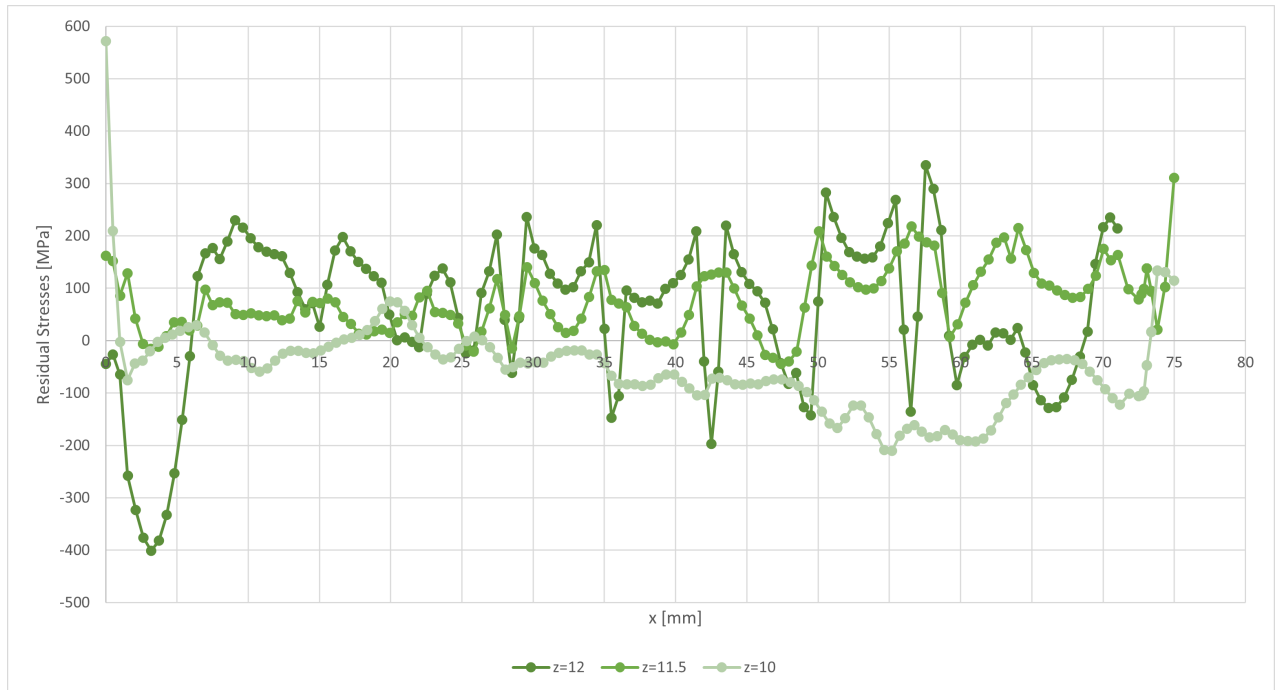


Figure 4.30 Evolution of σ_{yy} stresses on different levels.

Since the bridge has a more complex geometry, the stress distribution is very different from the prism's, which presented parabolic curves for nearly every variable. In the following figures, it is possible to observe the bridge's stress distributions in the different directions, extracted from plane $y=2.5$ [mm].

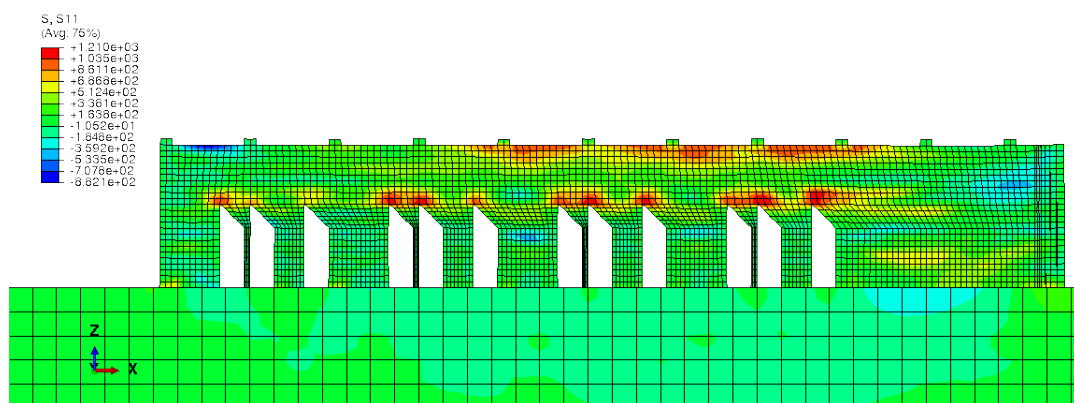


Figure 4.31 σ_{xx} distribution on the benchmark bridge, extracted from $y=2.5$ plane.

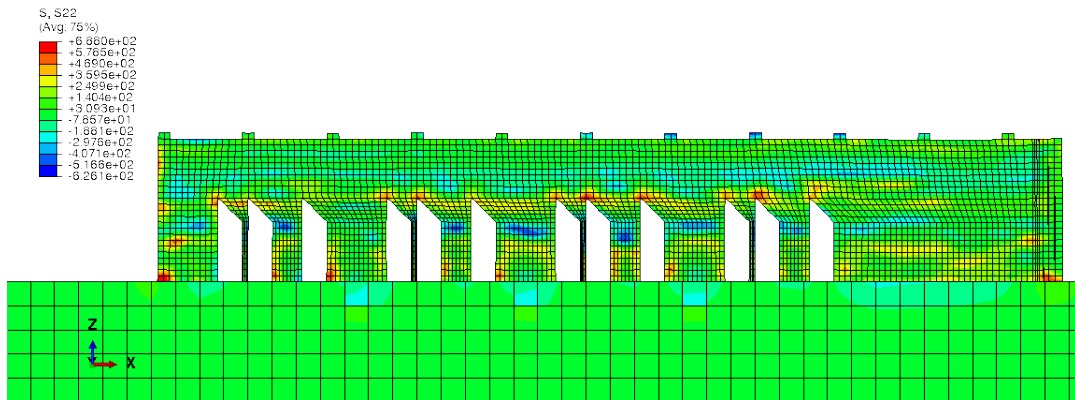


Figure 4.32 σ_{yy} distribution on the benchmark bridge, extracted from $y=2.5$ plane.

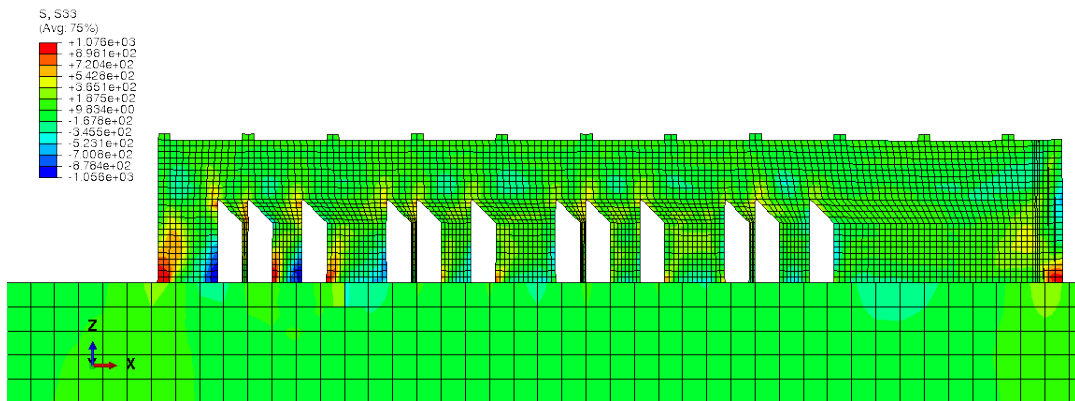


Figure 4.33 σ_{zz} distribution on the benchmark bridge, extracted from $y=2.5$ plane.

A study on the influence of the scanning strategy on the residual stresses was also conducted for this geometry, in order to understand if this variable has a higher impact on more complex geometries. Thus, another simulation was conducted using the prism's scanning strategy: repeating orientation every three layers (0° , 120° , 240°). The analysis was made at the same 3 levels as the previous strategy and the results are present in Figures 4.34 and 4.35.

In opposite to the prism's results, this analysis shows that there is indeed an obvious difference between the residual stresses developed by the two strategies, which leads to conclude that the geometry of the component is a crucial variable in these studies. Since the prism has a very simple geometry and the layers are equal to each other along all the printing process, the trajectory of the laser does not have a significant impact on the residual stresses. However, the bridge is a more complex geometry as it has legs with different lengths, sharp angles and very small volumes at the top. The building of the layers is conditioned by all these factors and, according to the results, the laser scanning strategy has a higher impact in this cases.

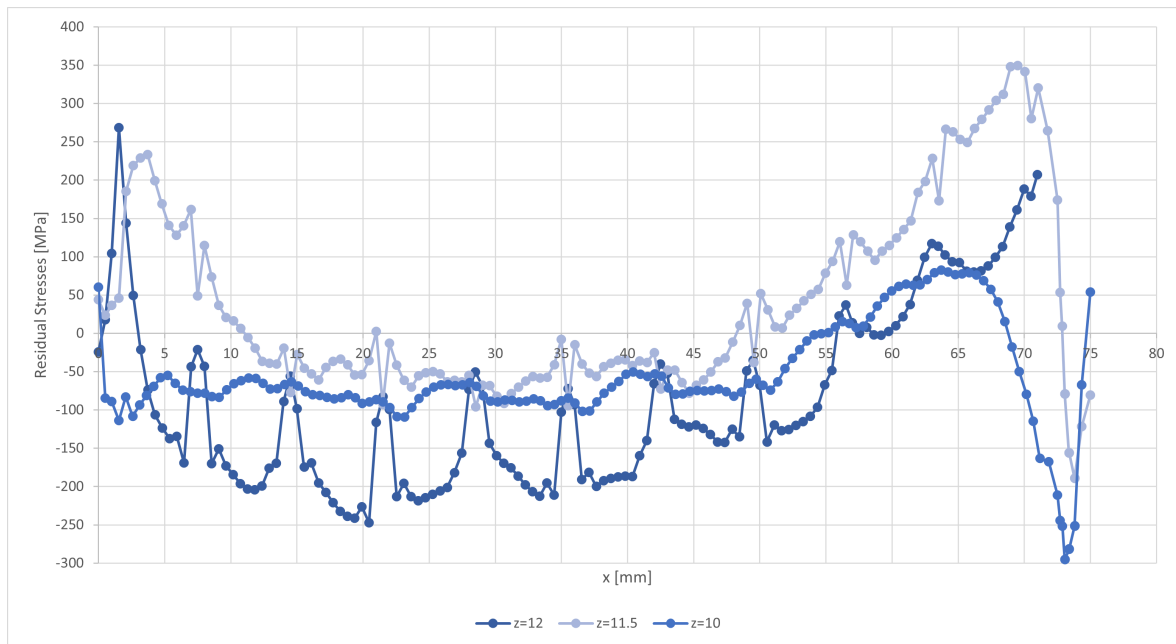


Figure 4.34 σ_{xx} distribution on the benchmark bridge using a different scanning strategy.

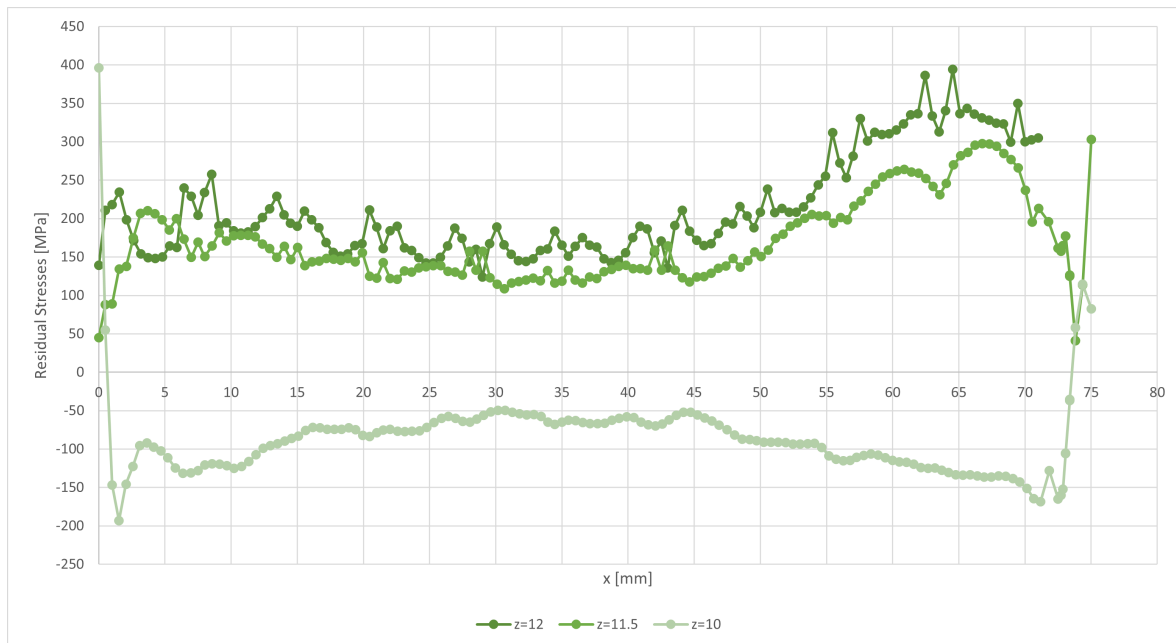


Figure 4.35 σ_{yy} distribution on the benchmark bridge using a different scanning strategy.

Nonetheless, the irregular stress distribution in a single layer is visible in both cases, specially in the higher levels. In the following figures, it is possible to observe the bridge's stress distributions in the different directions, extracted from plane $y=2.5$ [mm], using a scanning strategy based on repeating orientation every three layers, implying patterns with a 120° lag between them.

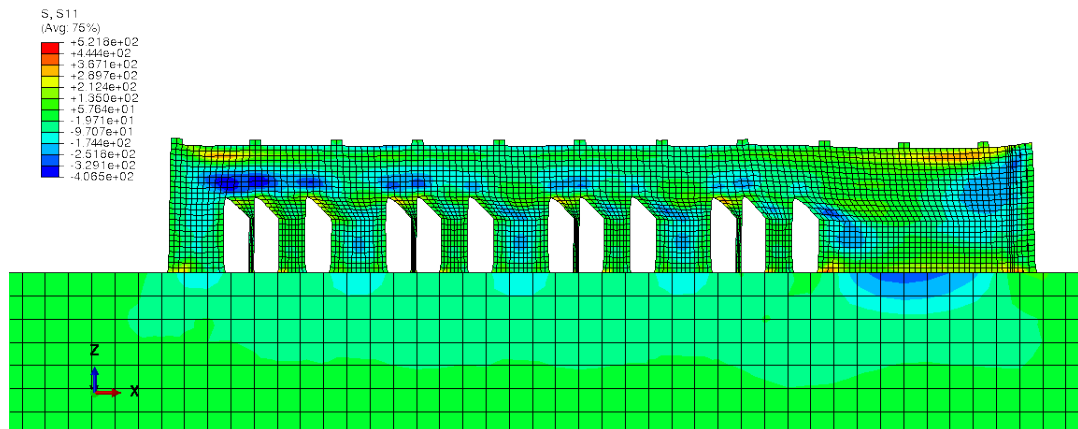


Figure 4.36 Bridge σ_{xx} stress distribution using a different scanning strategy, extracted from $y=2.5$ plane.

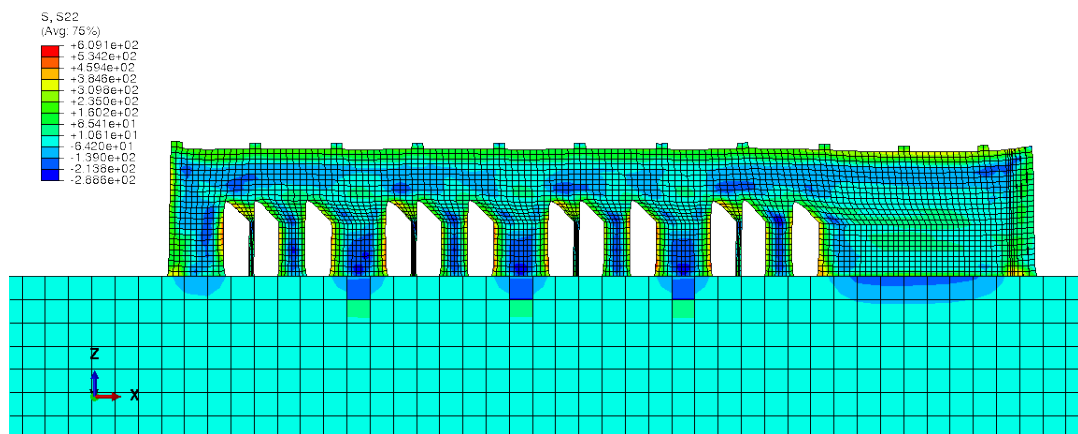


Figure 4.37 Bridge σ_{yy} stress distribution using a different scanning strategy, extracted from $y=2.5$ plane.

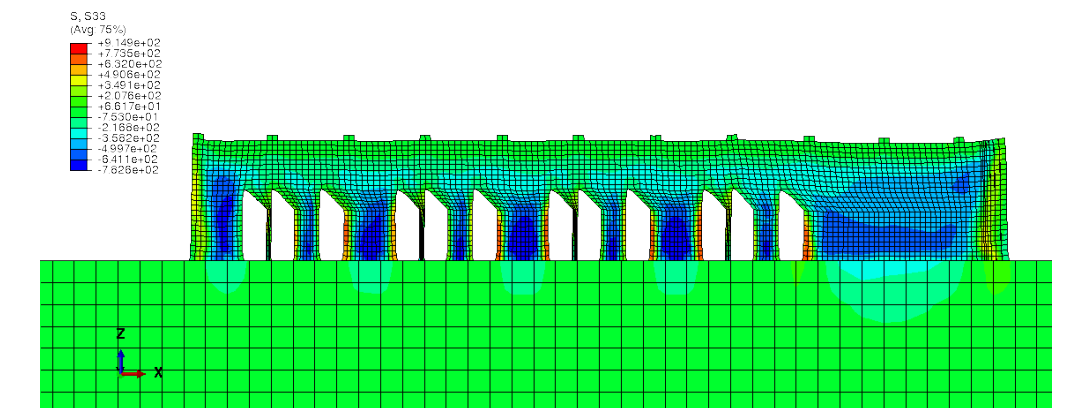


Figure 4.38 Bridge σ_{zz} stress distribution using a different scanning strategy, extracted from $y=2.5$ plane.

In the literature, the influence of the scanning strategy on the residual stresses is still widely studied, since the results of different analysis lead to different conclusions. In several studies, the results obtained for different strategies were significantly distinct, specially when using complex scanning patterns. The bridge's results are according to these cases, however, this effect it is most likely related to the geometry of the component, since this behaviour was not verified in the prism.

4.8 Comparison between the numerical and experimental results

This section of the study work focuses on the comparison between the numerical studies, whose goal was to simulate the manufacturing process of a physical sample as close as possible, to the experimental studies conducted by Center for Physics of the University of Coimbra, using X-Ray diffraction to measure residual stresses. The components used to conduct this experiment were the prism (not submitted to preheat temperature) and the benchmark bridge.

4.8.1 Prism

In the case of the prism, points from planes xy ($z=20$), xz ($y=0$) and yz ($x=0$) were measured and analysed. In the top plane, Figure 4.39, the numerical values for σ_{xx} are significantly higher than the ones measured experimentally, particularly for the midpoint, $x=25$. On the other hand, the σ_{yy} values for both studies are very similar, the numerical values being smaller in this case, and the maximum error between two values is of 25% at the midpoint.

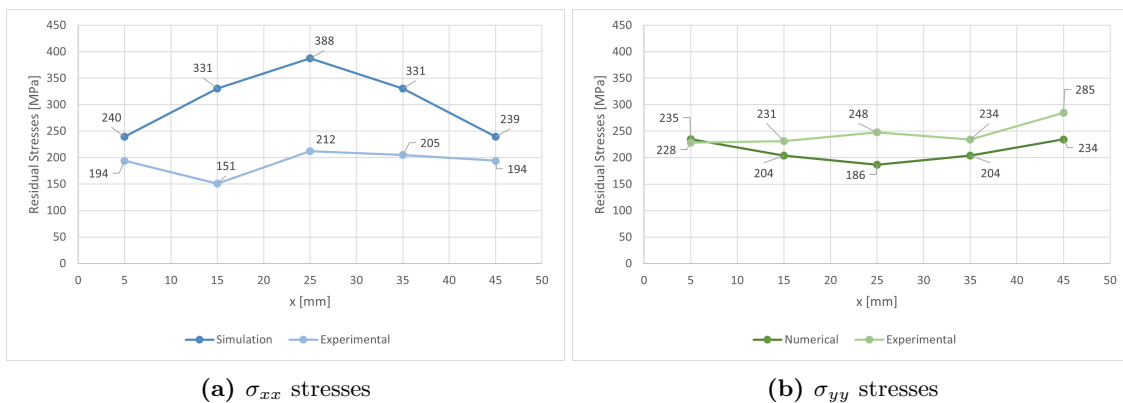


Figure 4.39 Evolution of the σ_{xx} and σ_{yy} stresses throughout the xy plane (Numerical *vs.* Experimental).

The points elected to study the residual stresses on the yz were along the z axis, for $y=5$. The results from Figure show, once again, similarities between the curves, despite the obvious difference between the values.

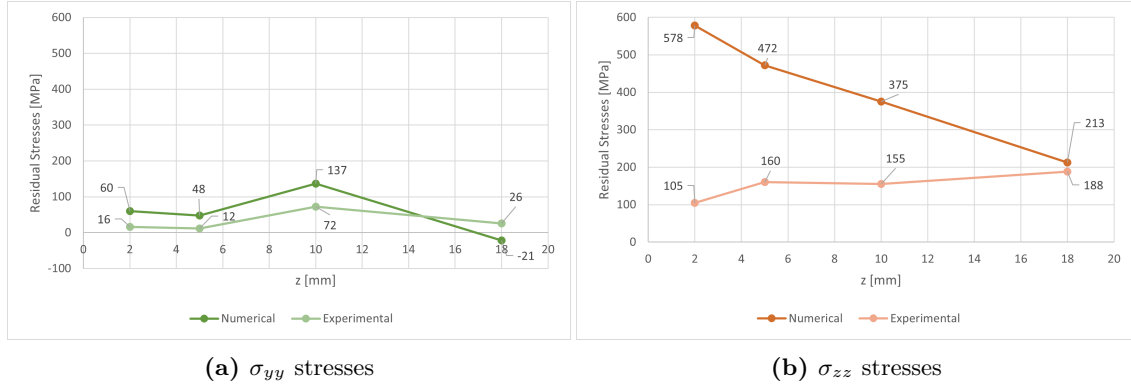


Figure 4.40 Evolution of the σ_{yy} and σ_{zz} stresses throughout the $x=0$ plane (Numerical *vs.* Experimental).

The numerical stress distribution of the prism for $x=25$ plane can also be observed in Figure 4.41, showing the evolution of the stresses along the height in the part's midsection.

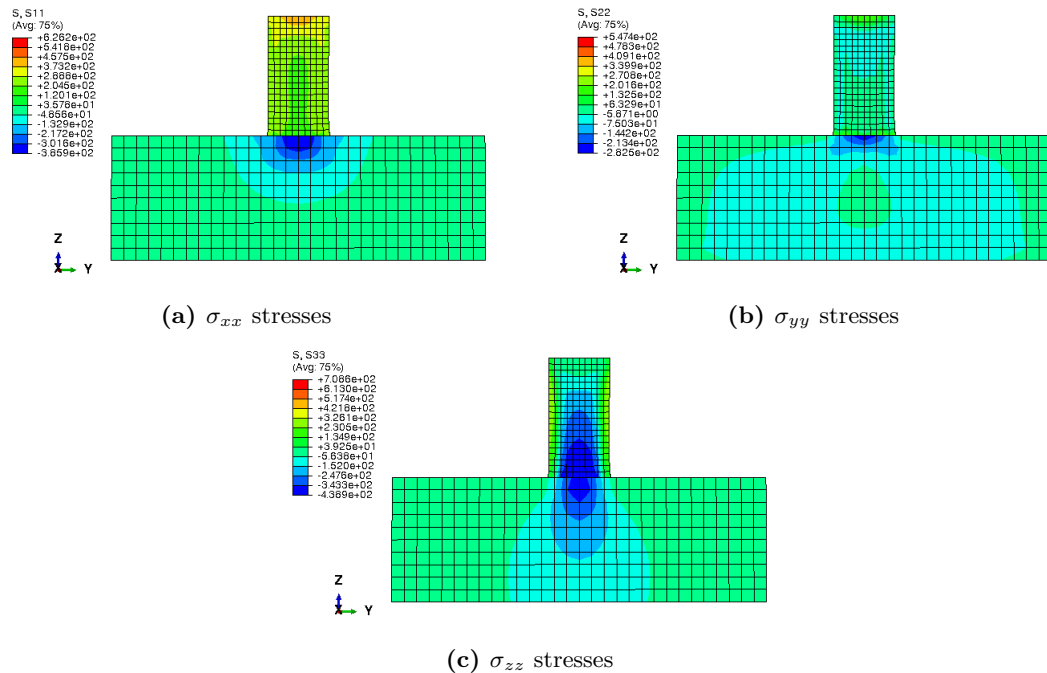


Figure 4.41 Stress distributions extracted from $x=25$ plane.

In the xz plane, σ_{xx} and σ_{zz} stresses were measured in four levels: $z=18$, $z=10$, $z=5$ and $z=2$. Regarding the σ_{xx} stresses presented in Figure 4.42, the numerical values are much higher than the experimental values, specially at the lower levels, where the experimental stresses are very small.

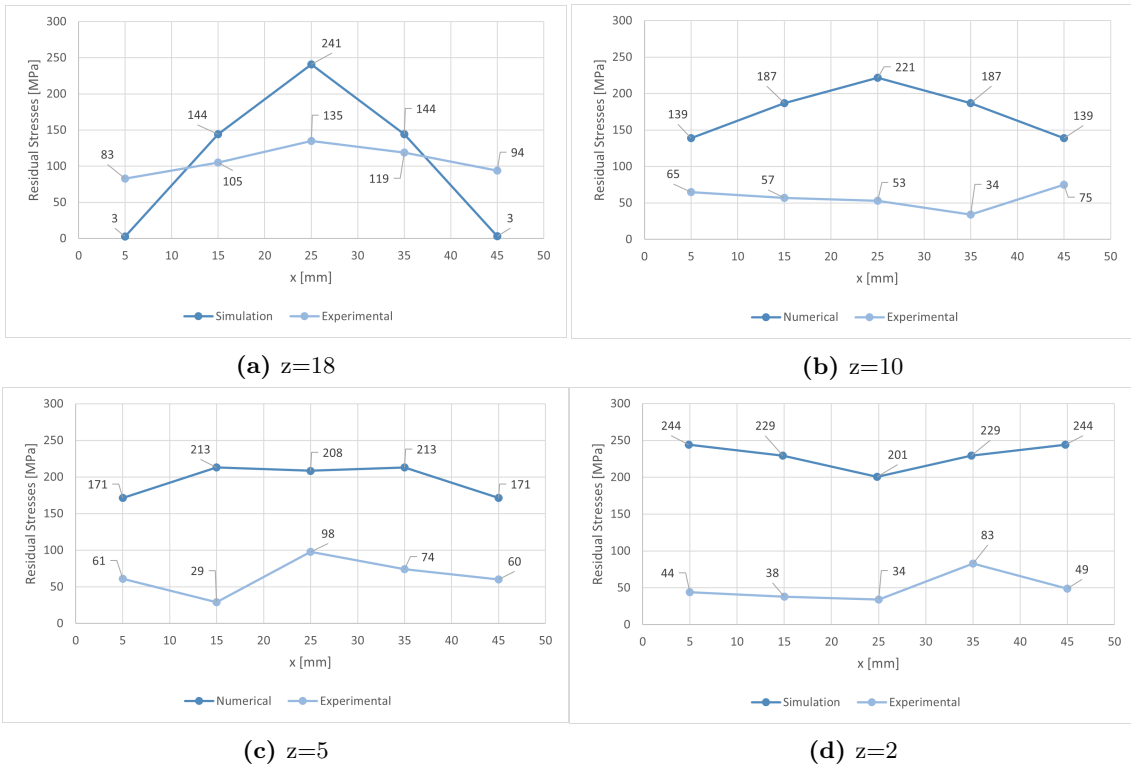


Figure 4.42 Evolution of σ_{xx} stresses throughout the xz plane (Numerical vs. Experimental).

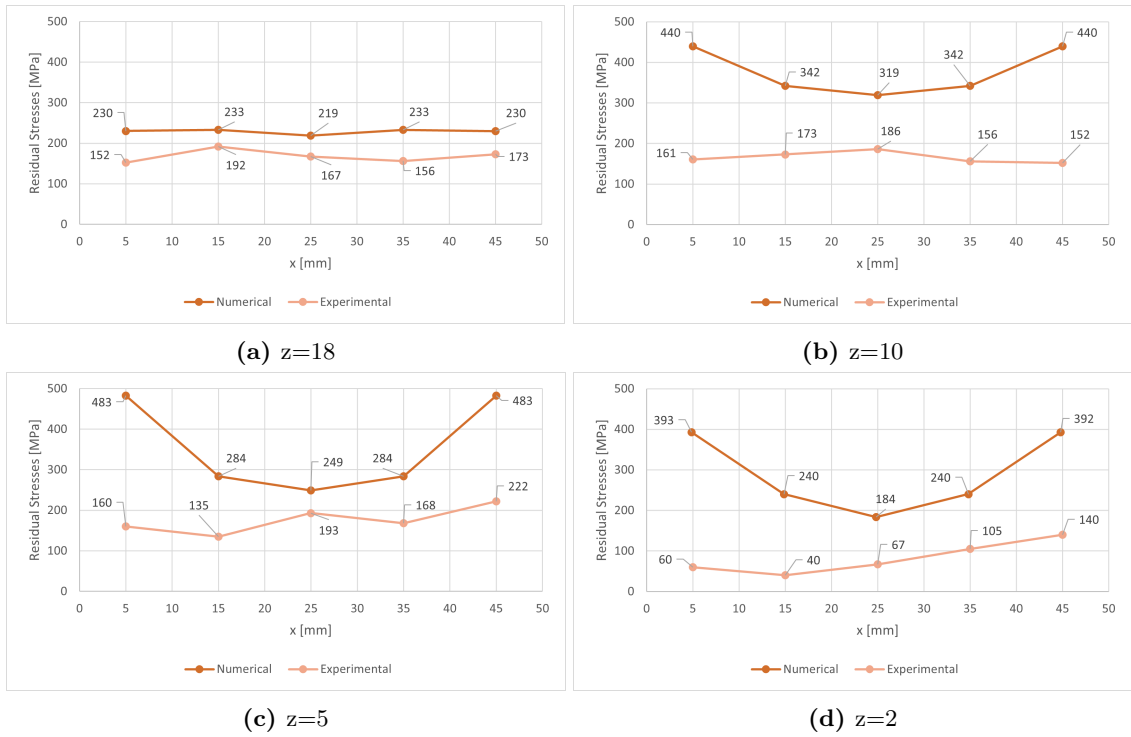


Figure 4.43 Evolution of σ_{zz} stresses throughout the xz plane (Numerical vs. Experimental).

On the other hand, the numerical and experimental curves for σ_{zz} stresses presented in

Figure 4.43 show some similarities in terms of evolution along the length, however, there are still discrepancies between the values, particularly at the prism's extremities.

It can be concluded that, despite the high percentage of error between the numerical and experimental studies in specific locations, the numerical study promotes a reasonable representation of the PBF process and of the residual stresses developed during the production of the part. It's worth mentioning the fact that the modeling of such a complex technique requires the consideration of a wide number of variables and particular conditions, which makes it very difficult to replicate the environment in which the experimental studies are conducted.

4.8.2 Benchmark bridges

The experimental study of the benchmark bridges consisted on the analysis of four parts produced by PBF: bridges A, B, C and D, as observed in Figure 4.44. All bridges are made of maraging steel and the machine settings used during the PBF process are presented in Table 3.2.

The objective of this experimental study was to examine the influence of the scanning strategy on the residual stresses developed on the bridge's prominences. Therefore, bridges C and D were printed using a continuous line strategy, in which even layers were scanned vertically (90°) and uneven layers were scanned horizontally (0°), and bridges A and B were printed using a striped method, which means that each layer was subdivided into multiple stripes that were constructed sequentially. In this case, even layers were horizontally scanned and uneven layers were scanned vertically, however, there were some errors in the scanning during the printing process of these bridges and, consequently, these results will not be analysed. Nonetheless, the experimental results for pairs (A and B) and (C and D) are identical, suggesting that the scanning strategies used had no significant affect on residual stresses in the areas analysed.

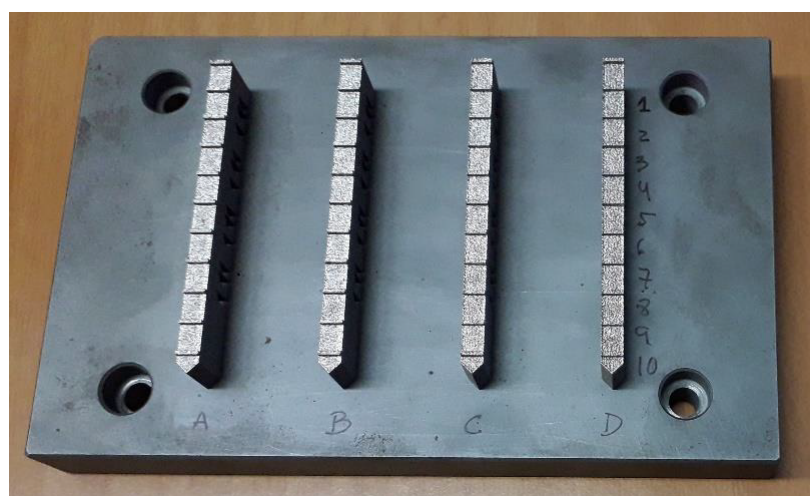


Figure 4.44 Printed benchmark bridges (November 2019).

Figures 4.45 and 4.46 represent the numerical results achieved for the first scanning strategy and the experimental data obtained for bridges C and D. The graphs show some convergence of the σ_{xx} results between points 4 and 8, however, there are some discrepancies on the values achieved for the bridge's extremities. On the other hand, regarding the transverse stresses, the numerical model does not promote an accurate representation of the stress evolution, since the experimental values are practically constant and the numerical results show some irregularities.

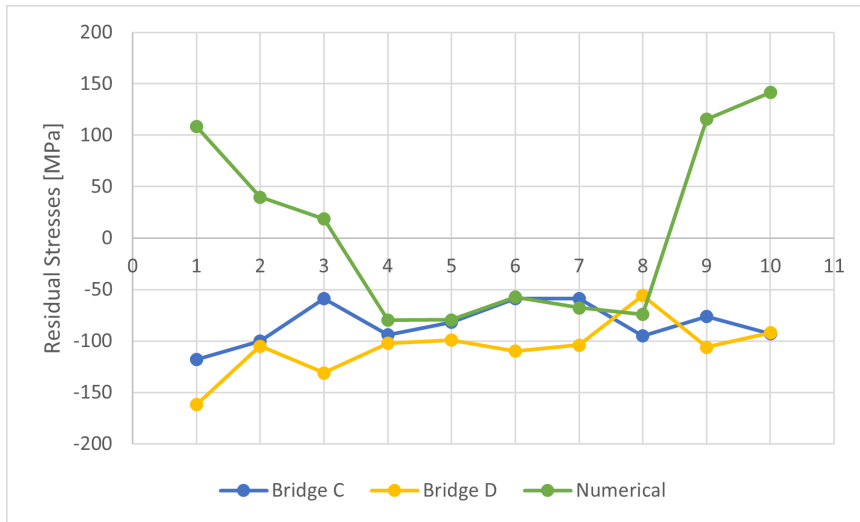


Figure 4.45 Evolution of σ_{xx} stresses on the bridges' prominences.

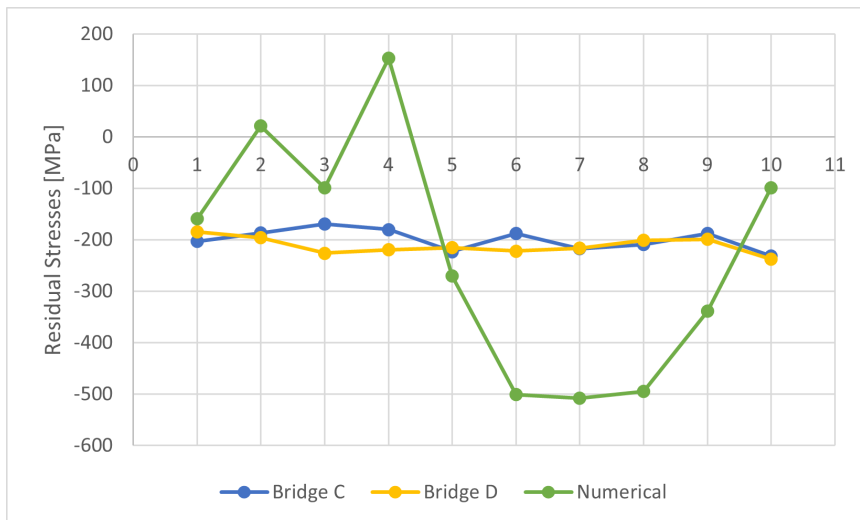


Figure 4.46 Evolution of σ_{yy} stresses on the bridges' prominences.

As previously mentioned, the prominences did not provide an accurate representation of the residual stresses' behaviour in the numerical model, since these regions have very small dimensions and the mesh size used in order to avoid excessive CPU times (0.5 [mm]) limits the number of elements that characterize these regions.

Despite the fact that the models do not converge in this specific locations, it was shown in previous analysis that the stress distribution in the bridge's top plane is very irregular, which makes it reasonable to assume that the models would present more similar behaviours at lower and stable levels, for example, for $z=10$ [mm].

4.9 Deflection analysis

This section explores the component's deflection after all of its legs have been removed by EDM (Electrical Discharge Machining), which means that the part is only connected to the baseplate through its larger section in the right extremity.

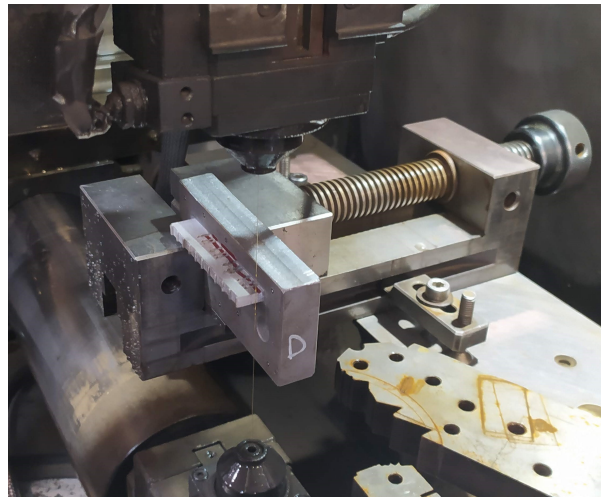


Figure 4.47 Wire-cut EDM process used on the bridges.

Experimental results were obtained through a Nikon Three-Axis Coordinate Measuring System with Renishaw PH10T-Plus Head, of spherical tip. The associated error to this procedure is 5 [μm]. The measuring points are presented in Figure 4.48.

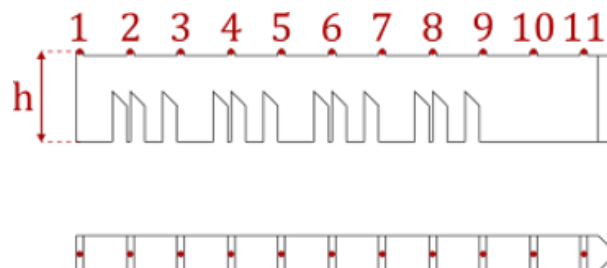


Figure 4.48 Measuring points of the experimental study.

Both the experimental and numerical results can be found in Figure 4.49. The numerical results were shown to be smaller, particularly in the initial point. The experimental values of bridges C and D are very similar to the numerical results, despite the 46% and 40% errors obtained for the first measuring point.

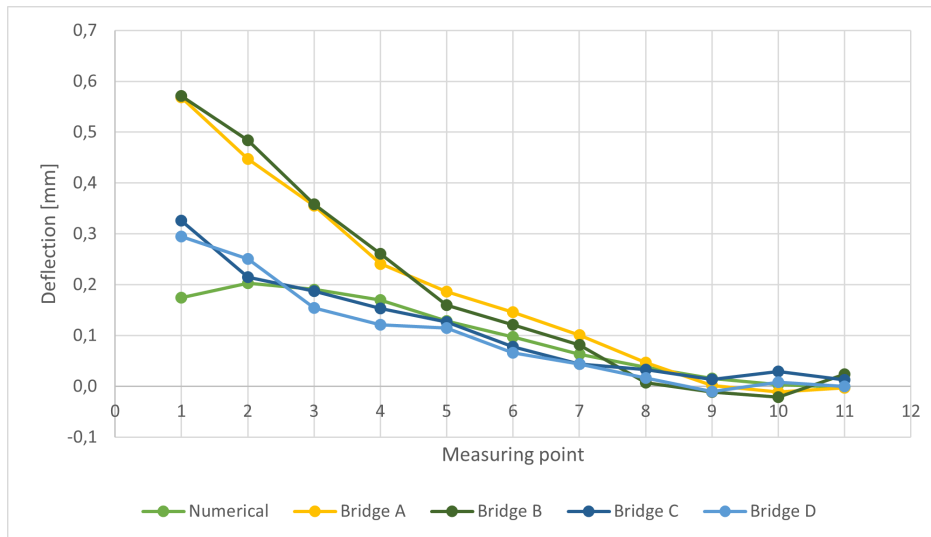


Figure 4.49 Experimental and numerical comparison between vertical deflection u_{zz} after leg removal

Figures 4.50 and 4.51 represent, respectively, the final deflection results achieved in Abaqus and experimentally. The volume towards the right extremity contracts and bends downwards due to the problem’s final boundary conditions. This contraction creates a negative displacement in the nodes on the component’s right side, which worsens the FEA results.

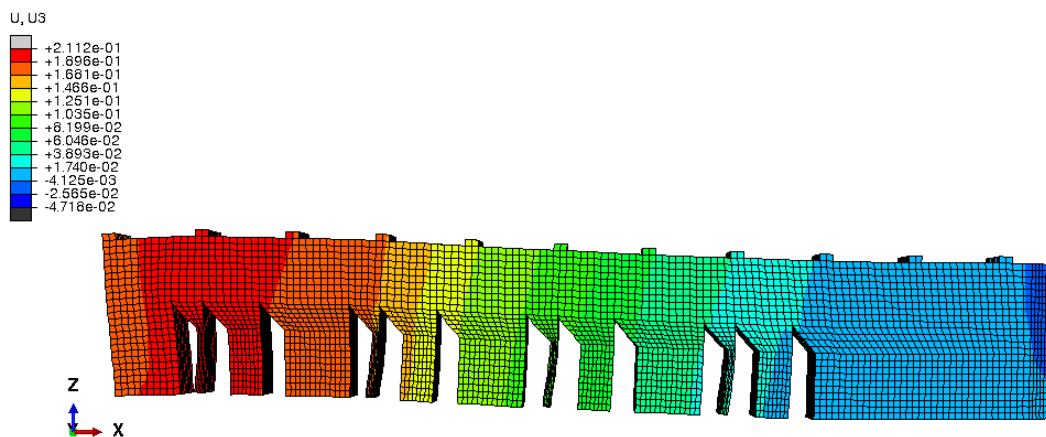


Figure 4.50 Displacement u_{zz} of the bridge with geometrical scale of 10.

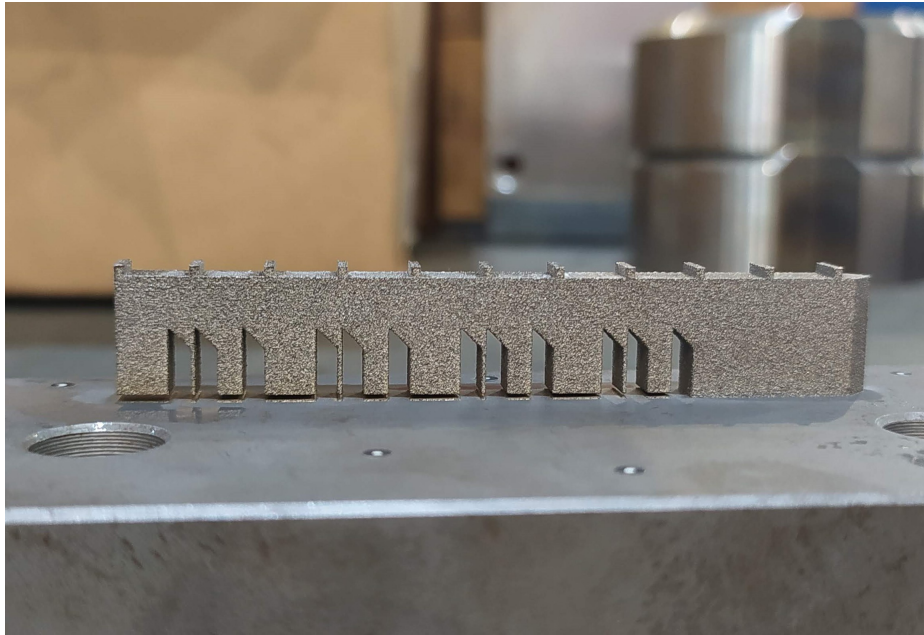


Figure 4.51 Bridge deflection after EDM process.

This page was intentionally left blank.

Chapter 5

Conclusions and Future Work

5.1 Conclusions

The fundamental purpose of this dissertation was to provide an overview of Abaqus as a software capable of estimating distortion and residual stresses developed during the modeling of AM processes. It was possible to explore the FEA formulation of AM processes conducting parametric and convergence studies on its input variables and, lastly, comparing the numerical results with experimental values.

The development of numerical models for two AM processes was a very slow procedure, as the high number of conditional variables led to the necessity to realize a lot of tests in the simulations in order to optimize the model as much as possible before thoroughly analysing the final results. A wide variety of parameters could have been analysed, however, due to the limited time available to complete this project, only three variables were submitted to parametric studies: mesh size, scanning strategy and preheat temperature. These studies were conducted with the objective of understanding the behaviour and evolution of the residual stresses in the components. The PBF model was further examined since an experimental study had been realized previously to this dissertation. This enables a direct comparison between numerical and experimental data, which is a valuable analysis to be conducted since it can lead to the optimization of numerical models that will be more and more used to predict a part's behaviour before the printing process. This ultimately will lead to a lower number of wasted parts due to mechanical defects and to reduction costs associated to AM processes, specially MAM, which is a very good accomplish in this field.

The main conclusions that were reached can be summarized in the following topics:

- One of the most important tools from Abaqus that was crucial to model AM processes is the progressive element activation, which is used to define the layer-by-layer deposition. A full element activation was implemented in both models. In the PBF model, each layer is entirely activated by the motion of the roller scanning the table. On the other hand, in the DED model, the scanning strategy can be observed during the activation of the layer's elements.

- Another fundamental parameter regarding the development of the numerical model was the definition of the moving heat source. This parameter simulates the laser-induced heating and was specified as "concentrated" for the PBF model and the Goldak distribution was used in the DED model.
- In the simpler geometry, the prism, Abaqus converged on the measured residual stress values, as the mesh was refined. As the mesh size decreases, the CPU time increases significantly, which led to the use of a mesh size of 1 [mm] for majority of the performed simulations.
- In the more complex geometry, the bridge, a mesh size of 0.5 [mm] was used, however, it did not provide very precise results. A more refined mesh should be applied to this component, as the smaller volumes of the bridge must be composed by multiple elements, in order to be better defined and provide valuable and accurate results.
- The different scanning strategies used in this dissertation did not influence the prism's residual stress results in the PBF model, however, this variable had an impact on the bridge's results, which led to believe that the influence of scanning strategy depends on the part's geometry.
- In the experimental studies and majority of simulations, the substrate's initial temperature was set at 25°C. It was shown in the numerical model that increasing the temperature of the baseplate reduces resulting residual stress magnitudes, which makes it reasonable to assume that the same behaviour would be observed in experimental studies.
- In general, the numerical models promoted higher values of residual stresses when compared to experimental data, which can be explained by the fact that AM processes are very complex and the modeling of these particular techniques (LPBF and DED) requires the use of a lot of variables and specific parameters that, if not well defined, can lead to errors of accuracy. Furthermore, the substrates' bottom surfaces were fixed in all degrees of freedom in the numerical models, however, in the experimental studies they were fixed at four points using screws, which can give some deformation capacity to the plate and reduce the stresses.
- The models do not take into consideration some important factors such as the presence of a powder bed in the PBF process and solid-state phase transformations present in the material, which can also explain the over prediction of the residual stress. Additionally, studies have shown that failing to properly account for the microstructural changes present in the deposited material has a substantial impact on simulated distortion results.

- The benchmark bridge's deflection after leg removal was simulated in Abaqus and the results were similar to experimental data, which is a good indirect validation of the overall residual stresses field estimation.

5.2 Future work

In order to optimize the numerical models and improve the results obtained in the duration of this project, some suggestions are provided:

- Study the results' convergence using more refined mesh sizes.
- Conduct an experimental study where the influence of the substrate's preheat temperature on the residual stresses is analysed.
- Study the influence of laser power and hatch space on the numerical model.
- Develop a condition that represents the powder bed in the PBF process and apply it to the existing model.
- Study the potential of a progressive stress relaxation model, which would require several tests to determine the appropriate rates of relaxation.
- Include microstructural changes present in the deposited material.
- Study the influence of using different materials for the same geometry.
- Modeling parts with larger dimensions.
- Choose different measuring points for the benchmark bridges.
- Provide experimental data of the DED process and establish a correlation with the numerical results.
- Compare the numerical results to other commercial softwares.
- Simulate and analyse the influence of heat treatments in the AM processes.

This page was intentionally left blank.

References

- [1] Bhaskar Dutta, Sudarsanam Babu, and Bradley Jared. Chapter 2 - additive manufacturing technology. In Bhaskar Dutta, Sudarsanam Babu, and Bradley Jared, editors, *Science, Technology and Applications of Metals in Additive Manufacturing*, Additive Manufacturing Materials and Technologies, pages 11–53. Elsevier, 2019.
- [2] D.N. Wasnik, G.K. Dey, V. Kain, and I. Samajdar. Precipitation stages in a 316l austenitic stainless steel. *Scripta Materialia*, 49(2):135–141, 2003.
- [3] Peter Pichler, Brian J Simonds, Jeffrey W Sowards, and Gernot Pottlacher. Measurements of thermophysical properties of solid and liquid nist srm 316l stainless steel. *Journal of Materials Science*, 55(9):4081–4093, 2020.
- [4] Jijin Xu, Philippe Gilles, Yonggang Duan, and Chun Yu. Temperature and residual stress simulations of the net single-bead-on-plate specimen using sysweld. *International Journal of Pressure Vessels and Piping*, s 99–100:51–60, 11 2012.
- [5] D. Umbrello, R. M'Saoubi, and J.C. Outeiro. The influence of johnson–cook material constants on finite element simulation of machining of aisi 316l steel. *International Journal of Machine Tools and Manufacture*, 47(3):462–470, 2007.
- [6] I. Polyzois. Finite element modeling of the behavior of armor materials under high strain rates and large strains. *Theory of Computing Systems Mathematical Systems Theory*, 2010.
- [7] Nils Keller. *Verzugsminderung bei selektiven Laserschmelzverfahren durch Multi-Skalen-Simulation*. PhD thesis, Universität Bremen, 2017.
- [8] Ashish Kalkal, Nabeel Ahmad, Gopinath Packirisamy, and Alexandr Vinogradov. *3D Printing in Medicine: Current Challenges and Potential Applications*, pages 1–22. 2019.
- [9] Jihong ZHU, Han ZHOU, Chuang WANG, Lu ZHOU, Shangqin YUAN, and Weihong ZHANG. A review of topology optimization for additive manufacturing: Status and challenges. *Chinese Journal of Aeronautics*, 34(1):91–110, 2021.
- [10] J.P.M. Pragana, R.F.V. Sampaio, I.M.F. Bragança, C.M.A. Silva, and P.A.F. Martins. Hybrid metal additive manufacturing: A state-of-the-art review. *Advances in Industrial and Manufacturing Engineering*, page 100032, 2021.
- [11] Tuan D. Ngo, Alireza Kashani, Gabriele Imbalzano, Kate T.Q. Nguyen, and David Hui. Additive manufacturing (3d printing): A review of materials, methods, applications and challenges. *Composites Part B: Engineering*, 143:172–196, 2018.

- [12] S.L. Sing, C.F. Tey, J.H.K. Tan, S. Huang, and Wai Yee Yeong. 2 - 3d printing of metals in rapid prototyping of biomaterials: Techniques in additive manufacturing. In Roger Narayan, editor, *Rapid Prototyping of Biomaterials (Second Edition)*, Woodhead Publishing Series in Biomaterials, pages 17–40. Woodhead Publishing, second edition edition, 2020.
- [13] Bhaskar Dutta, Sudarsanam Babu, and Bradley Jared. Chapter 8 - qualification for metal additive manufacturing. In Bhaskar Dutta, Sudarsanam Babu, and Bradley Jared, editors, *Science, Technology and Applications of Metals in Additive Manufacturing*, Additive Manufacturing Materials and Technologies, pages 245–307. Elsevier, 2019.
- [14] Bhaskar Dutta, Sudarsanam Babu, and Bradley Jared. Chapter 1 - metal additive manufacturing. In Bhaskar Dutta, Sudarsanam Babu, and Bradley Jared, editors, *Science, Technology and Applications of Metals in Additive Manufacturing*, Additive Manufacturing Materials and Technologies, pages 1–10. Elsevier, 2019.
- [15] Ian Gibson, David Rosen, and Brent Stucker. Additive manufacturing technologies: 3d printing, rapid prototyping, and direct digital manufacturing, second edition, 01 2015.
- [16] Yang Gao, Borui Li, Wei Wang, Wenyao Xu, Chi Zhou, and Zhanpeng Jin. Watching and safeguarding your 3d printer: Online process monitoring against cyber-physical attacks. *Proceedings of the ACM on Interactive, Mobile, Wearable and Ubiquitous Technologies*, 2:1–27, 2018.
- [17] John J. Lewandowski and Mohsen Seifi. Metal additive manufacturing: A review of mechanical properties. *Annual Review of Materials Research*, 46(1):151–186, 2016.
- [18] S. Sun, M. Brandt, and M. Easton. 2 - powder bed fusion processes: An overview. In Milan Brandt, editor, *Laser Additive Manufacturing*, Woodhead Publishing Series in Electronic and Optical Materials, pages 55–77. Woodhead Publishing, 2017.
- [19] Adrita Dass and Atieh Moridi. State of the art in directed energy deposition: from additive manufacturing to materials design. *Coatings*, 9(7):418, 2019.
- [20] Jamison L. Bartlett and Xiaodong Li. An overview of residual stresses in metal powder bed fusion. *Additive Manufacturing*, 27:131–149, 2019.
- [21] C. Li, Z.Y. Liu, X.Y. Fang, and Y.B. Guo. Residual stress in metal additive manufacturing. *Procedia CIRP*, 71:348–353, 2018. 4th CIRP Conference on Surface Integrity (CSI 2018).
- [22] Lin Cheng and Albert To. Part-scale build orientation optimization for minimizing residual stress and support volume for metal additive manufacturing: Theory and experimental validation. *Computer-Aided Design*, 113:1–23, 2019.
- [23] Michael P Sealy, Gurucharan Madireddy, Robert E Williams, Prahalada Rao, and Maziar Toursangsaraki. Hybrid processes in additive manufacturing. *Journal of manufacturing Science and Engineering*, 140(6):1–13, 2018.
- [24] LASERTEC DED: Additive Manufacturing by powder nozzle. <https://en.dmgmori.com/products/machines/additive-manufacturing/powder-nozzle>. 2021-03-20.

-
- [25] Tuan D. Ngo, Alireza Kashani, Gabriele Imbalzano, Kate T.Q. Nguyen, and David Hui. Additive manufacturing (3d printing): A review of materials, methods, applications and challenges. *Composites Part B: Engineering*, 143:172–196, 2018.
- [26] AMPOWER. *AMPOWER Report 2020 Metal Additive Manufacturing Management Summary*.
- [27] EOS 3D Printing Metal Materials. <https://www.eos.info/en/additive-manufacturing/3d-printing-metal/dmls-metal-materials>. 2021-03-10.
- [28] Kim Vanmeensel, Karel Lietaert, Bey Vrancken, Sasan Dadbakhsh, Xiaopeng Li, Jean-Pierre Kruth, Pavel Krakhmalev, Igor Yadroitsev, and Jan Van Humbeeck. 8 - additively manufactured metals for medical applications. In Jing Zhang and Yeon-Gil Jung, editors, *Additive Manufacturing*, pages 261–309. Butterworth-Heinemann, 2018.
- [29] SLM Solutions. Slm medical and dental applications: Metal additive manufacturing solutions for healthcare. Brochure, 2020. 2021-03-09.
- [30] Joaquim Minguella-Canela, Sergio Morales Planas, and María Antonia De los Santos-López. Slm manufacturing redesign of cooling inserts for high production steel moulds and benchmarking with other industrial additive manufacturing strategies. *Materials*, 13(21), 2020.
- [31] Martin Leary. Chapter 11 - powder bed fusion. In Martin Leary, editor, *Design for Additive Manufacturing*, Additive Manufacturing Materials and Technologies, pages 295–319. Elsevier, 2020.
- [32] SLM Solutions. Case study: Tooling inserts with conformal cooling. Brochure, 2019. 2021-03-09.
- [33] SLM Solutions. Case study: Die-casting mold insert with conformal cooling. Brochure, 2019. 2021-03-09.
- [34] Eugenio Oñate. *Structural Analysis with the Finite Element Method. Linear Statics. Vol. 1: Basis and Solids*. Springer Netherlands, 2009.
- [35] O.C. Zienkiewicz, R. Taylor, and J.Z. Zhu. The standard discrete system and origins of the finite element method. In O.C. Zienkiewicz R.L. Taylor and J.Z. Zhu, editors, *The Finite Element Method Set (Sixth Edition)*, chapter 1, pages 1–18. Butterworth-Heinemann, Oxford, 2005.
- [36] Erik Robert Denlinger. *Thermo-mechanical model development and experimental validation for metallic parts in additive manufacturing*. PhD thesis, Mechanical Engineering Graduate Program, PennState, 2015.
- [37] Xu Song, Stefanie Feih, Wei Zhai, Chen-Nan Sun, Feng Li, Raj Maiti, Jun Wei, Yangzhan Yang, Victor Oancea, Leon Romano Brandt, and Alexander M. Korsunsky. Advances in additive manufacturing process simulation: Residual stresses and distortion predictions in complex metallic components. *Materials Design*, 193:108779, 2020.

- [38] L. Costa, R. Vilar, T. Reti, and A.M. Deus. Rapid tooling by laser powder deposition: Process simulation using finite element analysis. *Acta Materialia*, 53(14):3987–3999, 2005.
- [39] Farshid Hajjalizadeh and Ayhan Ince. Short review on modeling approaches for metal additive manufacturing process. *Material Design & Processing Communications*, 2(2):e56, 2020.
- [40] Qingcheng Yang, Pu Zhang, Lin Cheng, Zheng Min, Minking Chyu, and Albert C. To. Finite element modeling and validation of thermomechanical behavior of ti-6al-4v in directed energy deposition additive manufacturing. *Additive Manufacturing*, 12:169–177, 2016.
- [41] Ruishan Xie, Gaoqiang Chen, Yue Zhao, Shuai Zhang, Wentao Yan, Xin Lin, and Qingyu Shi. In-situ observation and numerical simulation on the transient strain and distortion prediction during additive manufacturing. *Journal of Manufacturing Processes*, 38:494–501, 2019.
- [42] Thermomechanical analysis of powder bed-type additive manufacturing processes using the trajectory-based method. <https://help.3ds.com/2020/english/DSSIMULIA-Established/SIMACAEANLRefMap/simaanl-c-amspecialpurpose-powderbed.htm?ContextScope=allsimaanl-c-amspecialpurpose-powderbed>. 2021-06-07.
- [43] Yukio Ueda, You Chul Kim, and Min Gang Yuan. A predicting method of welding residual stress using source of residual stress (report i): characteristics of inherent strain (source of residual stress)(mechanics, strength & structural design). *Transactions of JWRI*, 18(1):135–141, 1989.
- [44] Thomas Mayer, Gabriel Brändle, Andreas Schönenberger, and Robert Eberlein. Simulation and validation of residual deformations in additive manufacturing of metal parts. *Heliyon*, 6(5):e03987, 2020.
- [45] Farshid Hajjalizadeh and Ayhan Ince. Finite element-based numerical modeling framework for additive manufacturing process. *Material Design & Processing Communications*, 1(1):e28, 2019.
- [46] T. Ales. An integrated model for the probabilistic prediction of yield strength in electron-beam additively manufactured ti-6al-4v. *Theory of Computing Systems Mathematical Systems Theory*, page 15, 2018.
- [47] Panagiotis Michaleris. Modeling metal deposition in heat transfer analyses of additive manufacturing processes. *Finite Elements in Analysis and Design*, 86:51–60, 2014.
- [48] Thermomechanical simulation of additive manufacturing processes. https://help.3ds.com/2020/english/DSSIMULIA_Established/SIMACAEANLRefMap/simaanl-c-amthermomechanical.htm?ContextScope=allsimaanl-c-amthermomechanical. 2021-05-19.
- [49] Michael Gouge and Pan Michaleris. *Thermo-mechanical modeling of additive manufacturing*. Butterworth-Heinemann, 2017.

- [50] Toolpath-mesh intersection module. https://help.3ds.com/2020/english/DSSIMULIA_Established/SIMACAEANLRefMap/simaanl-m-AMToolpathMeshIntersect-sb.htm?ContextScope=allid=ee967f4d42b34bb2a89c5a5d4e9257b6Pg0. 2021-03-21.
- [51] Eigenstrain-based simulation of additive manufacturing processes. https://help.3ds.com/2020/english/DSSIMULIA_Established/SIMACAEANLRefMap/simaanl-c-ameigenstrainbased.htm?ContextScope=allid=1af9097b432e41f2a1269684975ca4efPg0. 2021-05-19.
- [52] NIST. Amb2018-01 description, 2018.
- [53] Y.B. Lei, Z.B. Wang, B. Zhang, Z.P. Luo, J. Lu, and K. Lu. Enhanced mechanical properties and corrosion resistance of 316l stainless steel by pre-forming a gradient nanostructured surface layer and annealing. *Acta Materialia*, 208:116773, 2021.
- [54] Nabendu Ghosh, Pradip Kumar Pal, and Goutam Nandi. Gmaw dissimilar welding of aisi 409 ferritic stainless steel to aisi 316l austenitic stainless steel by using aisi 308 filler wire. *Engineering Science and Technology, an International Journal*, 20(4):1334–1341, 2017.
- [55] Ye Wang, Zhenghao Liu, Yuzhao Zhou, Xiaoshan Yang, Jingang Tang, Xue Liu, Jinfeng Li, and Guomin Le. Microstructure and mechanical properties of tin particles strengthened 316l steel prepared by laser melting deposition process. *Materials Science and Engineering: A*, 814:141220, 2021.
- [56] Latent heat. https://help.3ds.com/2020/english/dssimulia_established/SIMACAE_MATRefMap/simamat-c-latentheat.htm?ContextScope=allsimamat-c-latentheat. 2021-06-07.
- [57] Tiago Silva. *Machinability of Maraging Steel Manufactured by Laser Powder Bed Fusion*. PhD thesis, FEUP, 2021.
- [58] Wei Sha and Zhanli Guo. 1 - introduction to maraging steels. In Wei Sha and Zhanli Guo, editors, *Maraging Steels*, Woodhead Publishing Series in Metals and Surface Engineering, pages 1–16. Woodhead Publishing, 2009.
- [59] Eric A. Jäggle, Zhendong Sheng, Philipp Kürnsteiner, Sörn Ocylok, Andreas Weisheit, and Dierk Raabe. Comparison of maraging steel micro- and nanostructure produced conventionally and by laser additive manufacturing. *Materials*, 10(1):8, 2017.
- [60] Naoki Takata, Ryoya Nishida, Asuka Suzuki, Makoto Kobashi, and Masaki Kato. Crystallographic features of microstructure in maraging steel fabricated by selective laser melting. *Metals*, 8(6):440, 2018.
- [61] About additive manufacturing process simulation. https://help.3ds.com/2020/english/DSSIMULIA_Established/SIMACAEANLRefMap/simaanl-c-amabout.htm?ContextScope=allsimaanl-c-amabout-special. 2021-06-08.
- [62] Sequential thermomechanical analysis of a laser powder bed fusion build. https://help.3ds.com/2020/english/dssimulia_established/simacaexarefmap/simae_xa-c-amlaserpowderbedfusion.htm?contextscope=all. 2021-06-08.

- [63] Sequential thermomechanical analysis of a directed energy deposition build. https://help.3ds.com/2020/english/dssimulia_established/simacaexarefmap/simae_xa-c-amdirectedenergydeposition.htm?contextscope=all. 2021-06-08.
- [64] Thermomechanical analysis of FDM- and LDED-type additive manufacturing processes. https://help.3ds.com/2020/english/DSSIMULIA_Established/SIMACAEANLRefMap/simaanl-c-amspecialpurpose-lded.htm?ContextScope=allsimaanl-c-amspecialpurpose-lded. 2021-06-08.
- [65] H. Pommier, E.P. Busso, T.F. Morgeneyer, and A. Pineau. Local approach to stress relaxation cracking in a aisi 316l-type austenitic stainless steel: Tomography damage quantification and fe simulations. *Engineering Fracture Mechanics*, 183:170–179, 2017.
- [66] G. Gurewitz, N. Atzmon, and A. Rosen. Creep and stress relaxation in 18% ni (250) maraging steel. *Metals Technology*, 4(1):62–65, 1977.
- [67] Progressive element activation. https://help.3ds.com/2020/english/DSSIMULIA_Established/SIMACAEANLRefMap/simaanl-c-elemactivation.htm?ContextScope=allsimaanl-c-elemactivation. 2021-06-07.
- [68] Gunther Mohr, Susanna Nowakowski, Simon J. Altenburg, Christiane Maierhofer, and Kai Hilgenberg. Experimental determination of the emissivity of powder layers and bulk material in laser powder bed fusion using infrared thermography and thermocouples. *Metals*, 10(11):26, 2020.
- [69] J. Robinson, I. Ashton, P. Fox, E. Jones, and C. Sutcliffe. Determination of the effect of scan strategy on residual stress in laser powder bed fusion additive manufacturing. *Additive Manufacturing*, 23:13–24, 2018.
- [70] Haider Ali, Hassan Ghadbeigi, and Kamran Mumtaz. Effect of scanning strategies on residual stress and mechanical properties of selective laser melted ti6al4v. *Materials Science and Engineering: A*, 712:175–187, 2018.
- [71] Bey Vrancken. *Study of residual stresses in selective laser melting*. PhD thesis, KU Leuven, Leuven, 2016.